Unclassified **EP 2003-5092**

Amplification of waves by a Concrete Gravity Substructure

by
E. J. van Iperen
(Delft University of Technology)

Sponsor:	SIEP Rijswijk (EP Projects)
Reviewed by:	G.Z. Forristall
Approved by:	G.Z. Forristall
Date of issue:	March 2003
Revision:	1.0
Period of work:	September 2002 - March 2003
Account code:	A33003
ECCN number:	Not subject to EAR-No disclosure of technology

This report documents student work

SHELL INTERNATIONAL EXPLORATION AND PRODUCTION B.V., RIJSWIJK

Further copies can be obtained from the Global EP Library, Rijswijk

Delft University of Technology
Faculty of Civil Engineering and Geosciences
Environmental Fluid Mechanics Section

"Amplification of Waves by a Concrete Gravity Sub-structure"

M.Sc. Thesis

Erik J. van Iperen

March 2003

Thesis committee:

Prof. Dr. ir. J.A. Battjes (Delft University of Technology)
Dr. G.Z.F. Forristall (Shell EP Projects)
ir. J.M.J. Journee (Delft University of Technology)
W.W. Massie M.Sc. P.E. (Delft University of Technology)
Prof. Dr. ir. J.A. Pinkster (Delft University of Technology)

PREFACE

This thesis is submitted in conformity with the requirements for the degree of Master of Science (ir.) in Civil Engineering at the Delft University of Technology. The work was carried out in cooperation with, and facilitated by Shell EP Projects Rijswijk.

This research was carried out under the supervision of Prof. Dr. ir. J.A. Battjes. I want to thank him for his guidance and advice throughout the entire process of this research. I also want to thank ir. J.M.J. Journee and W.W. Massie M.Sc. P.E. for their much appreciated contribution to this work during meetings, telephone conversations, and review work. I thank Prof. Dr. ir. J.A. Pinkster for the time and effort he invested in explaining me how to prepare the input for his diffraction code DELFRAC, for making numerous runs and for being available to discuss the interesting results.

Daily guidance was provided by Dr. G.Z.F. Forristall of Shell EP Projects Rijswijk, with whom I enjoyed working thoroughly. I want to thank him for being available for often interesting discussions and always valuable advice.

During the entire period of this research I was offered a place to work in the Onshore Structures group of Shell EP Projects in Rijswijk. I want to thank everybody there for their contribution to a great learning experience and a very enjoyable time.

I also thank Dr. Prasad from Sandwell Engineering for arranging the transfer of the CD-ROMS with the data from the model tests, Dr. Tromans for the interesting discussions at an early stage of the project and for making reports and videos of similar studies available, and Dr. Ewans for providing me with very useful Matlab scripts.

Finally I thank my family and all my friends for the their support and the fun times we had during my years in Delft. I especially want to thank Esther for being there when times were difficult.

Erik van Iperen

Rijswijk, March 2003

SUMMARY

Diffraction of both regular and irregular waves by a Concrete Gravity Sub-structure (CGS) was investigated using both experimental surface elevation measurements and computational results of the linear diffraction code DELFRAC. The influence of the box-shaped base that supports the four vertical columns was studied independently from the columns, using data from regular wave tests on the Malampaya CGS. DELFRAC was shown to give accurate results for the focusing of waves over the underwater structure. Results from a regular wave data analysis of model tests on the complete Sakhalin II project Lunskoye structure were compared to those predicted by the linear diffraction code. For the wave cases tested, the first-order amplitudes were accurately predicted. Diffraction of irregular waves was studied in a similar way and linear diffraction theory for random seas gave an excellent prediction of incident wave spectral diffraction, including the peaks in the diffracted spectrum near twice the peak in the input spectrum. The results obtained for the Lunksoye structure in the present study are consistent with results found in similar studies on less complex structures. An attempt to predict the extreme crest heights from the diffracted spectrum was made using a Weibull distribution and a second-order expansion of the sea surface that captures the effects of wave steepness, water depth and directional spreading with no other approximation than the truncation of the expansion at second order. Depth induced breaking appeared to be an important phenomenon limiting the crest heights.

KEYWORDS

Linear diffraction, wave amplification, wave structure interaction, Sakhalin, crest heights

TABLE OF CONTENTS

LIST OF FIGURES

LIST OF TABLES

1. INTRODUCTION

1.1. Thesis description

A concrete gravity sub-structure (CGS) is one of many concepts for an offshore production platform. This concept consists of a steel structure mounted on a large underwater concrete structure. The concrete sub-structure is made up out of a box-shaped base supporting multiple vertical columns. As a result of the presence of the structure, the incident waves change as they reach the structure. At present physical model tests are required to investigate wave interaction with the structure. Due to the high costs for such tests, they are performed only for the final design. The objective of these tests is to determine the deck elevation required to avoid green-water impact under extreme storm conditions. The deck elevation is of great importance to the overall design of the platform; it is therefore very valuable to obtain an estimate for the required elevation for various alternatives in an early stage of the design process, prior to the choice for a final design. Making the physical model tests redundant would imply a significant cost reduction. At present physical model tests are however the only tool available to establish the required deck elevation for a CGS structure with sufficient accuracy.

Problem description:

The Canadian Hydraulics Centre (CHC) recently model tested two CGS structures for the Sakhalin II project. The objective of the tests was to determine the required deck elevation and forces from waves on the underside of the deck of the structures. These tests produced a lot of data on surface elevation at the structure under various wave conditions. There is thus the opportunity to use this data to create a prediction method. This method should translate the incident wave height into the surface elevation at the structure for similar structures under similar conditions.

Goal:

The goal of this MSc thesis is to develop a prediction method that translates incident wave heights into green-water surface elevation under the deck of a CGS structure, making extensive use of the test data provided by CHC.

The research can be characterized as data-driven and uses the extensive dataset obtained from the physical model tests for the Sakhalin II project platforms.

1.2. Developing a prediction method

To determine which approach has the biggest chance of developing a successful prediction method, we first gain insight in the available dataset in Section 1.3. A study of literature available on the subject is presented in Section 2. Literature shows that linear diffraction theory gives reasonably accurate results for the two most important wave-structure interactions. Combined with the nature of the dataset, this results in the following approach for the present study:

The linear diffraction code DELFRAC, which is discussed in Section 3, is used to predict the amplification of waves by the structure. We first look at the accuracy of DELFRAC in predicting the interaction with the box-shaped underwater base in Section 4.1, this analysis concerns regular waves only. In Section 4.2.1 the analysis concerns regular waves interacting with the complete structure. We proceed with irregular waves interacting with the complete structure in Section 4.2.2. For a given random sea-state, the diffracted spectra are predicted at various locations around the structure and compared to the measurements.

Various options to derive a maximum crest height from a diffracted spectrum are explored in Section 5. In Section 5.1 we assess the applicability of the Rayleigh distribution, followed by a similar analysis for the Weibull distribution in Section 5.2. The next option compares a second-order expansion of the sea surface to the measurements of the highest crests in Section 5.3.

The phenomenon of depth induced breaking, which significantly influences the energy in the diffracted spectrum and the extreme crest height distribution, is studied in Section 5.4.

Section 6 demonstrates the prediction recipe for two Concrete Gravity Sub-structures and compares the results to laboratory measurements.

1.3. The available dataset from the Sakhalin II project model tests

At the Canadian Hydraulics Centre (CHC), a program of physical model tests was conducted to assist in determining the optimal deck elevations for two offshore structures proposed for different sites in the Sea of Okhotsk near Sakhalin Island, Russia. In their report [6], CHC provided a description of the work that was done and the results that were obtained. The model tests were required to investigate the wave interaction with the two gravity-based structures designed for the Piltun-Astokhskoye and Lunskoye fields, from hereon referred to as PA-B and LUN-A respectively. For each structure, tests were conducted with multiple deck elevations and in extreme wave conditions associated with return periods of 100 and 10,000 years. Most tests were conducted with multidirectional irregular waves alone. However some tests were conducted with a steady state current running perpendicular to the mean wave direction. Regular waves and unidirectional waves were also used for some tests.

1.3.1. Wave basin parameters

- Geometric scale: 1:45
- Dimensions: 30m wide
  20m long
  3m deep
- Structure located centrally
- Progressive Wave Absorbers along three sides not occupied by wave generator
- Absorber opposite wave generator was 6.3m long (stretching over the total width of the basin) and featured reflection coefficients of 2%-6% over a wide range of water depths, wave heights and wave periods
- Guide walls: 11.5m long from wave boards to test site
- Bathymetry: Slope 1:20 rising 0.33m over 6.25m starting 1m from wave boards
- Location test site: Centre on flat bed, 7.75m from top slope, 15m from the wave paddles

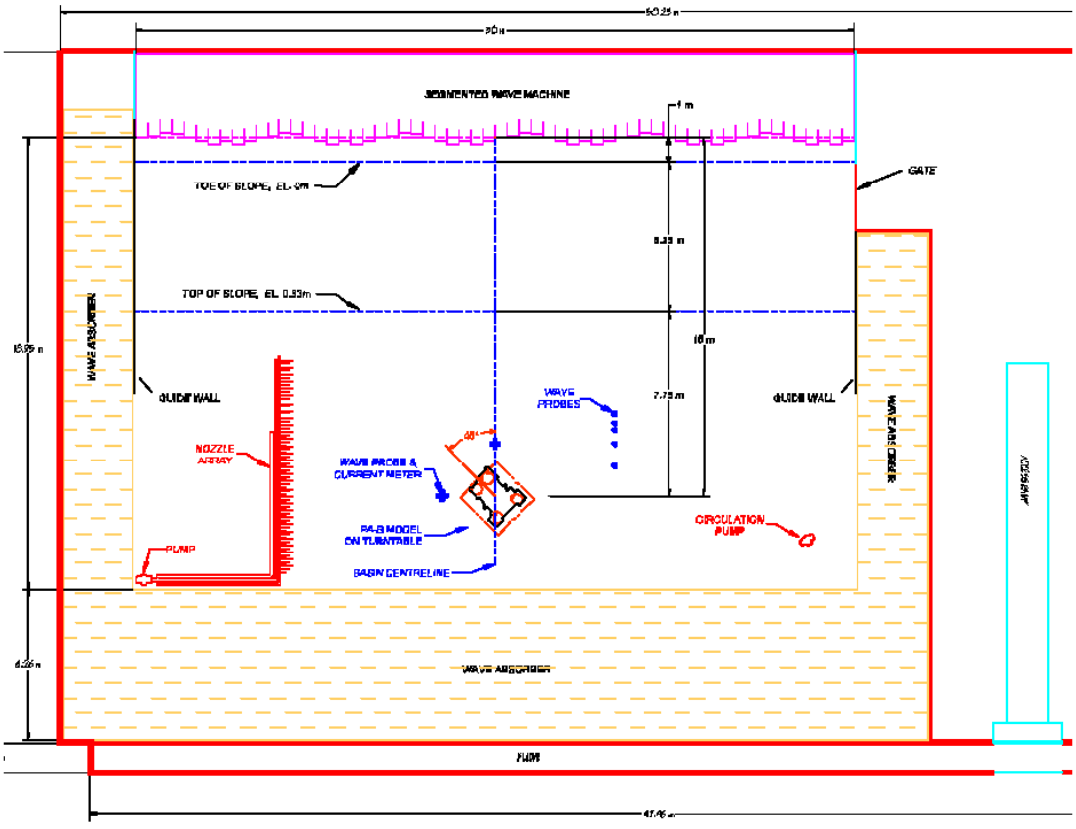

Figure 1: CHC wave basin

1.3.2. Parameters for the PA-B structure

Figure 2 shows the PA-B model at an undistorted scale of 1:45, standing on the floor of the basin. The box-shaped caisson or base (grey), the large concrete columns (black with yellow bands) and the slender steel columns (metal coloured) supporting the deck are clearly visible. The slender black cylinders at the front-left leg are the conductors. They have no structural purpose but transport hydrocarbons up to the deck where they are processed.

Figure 2: PA-B model

All the values are for prototype scale, i.e. not model scale.

- Base: 14m high
  115.25m long (forward to aft)
  109.82m wide (port to starboard)
- Concrete shafts
  All four terminate 27m above the top of the base or 41m above the seabed or 7m above the design still water level
  Approximately 75m forward to aft centre-to-centre spacing
  - Forward: 24m diameter
    33.67m centre-to-centre spacing
  - Rear: 22m diameter
    56.47m centre-to-centre spacing
- Steel columns:
  6m diameter
  74.5m forward to aft spacing
  50m side-to-side spacing
- Design still water level:
  33.94m

1.3.3. Parameters for the LUN-A structure

Figure 3 shows the LUN-A model, here too the base or caisson is grey, the concrete columns are black with yellow bands around the top and the steel columns that support the deck are white with coloured bands.

Figure 3: LUN-A model

All the values are for prototype scale, i.e. not model scale.

- Base: 15m high

  121.03m long (forward to aft)

  108.48m wide (port to starboard)

- Concrete shafts

  All four terminate 45.2m above the top of the base or 60.2m above the seabed or 7m above the design still water level

  26m diameter at the bottom to 23.9m above mid-height

  68.1m forward to aft centre-to-centre spacing

  40.5 side-to-side centre-to-centre spacing

- Steel columns:

  6m diameter

  68.1m forward to aft spacing

  40.5m side-to-side spacing

- Design still water level:

  53.13m

1.3.4. The model tests

For both structures, a large number of target conditions was defined. Tests without the structure in place, which we call undisturbed tests, were performed for two main reasons:

1. To obtain and test the wave machine command signals required to produce the desired wave conditions at the test site.
2. To measure properties of the various wave fields at and around the test site before installing the models.

Table 1: PA-B target conditions

No.	Wave type	Depth (m)	T_R (yr)	H, H_s (m)	T, T_p (sec)	γ	$\mu(\theta)$	$\sigma(\theta)$	Current (m/s)	Other
1	Regular	33.94	-	10	12.7	-	0	-	-	
2	Regular	33.94	-	14	12.7	-	0	-	-	
3	Regular	33.94	-	10	12.7	-	0	-	1.4	
4	Regular	33.94	-	14	12.7	-	0	-	1.4	
5	3D Irregular	33.94	100	9.7	14.2	2	0	15	-	A
6	3D Irregular	33.94	100	9.7	14.2	2	0	15	-	B
7	3D Snapshot	33.94	100	9.7	14.2	2	0	15	-	
8	2D Snapshot	33.94	100	9.7	14.2	2	0	-	-	
9	3D Irregular	30.90	100	9.7	14.2	2	0	15	-	LAT
10	3D Irregular	34.77	100	9.7	14.2	2	0	15	-	HAT
11	3D Snapshot	33.94	100	9.7	14.2	2	0	15	1.4	
12	3D Irregular	33.94	100	9.7	14.2	2	0	15	1.4	
13	3D Irregular	33.94	100	9.7	14.2	2	22.5	15	1.4	
14	3D Irregular	33.94	10,000	13.2	16.6	2	0	15	-	A
15	3D Irregular	33.94	10,000	13.2	16.6	2	0	15	-	B
16	3D Snapshot	33.94	10,000	13.2	16.6	2	0	15	-	

Table 1 shows the target wave conditions for the PA-B tests.

- T_R is the return period of the sea-state in years
- H, H_s is the wave height or significant wave height respectively in meters
- T, T_p is the wave period or peak period respectively in seconds
- γ is the JONSWAP peak enhancement factor
- $\mu(\theta)$ is the mean wave direction measured perpendicular to the wave generator in degrees
- $\sigma(\theta)$ is the standard deviation of the frequency independent wave angle distribution in degrees. For the Multi Directional Spectra (3D), $\sigma(\theta)=15$. For the Unidirectional Spectra (2D) the standard deviation is zero.

- In some tests a current was generated perpendicular to the mean incident wave direction at the location of the structure
- A, B or C indicates a different realization of the same sea-state
- HAT is Highest Astronomical Tide
- LAT is Lowest Astronomical Tide
- A wave snapshot is simply a short interval of irregular wave activity extracted from a longer simulation of a particular sea-state. In the present CHC study, the snapshots chosen contain waves with maximum heights close to the maximum wave height expected in a three hour long simulation.

Table 2: LUN-A target conditions

No.	Wave type	Depth (m)	T_R (yr)	H, H_s (m)	T, T_p (sec)	γ	$\mu(\theta)$	$\sigma(\theta)$	Current (m/s)	Other
1	Regular	53.13	-	10	12.7	-	0	-	-	
2	Regular	53.13	-	14	12.7	-	0	-	-	
3	3D Irregular	53.13	100	9.9	14.3	2	0	15	-	A
4	3D Irregular	53.13	100	9.9	14.3	2	0	15	-	B
5	3D Irregular	53.13	100	9.9	14.3	2	0	15	-	C
6	2D Irregular	53.13	100	9.9	14.3	2	0	-	-	
7	3D Irregular	53.13	100	9.9	14.3	2	0	15	1.4	
8	3D Irregular	53.13	100	9.9	14.3	2	22.5	15	1.4	
9	3D Irregular	53.13	10,000	13.8	17	2	0	15	-	A
10	3D Irregular	53.13	10,000	13.8	17	2	0	15	-	B

The number of actual tests performed with the models in place was 80 for the PA-B model and 47 for LUN-A. Both structures were tested at various deck levels. One of the deck levels was too high for the waves to reach, we will call this the "no-deck" level. In this research project, only the tests with the deck at the "no-deck" level are taken into account due to the fact that wave heights might otherwise be limited by the deck.

1.3.5. Instrumentation systems

The water level measurements were recorded as time series.

- Undisturbed wave tests:

  14 Water level probes were used to measure wave conditions.

- Water level probes during model tests:

  PA-B 30 probes

  LUN-A 26 probes

- Data acquisition:

  A low-speed system was used for sensor outputs during the undisturbed wave tests. The data was sampled at approximately 3 Hz at full scale.

A high-speed system was used for the sensors deployed on the models. The data was sampled at 14.9 Hz at full scale.

All tests were recorded on S-VHS videotape using up to four cameras.

The undisturbed waves were measured at 9 locations over the platform footprint. CHC ran several checks on repeatability of the wave characteristics (period, height, crest elevation etc.) for a given generator signal and obtained very good results. This results in data being available on both the incident wave at the location of the platform during the undisturbed tests, and on the same wave as it interacts with the platform, during the model tests. It is therefore possible to match one incident wave against the same wave as it interacts with the platform. The random waves during the undisturbed test were the same random waves as during the tests with the model in place.

During the tests with the model in place, extensive pressure measurements were made of the wave impacts on various locations on the deck, this in addition to the water level measurements. This information was used by members of the Sakhalin II project design team to select optimal deck elevations for the two structures. In the present study the pressure data will not be used. Figure 4 shows the measurement probe layout for the PA-B model. The outer square is the caisson outline. The blue dots, indicated by R followed by a number, are the water level probes. The green dots, indicated by PP followed by a number, are the pressure probes.

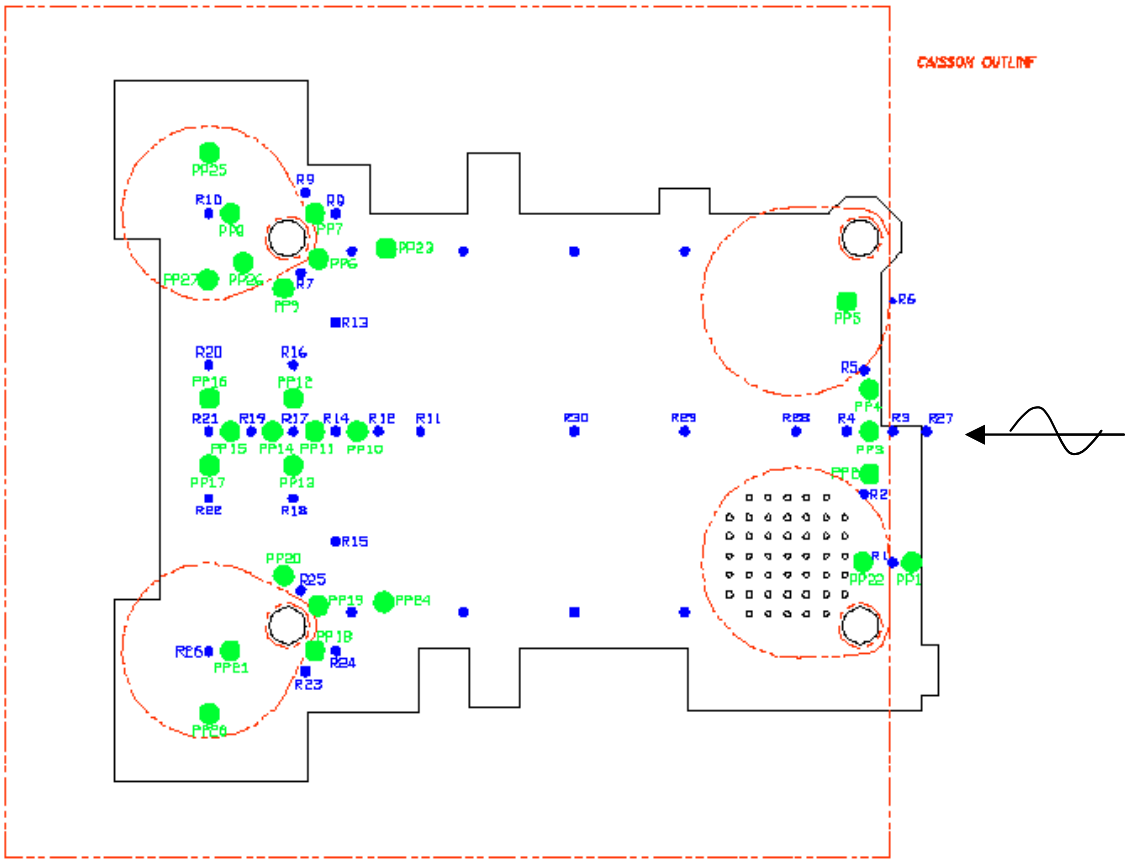

Figure 4: PA-B measurement probes layout

For the LUN-A model the locations of the probes is shown in Figure 5.

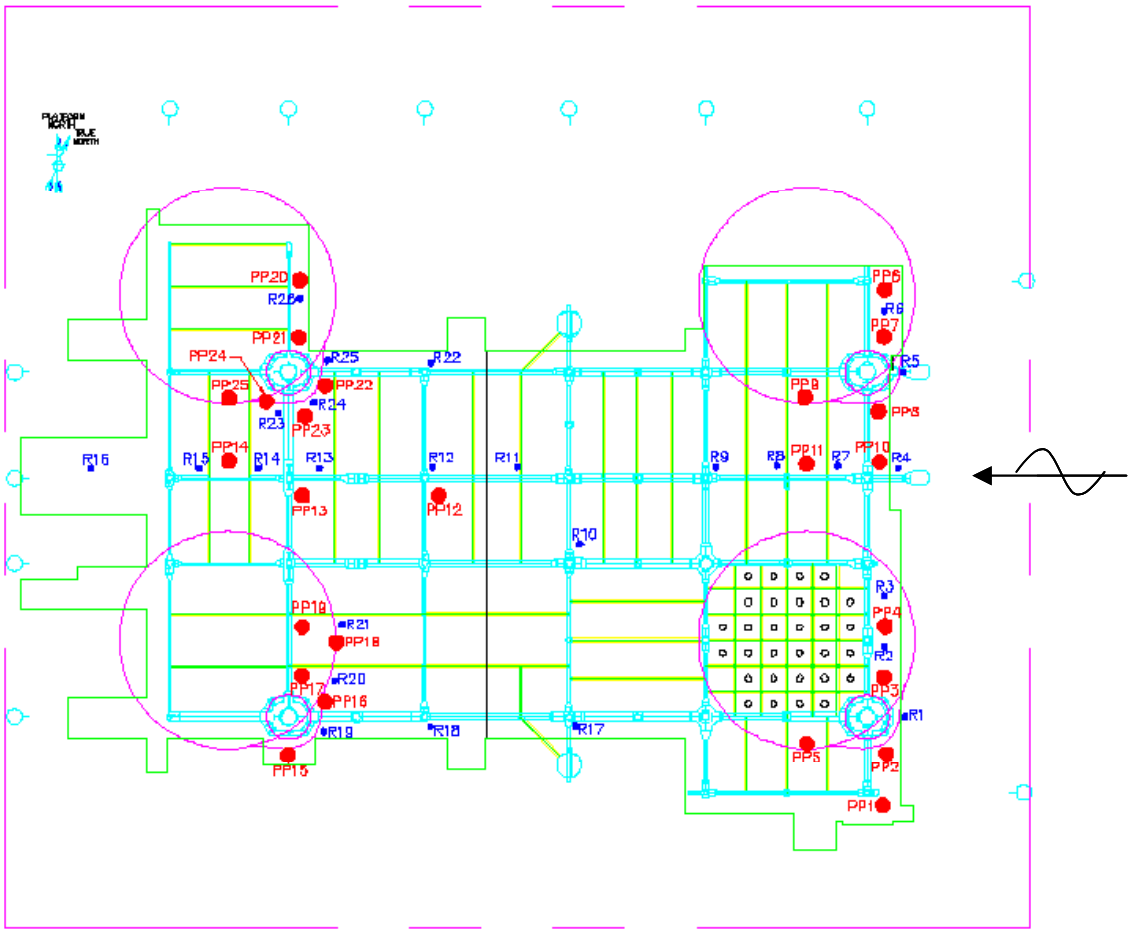

Figure 5: LUN-A measurement probes layout

2. GOVERNING PROCESSES AMPLIFYING WAVES AT A CGS

The interaction of waves with a CGS can be subdivided in three distinctively different processes: Interaction with the base, interaction with multiple columns and interaction with a single cylinder. They will be discussed in that order. Prior that discussion we define the diffraction regime as $k\ell = \mathrm{O}(1)$, where k is the wave number and ℓ is a typical horizontal dimension of the structure concerned.

2.1. Interaction with the base

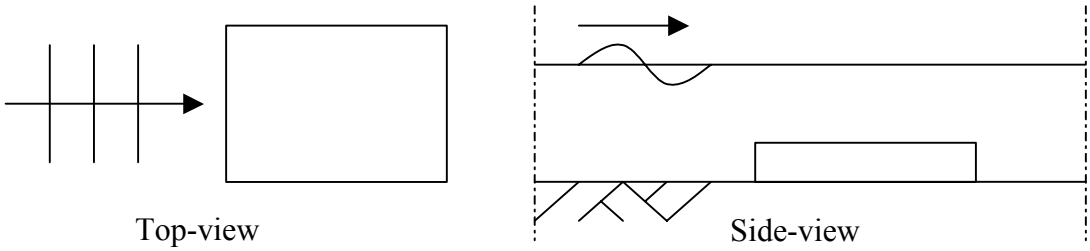

Figure 6: Sketch of wave interaction with the base

In the paper on the Brent Bravo model study, Swan et al. [12] presented the results of a physical model study of waves around the Brent Bravo gravity based structure. The motivation for the study arose as a result of wave damage sustained at the platform during a relatively mild storm. The tests were performed in three stages, where in stage 1 there is no structure present. In stage 2 only the storage caissons on the ocean floor were present and in stage 3 the complete structure was in place. Comparison of the results from stage 1 and 2 yielded information on the interaction of waves with the base only. The water depth at Brent Bravo was 140m and the storage caisson plan dimensions were roughly 100*90 m^2 with a height of 60m. Swan et al. investigated if this roughly 40% reduction in water depth influenced the waves as the propagated over the caisson. One might argue that the reduced water depth slows down the wave, thus decreasing the wavelength and increasing the steepness. If this were the case, there would be a corresponding increase in crest-trough asymmetry and as a result the maximum water surface elevation would be higher above the caisson. However, this approach does not take into account the time required for the changes in the wave profile to evolve. Since the horizontal dimensions of the caisson were in the order of one wavelength, this was particularly important. The experiment showed that the maximum water surface elevations were unaffected by the reduction in water depth for all of the 14 wave cases tested. This was explained in terms of phase velocity of the incident waves and the maximum horizontal dimensions of the base. The longest waves were most susceptible to changes in the water depth since they were effectively propagating in water of intermediate depth. However, the longest waves also had the largest phase velocity and thus the wave was only located over the structure for a small fraction of one wavelength. As a result there was insufficient time for the waves to evolve as they propagated over the caissons. In contrast, the shorter wave periods took much longer to propagate over the base and was located over the caisson for multiple wave periods. But since these waves effectively propagated in deep water and thus were not influenced by the seabed or the caisson, there was no significant change in the maximum crest elevations. The Brent study showed the importance of the ratio of wavelength $L = gT^2/2\pi * \tanh(2\pi h/L)$, which is a function of wave period T and water depth h, to the horizontal dimensions of, and the water depth above the caisson.

In the Malampaya model study, Swan [4] performed tests on a box-shaped submerged caisson in water of 45m depth. Two caissons of different dimensions, 115*100*19 m^3 and 90*75*16 m^3, were tested for different wave-heights and –periods to make a total of 22 regular wave cases. Waves were shown to be affected by the underwater caisson and the interaction mechanism was clearly identified and related to the propagation of the waves over the storage caissons. The local reduction in the water depth, together with the diffraction of the incident waves, resulted in the focussing of wave energy over the downstream half of the structure. This generated increases in wave height over the structure, with an amplification factor of almost 1.4 for the extreme case. This interaction primarily affected the longer wave components considered in this test series and was most pronounced along the centreline of the structure. The difference in the results for the Malampaya study and the Brent study is caused by the difference in water depth between the two.

Much theoretical work on waves interacting with obstacles under water has been carried out:

Mei and Black [9] considered the scattering of infinitesimal surface waves normally incident on a rectangular obstacle in a channel of finite depth. They used a variational formulation as the basis of numerical computations. Scattering properties for both bottom and surface obstacles were presented and compared to experimental results and theoretical results by others. The problem considered by Mei and Black was two dimensional as supposed to the three dimensional problem of waves interacting with the base.

In chapter 3 of his book on ocean surface waves, Mei [10] considered refraction by slowly varying depth or current. The box-shaped caisson in the present study cannot be assumed to have slowly varying depth contours. In chapter 4 Mei addressed waves over a bottom with appreciable variations but for the case of long waves of infinitesimal amplitude. This is not the wave environment of the model in the present study.

Linear wave reflection due to a rectangular bar was considered by Dingemans [11] in his book on wave propagation over uneven bottoms. This two dimensional case is again not a good representation of the presently studied problem.

In their paper on Stokes waves on variable bathymetry, Belibassakis and Athanassoulis [8] presented the extension of second-order Stokes theory to the case of a generally shaped bottom profile connecting to half-strips of constant (but possibly different) depths. Their theory can be used for the study of various wave phenomena (propagation, reflection, diffraction) arising from the interaction of weakly non-linear waves with a general bottom topography, in intermediate water depth. The application of their work to waves interacting with the base is not within the range of this study.

The studied literature does not present a straightforward method that allows for a quantitative description of the interaction of waves with the base. The theoretical work has shown not to be very applicable to our study of the Sakhalin II project structures. Instead we will use the linear wave diffraction program DELFRAC. This program is described in Section 3. The approach on studying the interaction of waves with the base is explained in Section 2.1.1.

2.1.1. Wave focussing

Wave focussing is considered here as the bending towards the structure of incoming waves caused by the presence of the shallow underwater caisson. This process is most severe near the end of the structure, where the waves have had the longest time to be influenced by the

caisson and bend towards the shallower area. A first order approximation is thought to give sufficient accurate results for this process. This assumption will be verified in Section 4.1:

- The model tests performed for the Malampaya structure incorporated testing of the box-shaped caisson only, without the legs in place. The depth and wave regimes were similar to the Sakhalin II project models. Analysis of the experiments showed there is limited wave focussing near the end of the caisson for long waves only. The shorter waves were not feeling the base at all.
- We have used DELFRAC to assess the influence of the base, and output has been generated for the two geometries tested in the Malampaya study. The output of DELFRAC has been compared to the physical tests to give a good insight in the applicability and accuracy of DELFRAC for the case with only the caisson in place.

2.2. Interaction with multiple columns

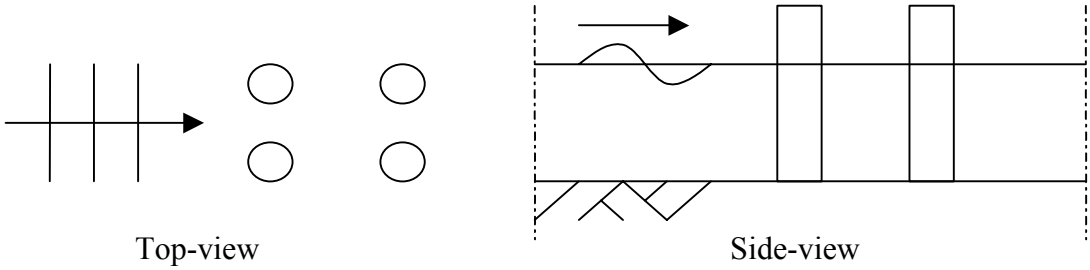

Figure 7: Sketch of wave interaction with multiple columns

After assessing the influence of the base in their paper on Brent Bravo, Swan et al. [12] continued to establish the extent of wave-structure interaction caused by the three large, closely spaced, surface piercing columns in stage 3. The test comprised 11 regular wave cases and 3 so-called New-Wave cases. Together with visual observations, the measurements suggested that the amplification of the maximum water surface elevation was clearly related to the scattering of incident waves by the structure. The Brent Bravo structure was within the diffraction regime and therefore produced considerable disturbance of the incident wave field. In the case of linear diffraction, the frequency of the outgoing or scattered waves would be identical to the incident waves. In one of the regular wave cases however, there was a significant increase in the wave energy located at higher frequencies, corresponding to the third harmonic of the fundamental, which did not appear in other wave cases. Further visual observations confirmed that the generation of high-frequency radiated waves was clearly dependent upon both steepness and period of the incident waves. The mechanisms identified in the paper explain why the extreme New-Wave simulations did not produce significant wave-structure interaction. This was due to the insufficient number of steep waves. To produce amplification of the maximum water surface elevation, steep incident waves first had to induce the forcing necessary to generate high-frequency waves. As these waves radiated outwards from the structure they had to interact non-linearly with the further steep incident waves. A single extreme wave form as predicted by New-Wave was shown to not undergo this type of interaction.

A wave-structure interaction phenomenon of vital concern is the subject of a paper by Niedzwecki and Huston [13] on wave interaction with Tension Leg Platforms (TLP). They referred to it as wave upwelling, the amplification of the incident waves beneath the deck of the platform. For a limited number of cases comparisons were made between

experimental data and numerical predictions. In general the experimental measurements exceeded the linear diffraction numerical model results by an average value of about 10%.

System identification was used by Sweetman and Winterstein [14] in a detailed comparison of model test data and numerical diffraction results in their paper on air gap analysis of the Veslefrikk semi-submersible. 'Optimal' quadratic transfer functions based on system identification of measured data were compared with those resulting from WAMIT [21], hydrodynamic analysis and those from Stokes theory. WAMIT is a set of tools for analysing wave interactions with offshore platforms and other structures or vessel. It has the capability of complete second-order non-linear analysis in bi-chromatic and bi-directional waves. The results of the system identification suggested that the Stokes substitution was reasonable and the quadratic transfer functions at high frequencies from WAMIT analysis were not reasonable.

Diffraction of regular waves by arrays of vertical bottom-mounted circular cylinders was investigated by Ohl et al. [3] using theoretical, computational and experimental methods. Results from regular wave data analysis for the first-order amplitudes were compared with those from linear diffraction theory, which was shown to be accurate in predicting incident waves of low steepness. Linear diffraction theory was shown to be very accurate at predicting the global surface elevation features, even for waves of high steepness. Use was made of the exact solution, under the assumption of linear water wave theory, for scattering of water waves by an array of N bottom-mounted vertical circular cylinders as derived by Linton and Evans [15].

Diffraction of irregular waves by the same array of cylinders was also investigated by Ohl et al. [5]. Linear diffraction theory for random seas was shown to give excellent prediction of incident wave spectral diffraction.

The literature shows numerical modelling of the interaction with the columns can provide accurate estimates for the free surface elevation at the structure. The approach followed is explained in Section 2.2.1.

2.2.1. Scattering

Scattering is considered here as the diffraction of the incident waves by the columns and the interaction of these waves with the incident waves. Previous work has shown it to be dependent on many parameters and that in some cases linear diffraction theory gives accurate results for both regular and irregular waves. Our approach to investigating scattering by the Sakhalin II project models also uses linear diffraction theory:

- The Sakhalin II project model tests have been thoroughly analysed. Water level time series are available throughout many locations around the structure for different wave cases, both regular and irregular.
- The scattering has been predicted by DELFRAC through linear diffraction theory. Results have been compared to the measurements to provide insight in the applicability and accuracy of the numerical model.

2.3. Interaction with a single cylinder

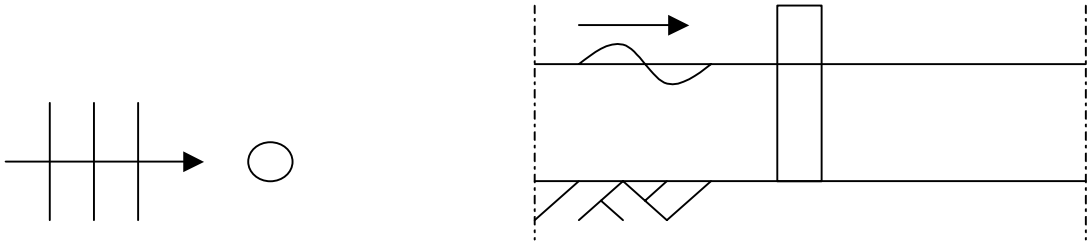

Figure 8: Sketch of wave interaction with a single cylinder

In his paper on wave run-up and forces on cylinders, Niedzwecki [16] compared experimental run-up measurements on a single, circular cylinder during both regular and irregular wave tests with predictions obtained using linear diffraction theory. From this comparison it was apparent that the use of linear diffraction theory for both regular and random waves adequately predicted the forces and that it underestimated the wave run-up for all but very low wave steepness.

Kriebel [19] compared theoretical results for second-order wave run-up around a large diameter vertical circular cylinder to results of regular, non-linear laboratory wave experiments. The second-order theory explained a significant portion of the non-linear wave run-up around the cylinder. The non-linear diffraction theory was found to be valid for the same relative depth and wave steepness conditions applicable to Stokes second-order wave theory. In the last section of the paper, Kriebel presented design curves for estimating maximum second-order wave run-up for a wide range of conditions.

Kriebel [18] also presented various design methods for computing non-linear wave run-up on a large-diameter circular cylinder. First, empirical correlations were developed between the observed maximum run-up and the incident wave and cylinder properties. Then a simple theoretical method was developed to obtain design estimates of the maximum run-up. This method was based on the well-known linear diffraction theory and on the assumption that the higher-order harmonic components of a non-linear wave can be treated as if they were linear waves in order to estimate their individual run-up contribution. Comparison to measurements showed that this simplified method predicted the measured run-up with better accuracy than more complicated but rigorous second-order diffraction theories.

A simplified method for estimating the run-up of non-linear incident waves on large-diameter circular cylinders is presented by Kriebel [17] and compared to experimental data. Results showed that, because of non-linearity, the maximum run-up of random waves on a large vertical cylinder reached an elevation above the still water level of about twice the incident significant wave height for the largest waves in the sea-state. Kriebel [17] stated that critical future work should involve verification of the method using laboratory and field data on wave run-up for a variety of realistic conditions, such as in directional seas or in seas with breaking waves.

An experimental study of run-up on slender columns in steep, deep water waves was described by Martin et al. [20]. Run-up predictions from several theories were compared to the data; the theories were linear diffraction, a superposition method, velocity stagnation head and a related semi-empirical method as derived by Kriebel [18]. It was found that all underestimated the run-up by significant margins, up to a factor of two, with the exception

of the semi-empirical method, which provided a conservative design curve for the shorter wave periods.

The literature shows a lot of effort has been made to develop a method to predict the run-up on cylinders. Our approach on describing the run-up on the CGS columns is set out in Section 2.3.1.

2.3.1. Run-up

Run-up is considered here as the very high jetting water near vertical cylinders. To be able to reach its maximum value, the water needs the support of the cylinder. Since the large concrete columns of the CGS are truncated 7m above still water level, the high waves overtop the columns instead of building up to large elevations on its surface. The dimensions of the steel columns are such that they will not cause run-up that is significant for structural design. Run-up on these columns could cause local damage however. The present research studies the green-water surface elevation and therefore the run-up on the columns will not be studied in great detail. Our approach on studying run-up on the columns is as follows:

- The Sakhalin II project model tests have provided surface elevations near the truncated legs. This experimental data has been analysed.
- Previous work showed that linear diffraction theory underestimated the run-up on circular columns that are not truncated above a certain level above mean sea level. We have compared DELFRAC results to the measurements to determine the applicability of linear diffraction theory for this particular geometry.

3. LINEAR DIFFRACTION MODEL DELFRAC

The linear diffraction code DELFRAC was developed by Prof. Dr. ir. J.A. Pinkster from the Ship Hydromechanics section of the Design, Engineering and Production Faculty of the Delft University of Technology. In 1994 Dmitrieva [7] prepared a report that contained a program description and comparisons between calculations and experimental data. Some work is reproduced in this section, for more detailed information on the theory behind DELFRAC, we refer the reader to the report by Dmitrieva.

3.1. The theory behind the model

The program DELFRAC is a radiation/diffraction program, which is developed for the analysis of the interaction of surface waves with ships and offshore structures. It solves the linear velocity potential problem using a three-dimensional source distribution technique. The program calculates the wave loads and motion responses of a free-floating or fixed structure in regular waves and is applicable to shallow as well as to deep water. It uses a rectangular Cartesian coordinate system with the origin located on the free surface of the fluid and the vertical z-axis positive upward.

The fluid is assumed to be non-viscid, homogeneous, rotation free and incompressible. Due to these assumptions, the fluid velocity may be represented as the gradient of a scalar potential Φ, which satisfies the Laplace equation {1}.

$$\nabla^2 \Phi = 0 \qquad \{1\}$$

The velocity potential φ, is a scalar function of the coordinates and of time. The harmonic time dependence allows the definition of a complex velocity potential, which can be related to Φ by equation {2}.

$$\Phi = \mathrm{Re}\left\{\varphi(x,y,z)\cdot e^{-i\omega t}\right\} \qquad \{2\}$$

The complex velocity potential satisfies the free-surface boundary condition, which is made linear, on z=0 according to equation {3}.

$$\frac{\partial \varphi}{\partial z} - \frac{\omega^2}{g}\varphi = 0 \qquad \{3\}$$

The velocity potential may be decomposed in the way shown in equation {4}.

$$\varphi = \varphi_R + \varphi_D \qquad \{4\}$$

φ_D is the total diffraction potential;

φ_R is the radiation potential connected with the body's oscillatory motion in its six rigid-body degrees of freedom

The radiation and diffraction velocity potentials on the body's wetted surface are determined from the solution of an integral equation obtained using Green's theorem with free-surface source-potential as the Green function.

For the computations, the mean wetted part of the object is approximated by a number of quadrilateral or triangular plane elements, representing a distribution of source singularities. Each of these contribute to the velocity potential describing the fluid flow. Knowledge of the velocity potential around the structure is sufficient to compute the fluid pressures and wave loads.

3.2. In- and output

As input DELFRAC requires:

The geometry of the structure

The assumptions DELFRAC is based on are only valid for relatively low waves. If elements are surface piercing it calculates the amplification factors of the amplitudes as if the elements are infinitely high; the program does not take waves overtopping the concrete columns into account. Since the slender steel columns originate 7m above mean sea level, there is no reason to incorporate them in the input; DELFRAC will not take them into account. Due to the large dimensions of the concrete columns, approximately 24m diameter at mean water level, compared to the steel columns, 6m diameter, and the fact that the steel columns originate 7m above mean sea level, the physical diffraction process will be dominated by the concrete columns. The absence of the steel columns is assumed to have no significant impact on the accuracy of the outcome.

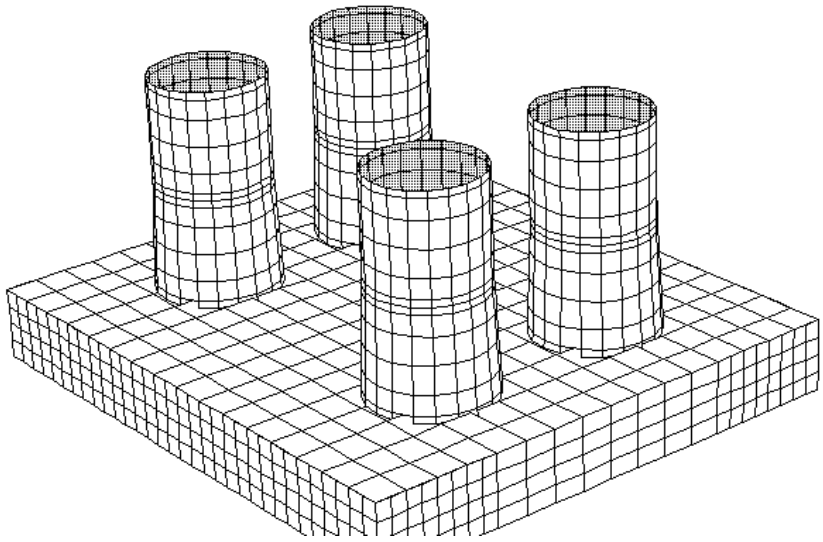

Figure 9: Large mesh-size LUN-A model

The geometry of the structure is entered in mesh coordinates. The mesh or panel size determines the accuracy of the output. As a rule of thumb DELFRAC requires 10 panels per wavelength. This implies that a larger mesh size, like in Figure 9, gives less accurate results for short waves than a smaller mesh size, like in Figure 10.

Location of centre of gravity

DELFRAC requires the location of the centre of gravity with respect to the still water level. Since the CGS is standing on the seabed, this figure is not important and can be set to 0.

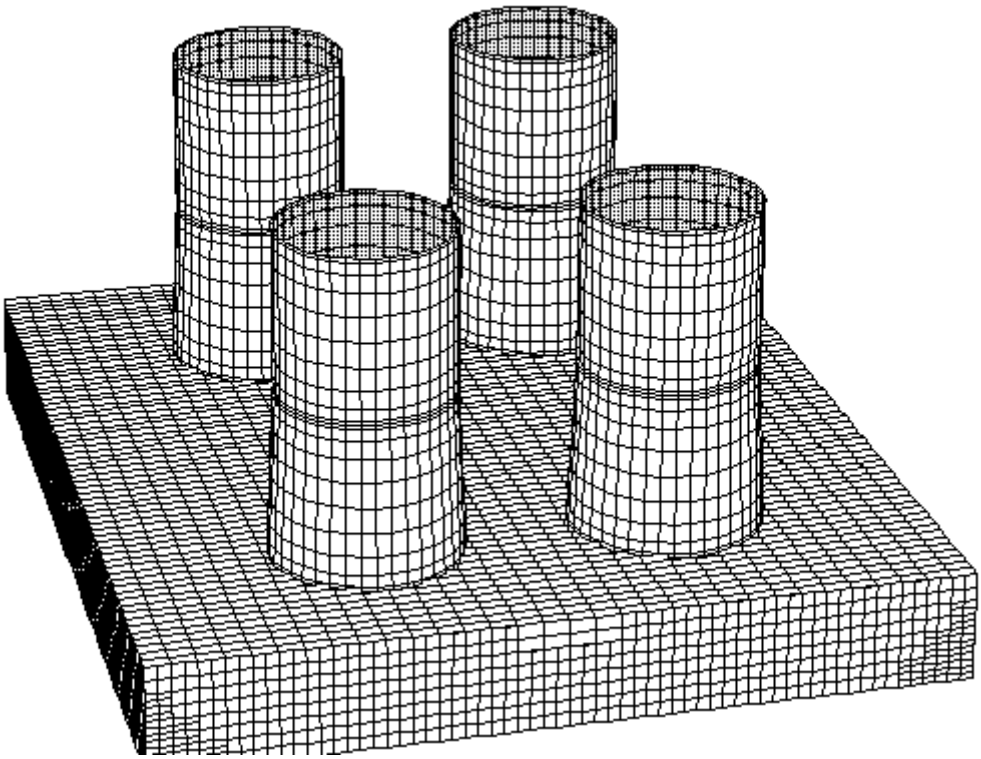

Figure 10: Small mesh size LUN-A model

*6*6 Matrix of mass coefficients and radii of gyration of a body*

DELFRAC requires these figures to calculate the excitation of, and radiation from a floating object. For the bottom founded CGS these values are not important and the matrix can be set to 0 with ones on the diagonal.

Water depth

This parameter is set to 53,13m for the LUN-A model

Wave directions

The user can enter directions of the incident waves with respect to the structure where 180 degrees represents waves approaching the structure head-on from the positive x-axis to the negative. 90 Degrees represents waves approaching from the port side of the ship. In the present study, regular waves approaching the structure head-on are studied in Section 4.1 for the caisson only and in Section 4.2.1 for the complete structure. The analysis in Section 4.2.2 is for multidirectional irregular waves with waves travelling in the mean direction approaching the complete structure head on. This directional spread is not taken into account in the present comparison of DELFRAC to the measurements. The analysis using DELFRAC regards the waves as unidirectional.

Wave frequencies

The user can enter frequencies in radians per second for a specific value or for an array of values, whichever is required.

Coordinates of reference points

These are the coordinates of the origin of the Cartesian coordinate system with respect a reference coordinate system, which is attached to the land.

Waterline points

The locations where the user requires output figures need to be indicated by a number sequence accompanied by (x,y)-coordinates. The waterline elements can either be line elements between two waterline points or just plain waterline points.

DELFRAC needs to solve for all the items listed below, but the user can indicate which data should be send to an output file:

- Six hydrodynamic reaction forces and moments, expressed as added mass and damping coefficients due to the structure-fluid interaction.
- Six first order wave exciting forces and moments including the diffraction effects of the wave on a structure.
- Amplitudes and phases of the six degrees of freedom motions.
- Mean drift forces and moments (near-field method) for six degrees of freedom, which include the fluid velocity components and vessel motion components.
- Mean surge, sway and yaw drift forces and moment based on the Maruo formulation (far-field method).
- Transfer function of the surge, sway and yaw drift forces and moment in regular cross sea of the same frequency based on the far-field formulation and the near-field formulation.
- Amplitudes and phases of reference point motions and accelerations.
- Amplitudes and phases of relative motions.
- Three components of relative fluid velocity at the centre of each panel.
- Hydrodynamic pressure at the centre of each panel.
- Free surface elevation.

In the present research, the absolute wave elevation amplitudes and phase angles are given at all waterline elements, which have been entered in the input as waterline points that include the location of the water level probes in the Sakhalin II project model tests.

4. TRANSFER FUNCTIONS

In this chapter results from the numerical linear diffraction code DELFRAC are compared to physical wave experiments. In addition to the extensive dataset from the recent model tests performed at CHC, use is also made of the report by Swan [4], which contains analysed results from model tests of the Malampaya CGS, a very similar type structure. A Transfer Function (TF) gives an amplification factor, ϕ, that translates the incident wave height, H_i, into a diffracted wave height, H_a.

$$H_a = \phi(x, y, \theta, f) * H_i \quad \{5\}$$

This amplification factor ϕ depends on the structure, the location at the structure, the angle and the frequency of the incident waves.

4.1. Caisson only

The model tests of the Lunskoye and Piltun structures as performed by CHC do not include tests of the caisson only. To make an assessment of the accuracy of the numerical model DELFRAC with respect to the caisson alone, the output is compared to the experimental results from the Malampaya study. The purpose of this study was to investigate the wave conditions on the local reef on which the proposed structure was to be positioned, and to identify the extent of wave-structure interaction. Details of the structural layout had not been finalised at the time of the study. As a result the model tests were of a 'generic' nature in which the extent of wave-structure interaction and the influence of the structural layout was considered. The tests therefore comprised many different wave cases and upper- and lower-bound values of the structural parameters.

Table 3: Geometry of the structure

	Caisson Length	Caisson Width	Caisson Height	Column Diameter	Column Spacing length	Column Spacing width
Upper-bound values	115m	100m	19m	11m	55m	35.4m
Lower-bound values	90m	75m	16m	9m	53.4m	26.7m

Various wave heights at five different wave periods made a total of 22 wave cases, all regular waves. To investigate the relative importance of the wave-structure interaction mechanisms and to assess the significance of the changes in model dimensions given in Table 3, the proposed laboratory study was sub-divided into a number of stages. The intention being that comparison between the data gathered in these stages would highlight the nature and extent of the wave-structure interaction.

- Stage 1: Wave conditions in deep water
- Stage 2: Wave conditions on the model reef
- Stage 3: Wave conditions above the storage caisson
- Stage 4: Wave conditions in the vicinity of a single column on top of the caisson
- Stage 5: Wave conditions around the complete structure

For the present research the wave conditions of stage 2 and 3 are compared; they yield information about the wave amplification by the caisson only.

In his report, Swan [4] presented results comparing the wave conditions from stage 2 with stage 3 only for the highest waves at each of the five frequencies. This resulted in the wave cases shown in Table 4.

Table 4: Regular wave conditions and some additional parameters

Wave case	T (sec)	H_i (m)	L_{deep} (m)	$L_{shallow}$ (m)	Steepness [-]	Ursell # [-]
1e	16.1	16.7	405	349	0.05	22
2e	13.4	17.4	280	264	0.07	13
3e	10.8	16.4	182	179	0.09	5.8
4d	9.0	13.0	126	126	0.10	2.3
5c	7.2	7.2	81	80	0.09	0.5

Where T is the wave period, H_i is the incident wave height, L_{deep} and $L_{shallow}$ are the deep- and shallow-water wavelength respectively, shallow water here being water of 45m depth.

The steepness is defined as $s = \frac{H_i}{L_{shallow}}$ and the Ursell number is defined as

$Ur = \frac{H_i}{d} * \left(\frac{L_{shallow}}{d} \right)^2$, where d is the water depth, which is kept constant at 45m throughout the entire test program.

Swan [4] presented the results of test stages 2 and 3 in the form of time series showing both the undisturbed incident wave on the reef in stage 2, and the disturbed wave above the caisson only (so no columns present) in stage 3. Both time series were plotted in one figure to allow for easy comparison. In stage 2 the wave conditions were measured along the centreline of the entire region where in a later stage the structure would be, using an array of elevation probes. There was a total of 11 probes with a constant spacing of 11.8m. In stage 3 the wave probes were placed in the exact same position with the centre probe at the centre of the storage caisson. The front- and rear probe were placed up- and down-wave of the caisson respectively.

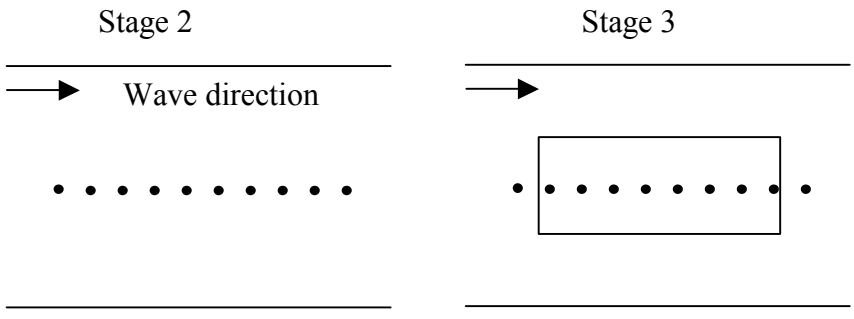

Figure 11: Probe locations for the different test stages

Using the time series an average wave height can be estimated for both the undisturbed case, stage 2, and for stage 3, with the caisson in place. Dividing the average disturbed wave height by the average undisturbed wave height gives the amplification factor. This factor is dependent on the geometry of the structure, the location at the structure and on the

frequency of the incident wave. Each wave case represents a different incident wave period and therefore frequency.

For comparison with the measurements, we loaded the structure geometry into DELFRAC. The results from the DELFRAC runs are amplification factors at each location at various frequencies. The output for the upper-bound values of the geometry is shown for three locations in Figure 12.

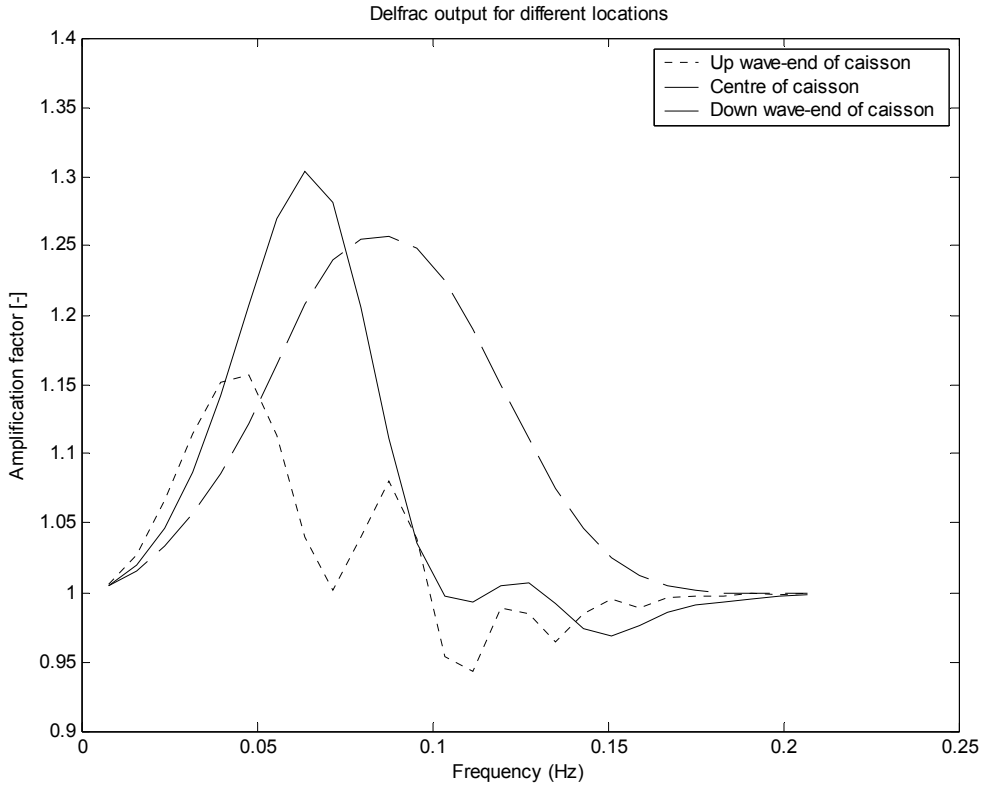

Figure 12: Upper-bound values DELFRAC output at various locations

Figure 13 shows a comparison between DELFRAC and the measurements for the upper-bound values. The same procedure is followed for the lower-bound values of the geometry, and the results are shown in Figure 14. In his Final Report of the Malampaya CGS, Swan [4] included comments about the process of wave amplification due to the caissons, and some of these comments are reproduced here. For wave case 2e at the upstream end of the structure the increase in crest elevation is immediately apparent. It is not reproduced by DELFRAC but it is relatively small compared to the values recorded elsewhere. However as the wave profile both adjusts to the local change in water depth and undergoes the effects of wave diffraction, the increase in the maximum crest elevation is considerably enhanced. The nature of this amplification process is such that as the waves propagate over the storage caisson, their phase velocity reduces. This leads to a curved wave front, which in turn encourages the focussing of wave energy towards the rear of the structure. In this case the largest effect will clearly be generated along the centreline of the structure.

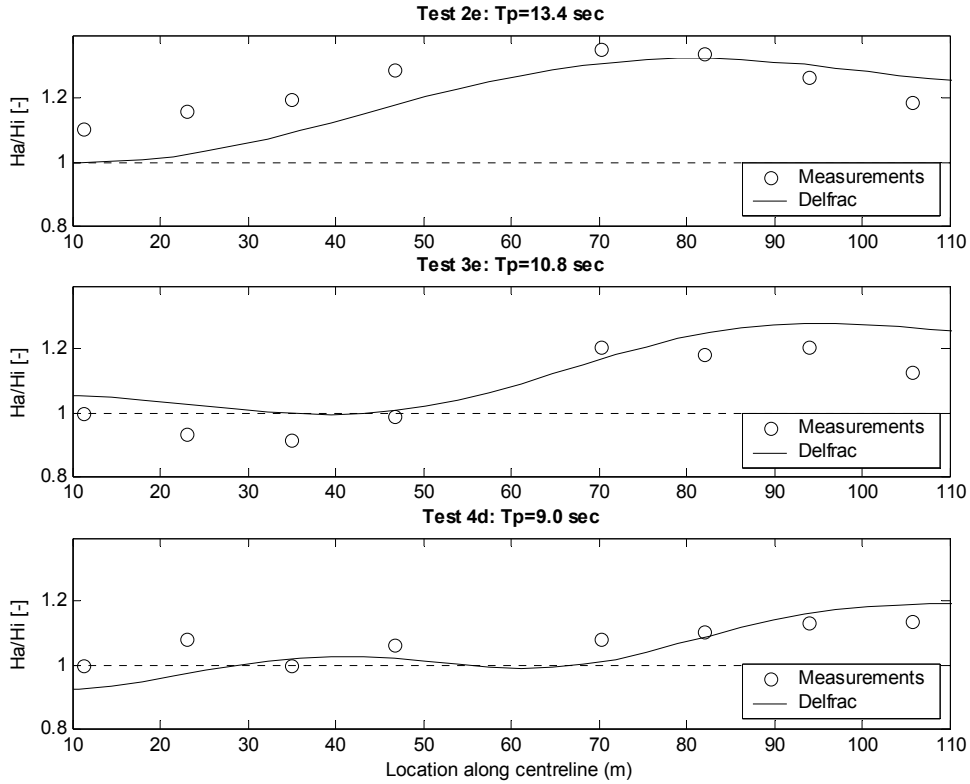

Figure 13: Comparing DELFRAC output to upper-bound measurements

The results from wave case 4d suggest that the interaction with the storage caissons is strongly dependent upon the wavelength of the incident waves. It can be argued that as the incident wavelength reduces, the effective reduction in water depth becomes smaller. As a result of this, the amplification factor might be expected to be smaller. However, wave focussing, the process described above, acts to counter this effect since its magnitude depends on the size of the caisson relative to the incident wave length. As a result, significant increases are again observed on the downstream side of the structure. With a simple hand calculation the influence of shoaling in the amplification process can be assessed qualitatively. The theory assumes a gradual slope with parallel contours, which is obviously not the case. But for a gradual slope from 45m to 26m water depth (which is the water depth above the upper-bound caisson), the shoaling factor can be calculated to be $K_s = \frac{K_s(45m - 26m)}{K_s(deep - 45m)} = \frac{0.939}{0.913} = 1.03$. If anything, this figure shows that shoaling is not the governing process.

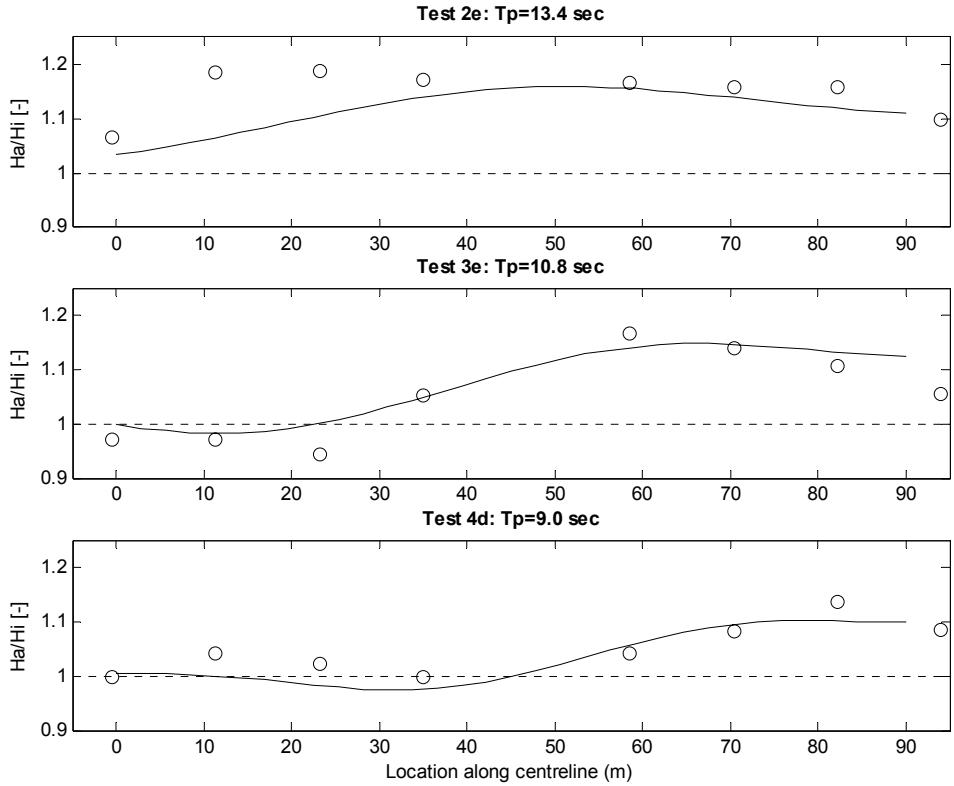

Figure 14: Comparing DELFRAC output to lower-bound measurements

In the Malampaya report, Swan [4] referred to diffraction calculations made earlier and noted that the measurements appeared to be in good agreement. He further stated that for the complete structure, a storage caisson with four supporting columns mounted on top, two separate wave-structure interaction mechanisms were clearly identified. The first was related to the propagation of the waves over the storage caisson. The second mechanism was a separate interaction between the incident waves and the legs of the structure. Swan showed the two interactions were not linearly additive. Based on the comparison of the measurements with the DELFRAC output, we can conclude that DELFRAC gives good results for this first mechanism, the so-called caisson effect or wave-focussing.

4.2. Complete structure

As shown in Table 2 in Section 1.3.4, the LUN-A model was tested in many different sea-states. In addition to all these different sea-states, the model heading was varied. Only five sea-states are analysed in the present study, all with the model centreline in the mean incident wave direction. The sea-states and their indexing are shown in Table 5.

Table 5: LUN-A target conditions

No.	Type	Depth (m)	T_{return} (years)	H, H_s (m)	T, T_p (sec)	γ	μ(θ) (deg.)	σ(θ) (deg.)
1	Regular	53.13	-	10	12.7	-	0	-
2	Regular	53.13	-	14	12.7	-	0	-
3	3-D Irregular	53.13	100	9.9	14.3	2	0	15
4	2-D Irregular	53.13	100	9.9	14.3	2	0	-
5	3-D Irregular	53.13	10,000	13.8	17	2	0	15

For the irregular sea-states, we define the significant wave steepness and Ursell number as follows:

$$S_{sig} = \frac{H_{m0}}{L_{shallow}} \quad \{6\}$$

$$Ur = \frac{H_{m0} * L_{shallow}^2}{h^3} \quad \{7\}$$

where:

H_{m0} is the significant wave height in meters: $H_{m0} = 4\sqrt{m_0}$

$L_{shallow}$ is the shallow water undisturbed wave length in meters:

$$L_{shallow} = \frac{gT_p^2}{2\pi}\tanh\left(\frac{2\pi h}{L_{shallow}}\right)$$

T_p is the peak period in seconds

h is the water depth in meters.

This results in Table 6.

Table 6: Irregular sea-state non-linearity parameters

	100-year	**10,000-year**
$\mathbf{S_{sig}}$	0.037	0.037
Ur	4.6	13

The undisturbed sea-states were measured by nine probes, referred to as front left to back right, throughout the location where later the structure would be. The results from the spectral analysis of the irregular tests are shown in Figure 15, Figure 16, and Figure 17.

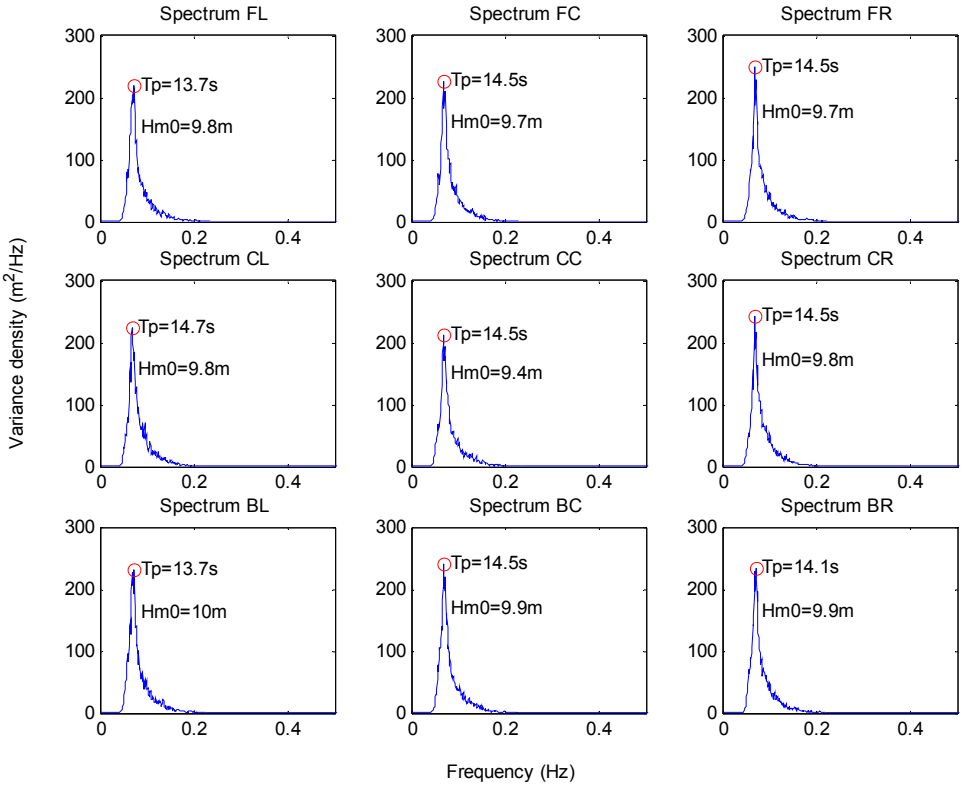

Figure 15: 100-year MDS undisturbed irregular sea-state

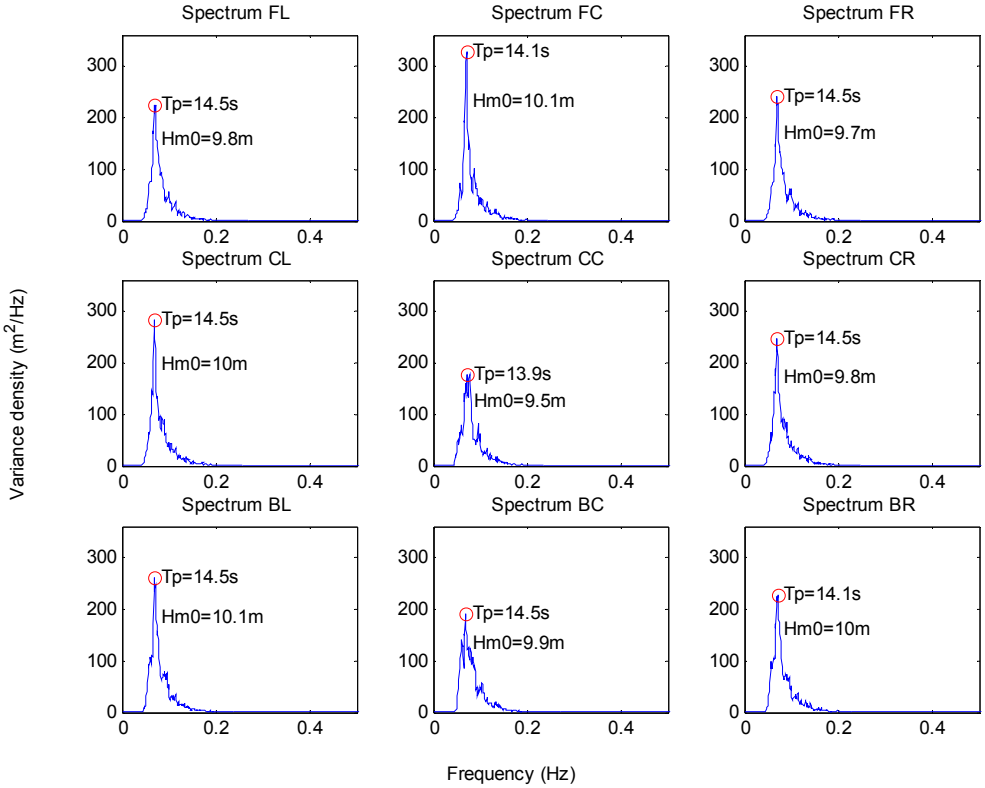

Figure 16: 100-year UDS undisturbed irregular sea-state

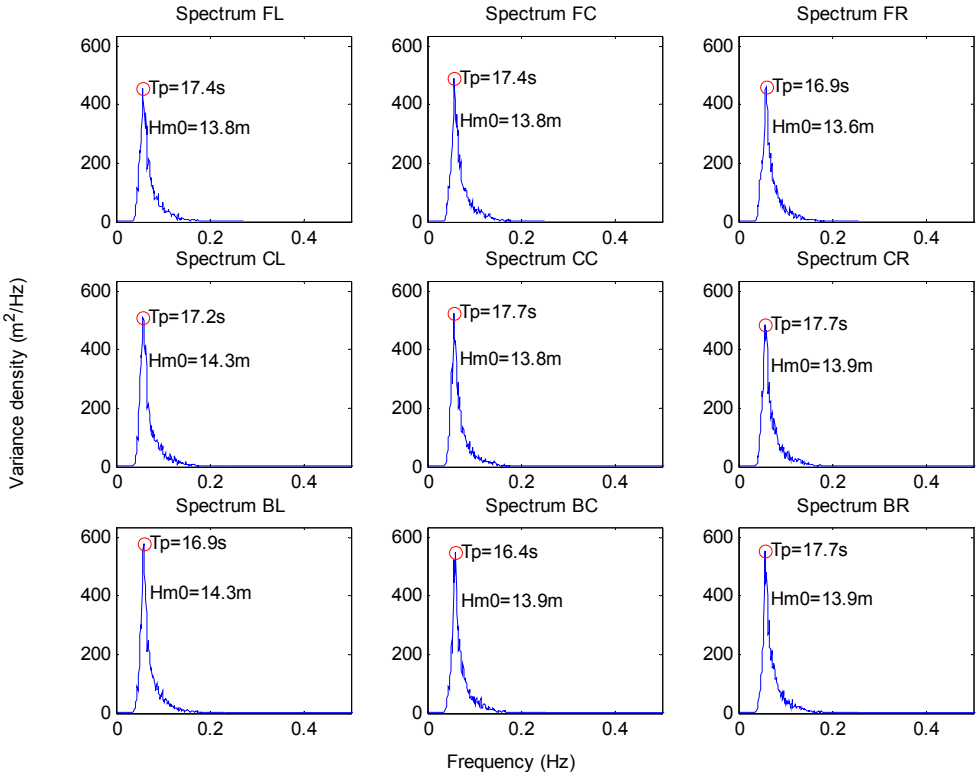

Figure 17: 10,000-year MDS undisturbed irregular sea-state

4.2.1. Regular waves

In their paper on regular wave diffraction, Ohl et al. [3] discussed experiments in an offshore basin at HR Wallingford, for which free surface elevation measurements were made to allow for direct comparison with diffraction theory. They stated that where previous comparisons of theoretical free surface elevation to experimental measurements were conducted, these were for experiments involving single cylinders and small wave heights. Clearly these single cylinder cases yielded no information on the complex scattering problem for the interaction of multiple bodies and were of little interest for the practical design of large offshore structures. In addition the small-amplitude waves that were tested, were nothing alike the highly non-linear, steep ocean waves encountered in typical design conditions. Ohl et al. further stated that while more complex geometries like a Tension Leg Platform (TLP) or GBS with truncated or tapered columns were tested under design conditions, these were of sufficient complexity to make direct comparison with the most basic theories impossible. They therefore simplified the geometry of the experimental model to a square array of bottom mounted cylinders. This simplified geometry and the free surface elevation measurements allowed them to make a relatively straightforward comparisons with alternative theoretical and numerical data. A sketch of the geometry is shown in Figure 18.

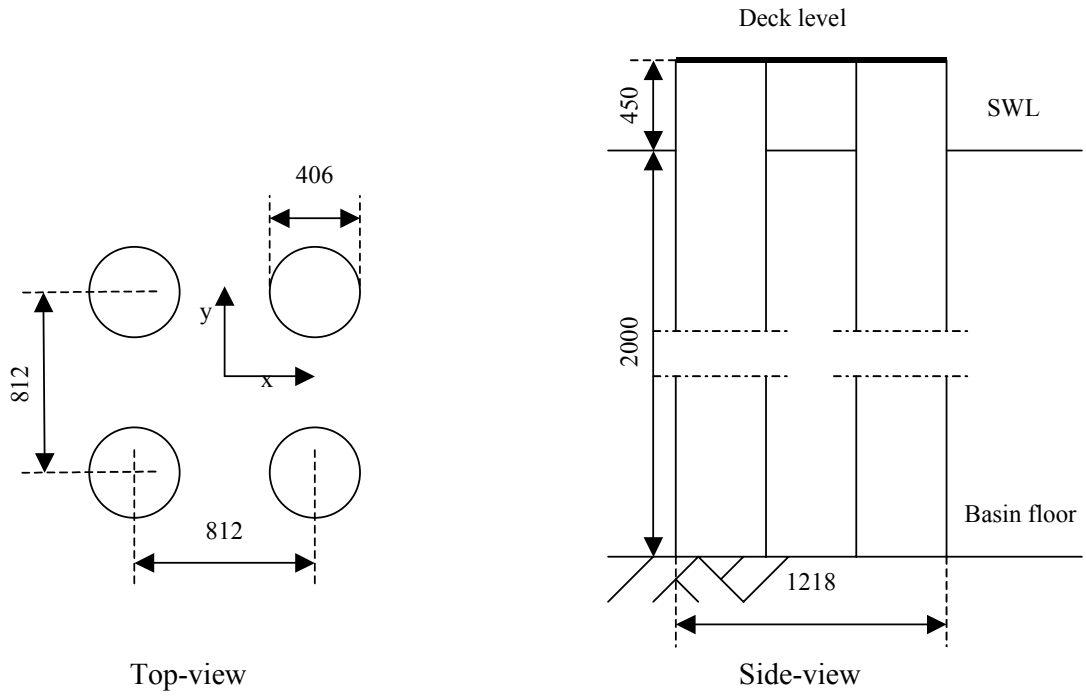

Figure 18: Model structure studied by Ohl et al.; values in mm

The present research gives results for a similar exercise performed on the much more complex LUN-A model tested by CHC: a CGS with rectangular spaced, truncated columns (the large circles in Figure 19), mounted on a rectangular box-shaped, bottom mounted storage caisson (the large rectangle in Figure 19). Ohl et al. studied the amplification for different regular wave cases, one of which allows for straightforward comparison to the present study. The parameters of that wave case are scaled to the LUN-A regular wave case using the ratio of wave frequencies between the two tests. The most important difference is that the tests by Ohl et al. were in much deeper water than the LUN-A tests. The results are shown in Table 7.

Table 7: Test matrix for both Ohl and LUN-A regular waves

	Ohl	**LUN-A**	**Scaled Ohl**
Frequency f (Hz)	0.8	0.08	0.08
Water depth h (m)	2	45	200
Amplitude high (m)	0.09	7	9
Amplitude low (m)	0.05	5	5
Column spacing (m)	0.8	68	81
Column diameter (m)	0.41	26	41
Deep water wavelength (m)	2.44	252	244

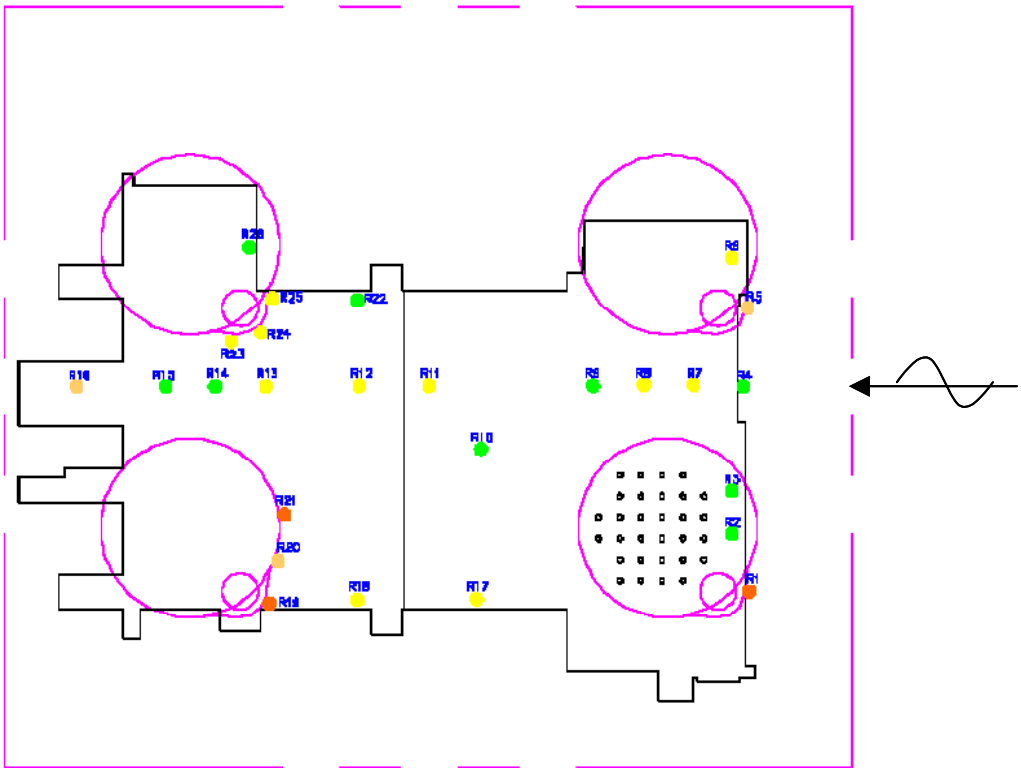

Figure 19: Probe locations along the centreline of the LUN-A model

Probes R4, R7-R9, R11-R16 represent an array of 10 measurement probes along the centreline of the LUN-A model starting at the up-wave end of the model. Fourier analysis of the wave records, as described in A1.2.2, at each location provides an estimate for the amplitudes of the harmonic components at that location. For example take the five regular wave cycles, as identified by CHC, from the undisturbed wave as shown in the top graph in Figure 20. The bottom graph shows the same five cycles at R4. Copying the five cycles, as discussed in A1.2.2.2, provides a sufficiently long time series for high spectral resolution. The variance density plots of these copied time series, and the amplitudes of their harmonic components are shown in Figure 21. The same exercise is performed for all the locations along the centreline. This results in values for the amplitudes of the first three harmonic components at every probe location along the centreline of the model.

To be able to compare the measurements with the results from linear diffraction theory, the complete model is loaded in DELFRAC to give similar output as for the case with the caisson only, which is discussed in Section 4.1. For a discrete number of locations along the centreline the amplification factor is given over a discrete number of frequencies.

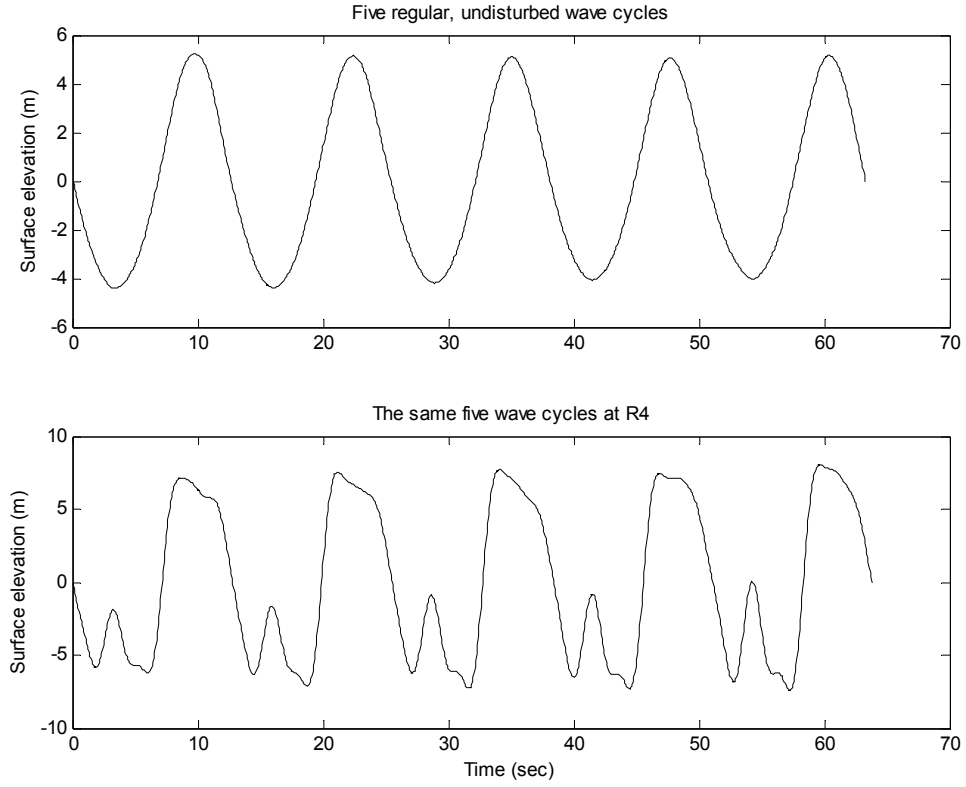

Figure 20: Regular wave test; target parameters H=10 m and T=12.7s

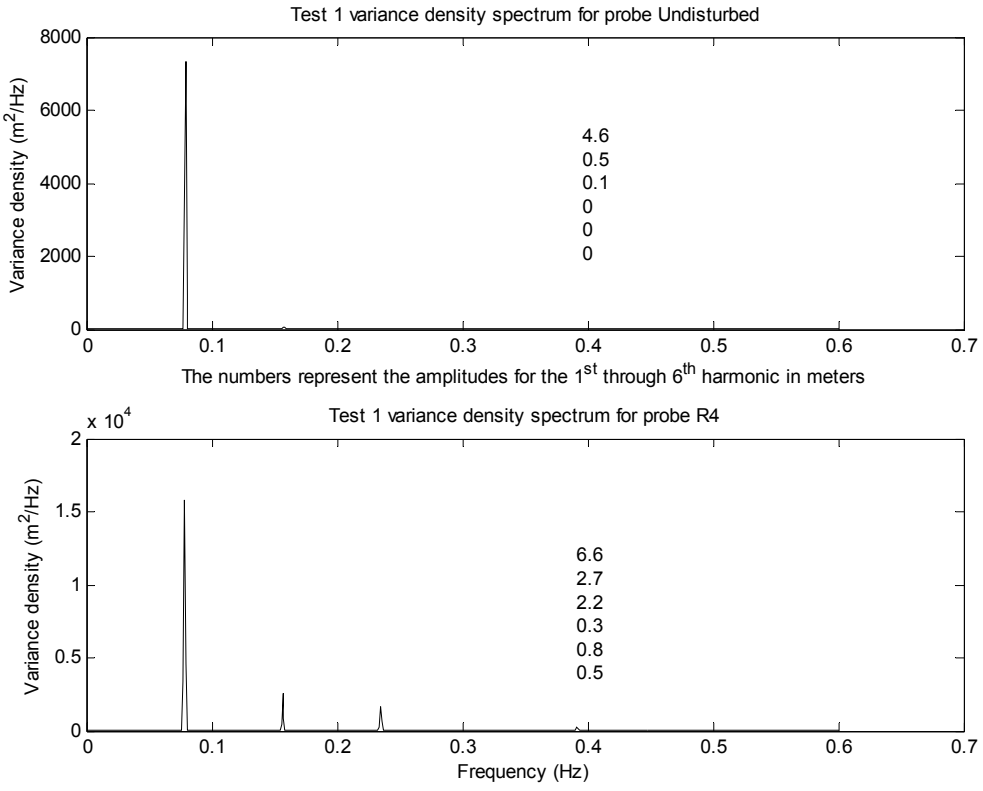

Figure 21: Regular wave test variance density spectra at two locations

Results from two regular wave model tests are available, one that is discussed above with a wave period of 12.7 seconds and a wave height of 10 meters. A second test represents a steeper wave case, with the same wave period of 12.7 seconds but a larger wave height of 14 meters. For each test, the measured amplitude of the first order harmonic, here called $\eta^{(1)}$, at each probe location is normalized by the measured incident wave first order amplitude, here called A, of that specific test case, to give the first order amplification factor at each test. This is compared to the DELFRAC results in Figure 22. In this figure the waves pass the structure from left to right so from x=0m to x=120m.

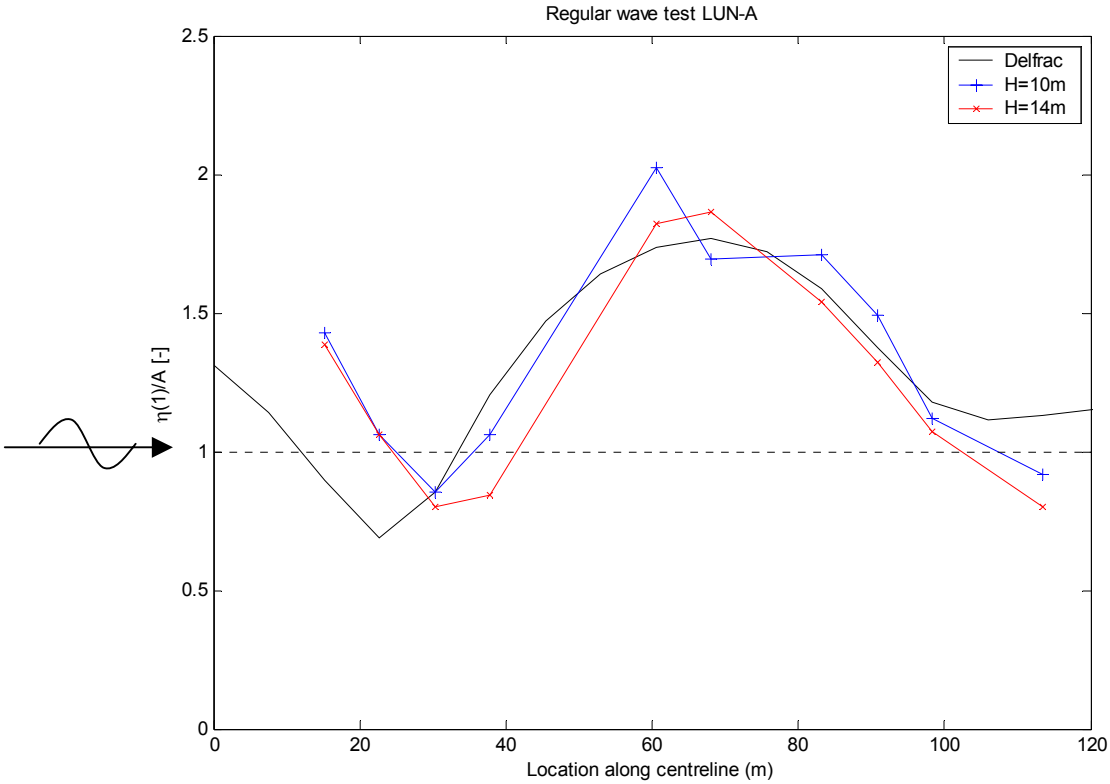

Figure 22: First-order amplitude versus position

With some notable exceptions, the experimental and theoretical results at first order are in close agreement with each other, ànd with the results found by Ohl et al. [3]. There is little difference between the two wave-steepness cases, as expected from linear theory. The centreline plots for both the theory and the experiment indicate a large peak approximately at the model centre, which is at roughly 60m along the centreline in Figure 22. Although the agreement between experimental data and theory is quite close, there are some discernible differences.(Ohl et al. found that the magnitude of the up-wave peak, a peak in front of the structure away from the area of the deck, was significantly underestimated by the theory. There are no measurements in this area for the LUN-A model and therefore nothing can be said about the agreement between theory and the measurements performed by CHC. This phenomenon occurs away from the deck area and as such, it is not of immediate interest for the present research.)

The most important discrepancy is that the measured minimum in between the two front legs, approximately between x=20m and x=40m, seems to be shifted down-wave of the theoretically predicted minimum. This is also found by Ohl et al.. A solid explanation is not available. In addition, the amplification factor for the measurements continue to drop after

x=100m, whereas DELFRAC predicts a slight increase in amplification factor. A possible explanation for this is dissipation of energy due to breaking, which obviously is not taken into account by DELFRAC. The second- and third-order components, $\eta^{(2)}$ and $\eta^{(3)}$, are normalized by kA^2 and k^2A^3 and presented in Figure 23 and Figure 24 respectively. The wave number $k = \frac{2\pi}{L}$ where L is the shallow water wavelength, which is calculated to be 227m for a wave period of 12.7 seconds and a water depth of 53 meters.

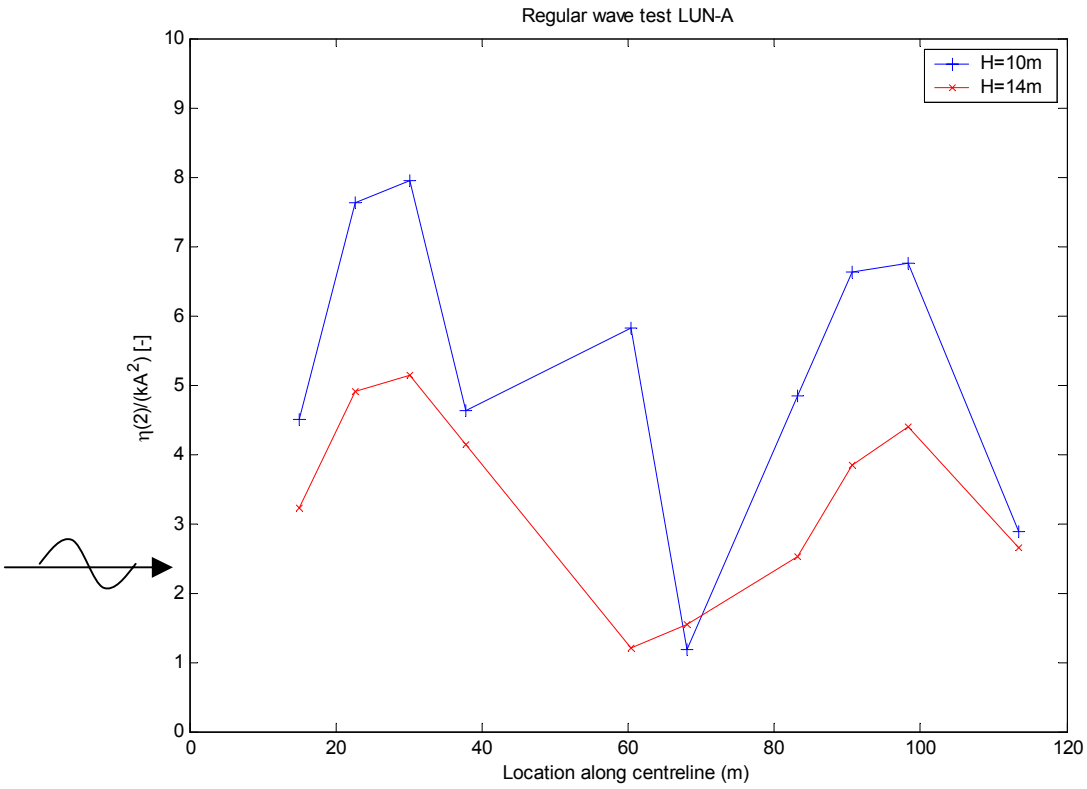

Figure 23: Second-order amplitude versus position

As in the paper by Ohl et al., plots for the lower amplitude waves with H=10m, show significantly higher non-dimensional peaks at both second- and third-order than the higher amplitude wave case, H=14m. They do show similar trends in the location of peaks and troughs however. Many trends are not as pronounced as they are in the more closely spaced array of measurement probes used by Ohl et al.. It is believed there is enough resemblance however to adopt the findings of Ohl et al. with respect to the global trends in second- and third-order profile: In general the second-order peaks correspond with the peaks and troughs of the first-order profile. Second-order troughs appear at the maximum slopes of the first-order profile. Third-order peaks appear at the peaks and maximum slopes of the first-order profile, and third-order troughs appear at the first-order troughs and any gradual slope or crest transition point. However the largest third-order peaks occur at the first-order maximum slopes, with less significant third-order peaks at the first order peaks. This behaviour is clearly observed in the paper by Ohl et al., but due to a limited amount of probes not as clearly in the present research. Figure 24 shows a third-order peak at approximately x=40m flanked by two third-order troughs. These trough locations, at x=30m and x=60m, correspond with a trough and a peak in the first-order profile in Figure 22. A first-order peak should correspond with a third-order peak and this is not the

case. The significantly higher third order peak at the first-order maximum slope from x=30 to x=60 is however clearly present.

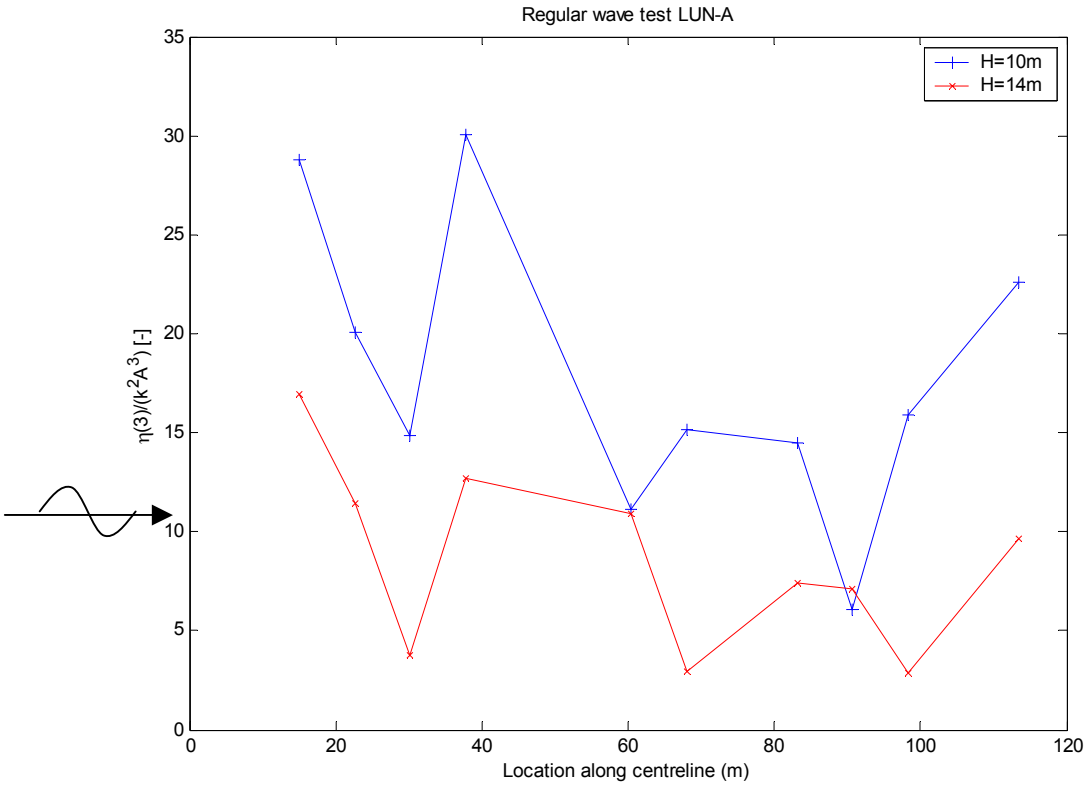

Figure 24: Third-order amplitude versus position

For the LUN-A model, the influence of the caisson on the amplification of regular waves with a period of T=12.7 seconds is very limited. As mentioned in Section 4.1, Swan [4] found that the amplification due to wave-focussing and the amplification due to scattering are not linearly additive. However, to give an indication of the increase in wave height due to the caisson alone, Figure 25 shows the amplification factor along the centreline as calculated by DELFRAC.

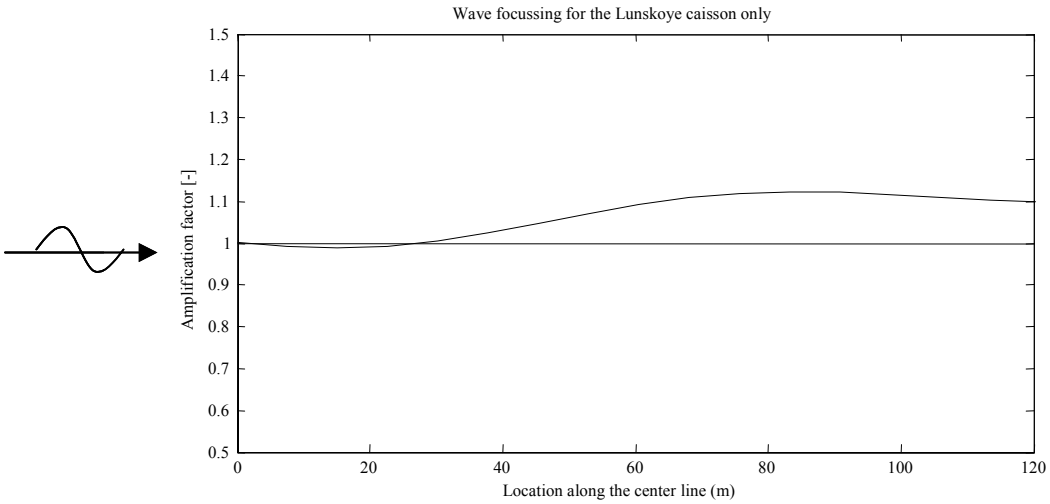

Figure 25: The caisson effect for the LUN-A model

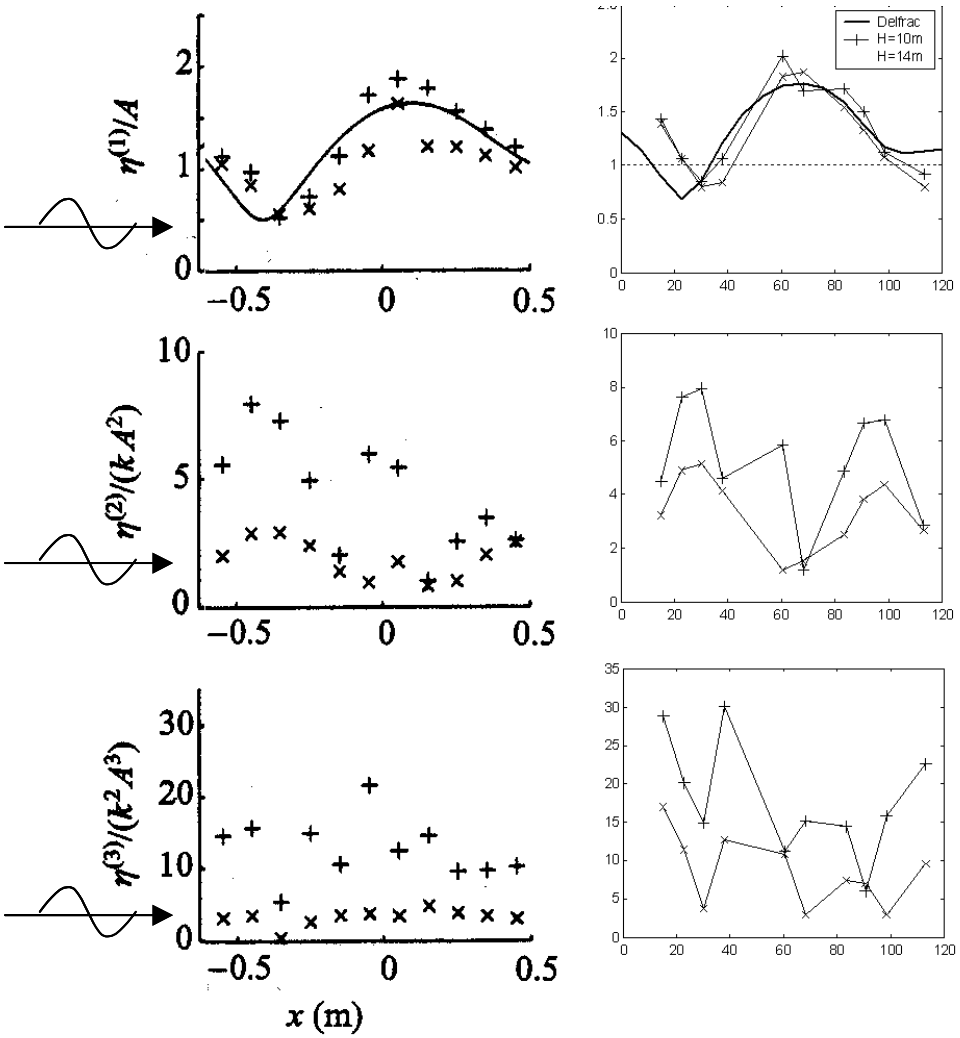

Figure 26: Amplitude versus position Ohl et al. and present study

The figures provided by Ohl et al. [3] in their paper on regular waves, are adjusted slightly to allow for a more straightforward comparison of the results from the two studies. The results from the first- second- and third-order harmonic analysis is shown in each row respectively with the present study in the right-hand and the results found by Ohl et al. in the left-hand column. The non-dimensional y-axis is equally scaled and numbered. For the dimensional x-axis the scale is the same for the two columns, even though the numbers are not. The results from Table 7 are recalled here, which state that the length dimensions from the study by Ohl et al. can be scaled to the present study using a ratio of 1:100. The centre of the structure is at x=0 in the left and x=60 in the right column.

4.2.2. Irregular waves

For irregular waves a similar approach is followed as for regular waves. A number of objectives, as defined by Ohl at el. [5] in their paper on wave diffraction by irregular waves, are reproduced here. Ohl et al. expanded diffraction theory for cylinder arrays to cover random seas at first order. They analysed free surface elevation time histories collected from irregular wave experiments and assessed the diffraction theories for random seas. The present research assesses how well the linear diffraction code DELFRAC describes wave

diffraction for random sea states, by comparing the results to the recent measurements made by CHC. The necessity of introducing higher order effects by empirically adjusting the diffracted spectrum as calculated by DELFRAC will be explored.

The complete model is loaded in DELFRAC and the output is the phase and the amplification factor ϕ, at predetermined locations along the structure for a number of discrete frequencies. Figure 27 shows the amplification factor from DELFRAC at the location of measurement probe R4 over the frequencies. In reality the TF is continuous but in Figure 27 the step size Δf is quite large. Reducing the step size would result in a more continuous TF but also increases computation time significantly. For the wave prediction recipe developed within this research, a more continuous TF would not result in a significant increase in the overall accuracy.

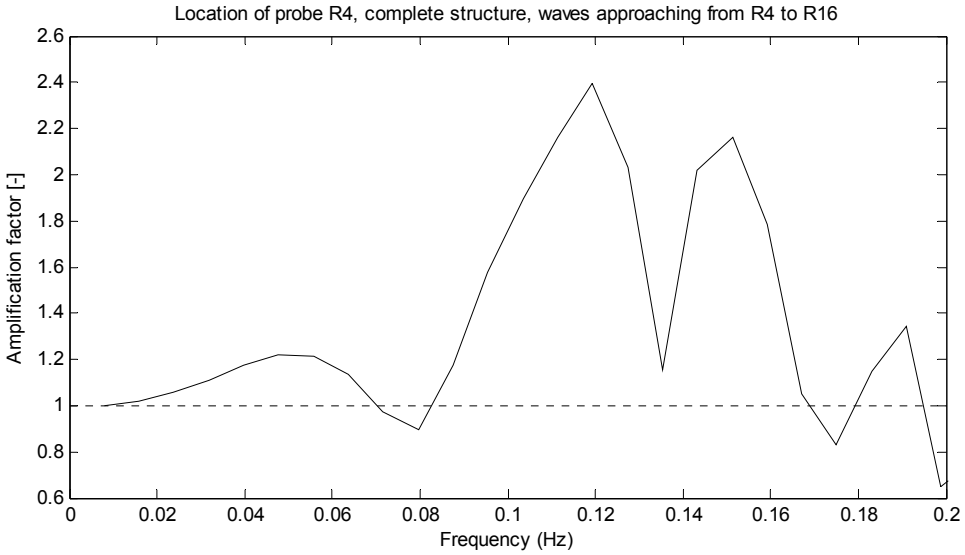

Figure 27: Transfer function for probe R4

Contour plots of the amplification factor and phase throughout the structure are shown in Section 4.2.4 to point out principal features, but first the applicability of DELFRAC and the fit to the measurements is studied in the sections prior to that.

The amplification factors as calculated by DELFRAC can be used to translate the incident wave spectrum into a diffracted spectrum according to equation {8}.

$$S_D(x, y, f_n) = \phi_n^2(x, y) * S_i(f_n) \qquad \{8\}$$

Like the amplification factor ϕ, the incident wave variance density $S_i(f_n)$ is also defined at discrete frequencies however, with a smaller step size Δf since this determines the spectral resolution as discussed in A1.2.2. Therefore the TF as calculated by DELFRAC is linearly interpolated to provide an amplification factor at every discrete frequency with a value for the incident wave variance density. By applying equation {8} the variance density spectrum as predicted by DELFRAC can be calculated and compared to the measured variance density spectrum. This exercise is performed for the 100-year multidirectional sea-state, test3 in Table 5, for all the measurement probe locations along the centreline, the results are shown in Figure 28 trough Figure 37. In these figures, the black line represents the undisturbed spectrum, the blue line is the measured spectrum of which the peak-frequency, the peak-period and the significant wave height H_{m0}, are stated. The red line is the spectrum as predicted by DELFRAC, of which also the significant wave height is stated.

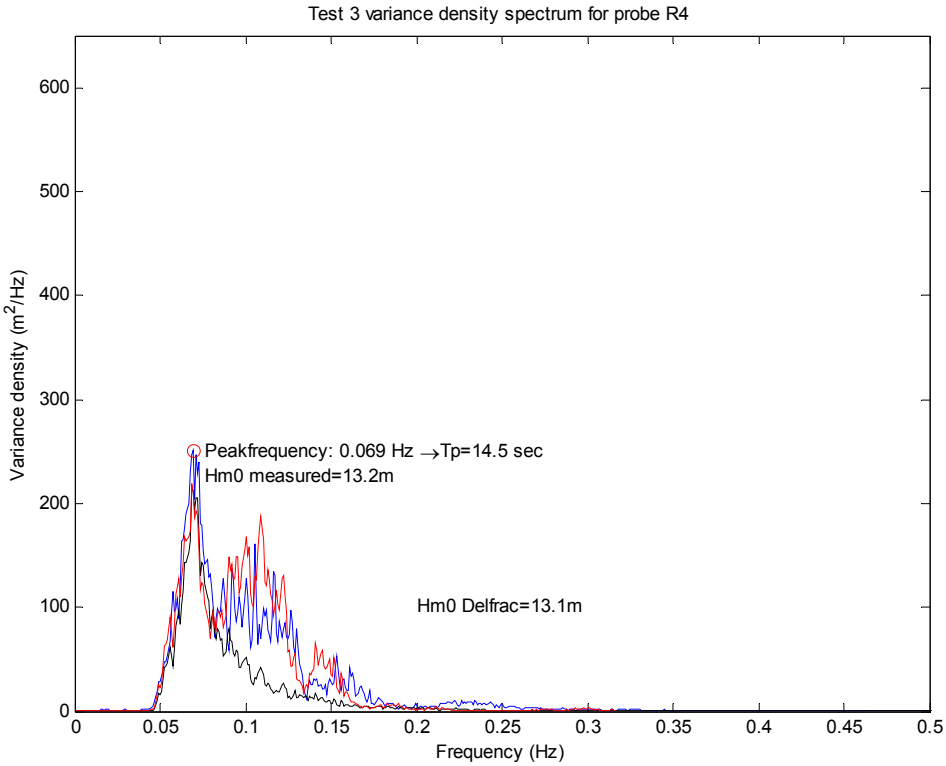

Figure 28: Spectra R4

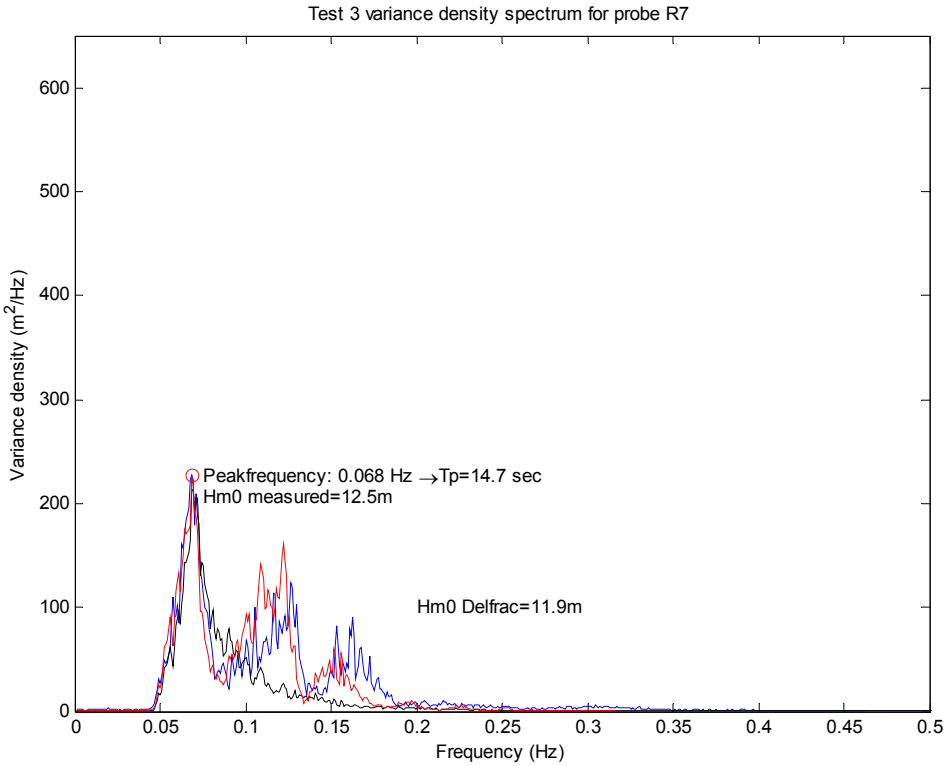

Figure 29: Spectra R7

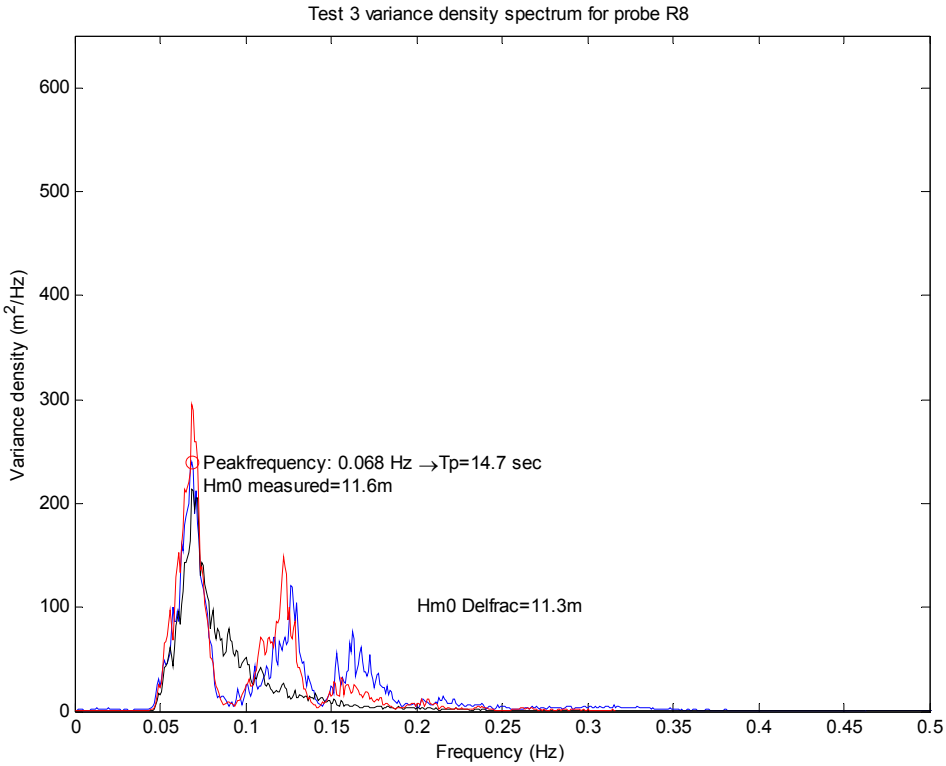

Figure 30: Spectra R8

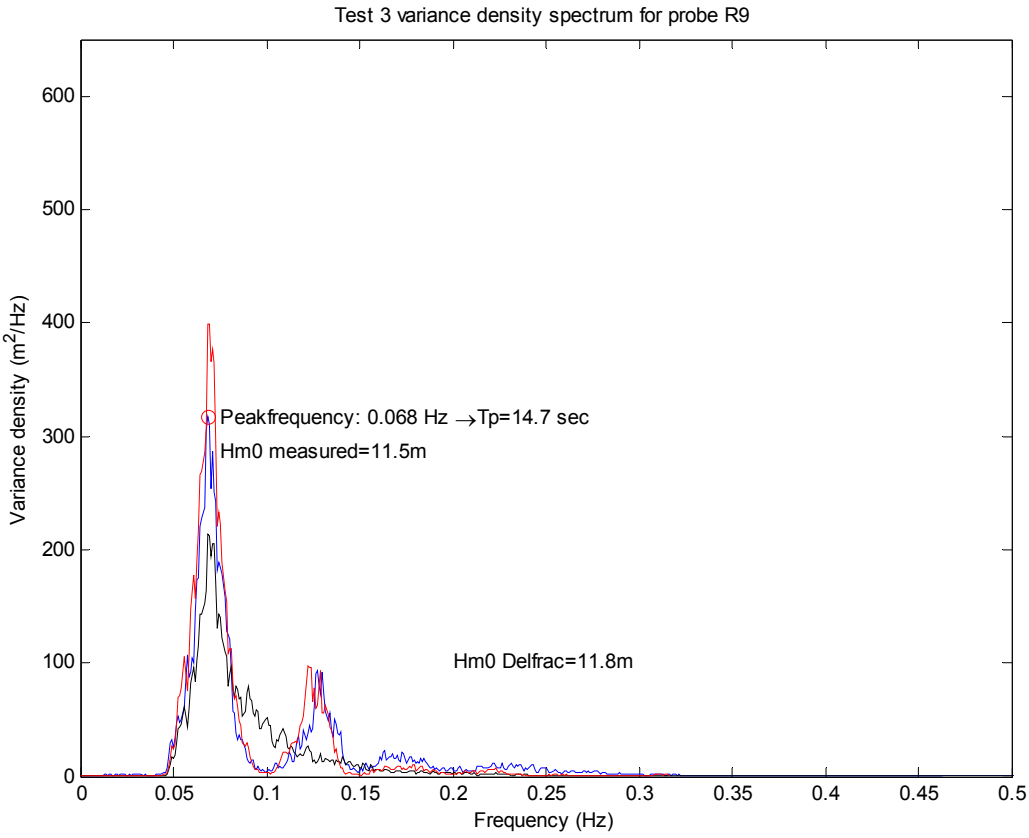

Figure 31: Spectra R9

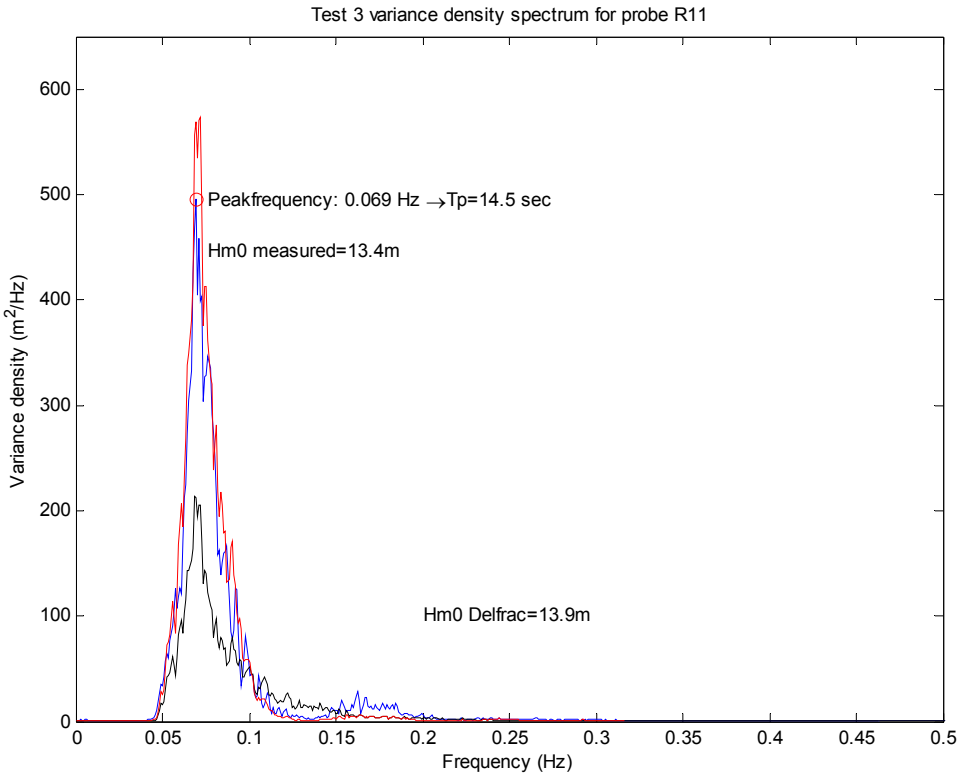

Figure 32: Spectra R11

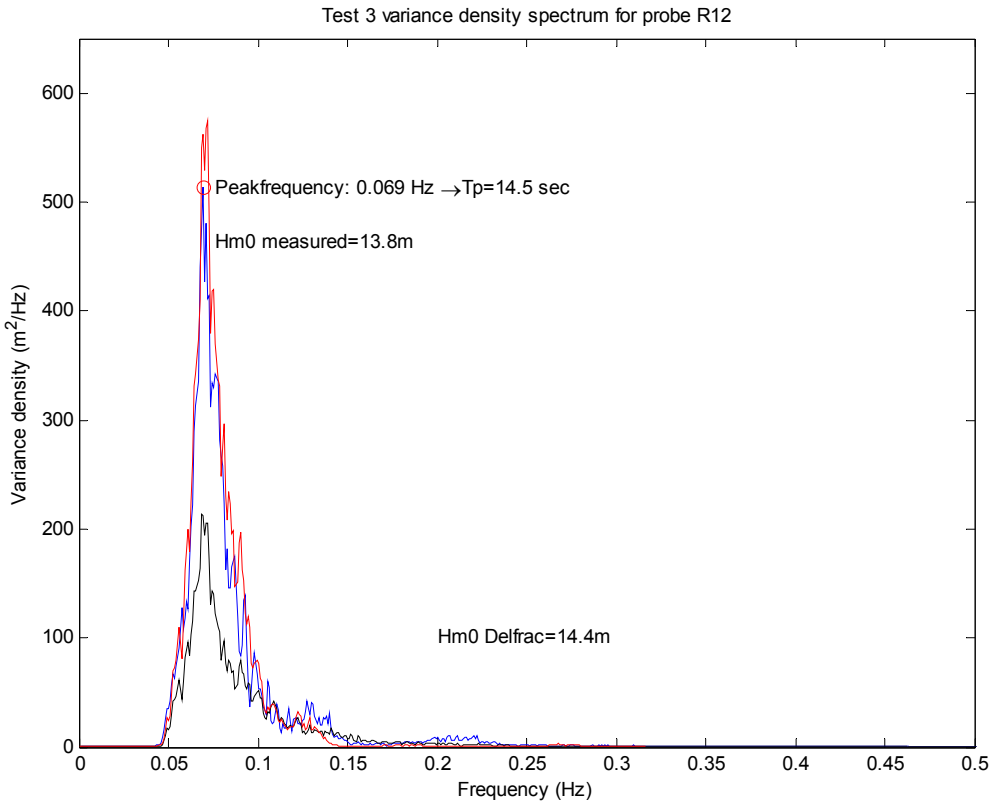

Figure 33: Spectra R12

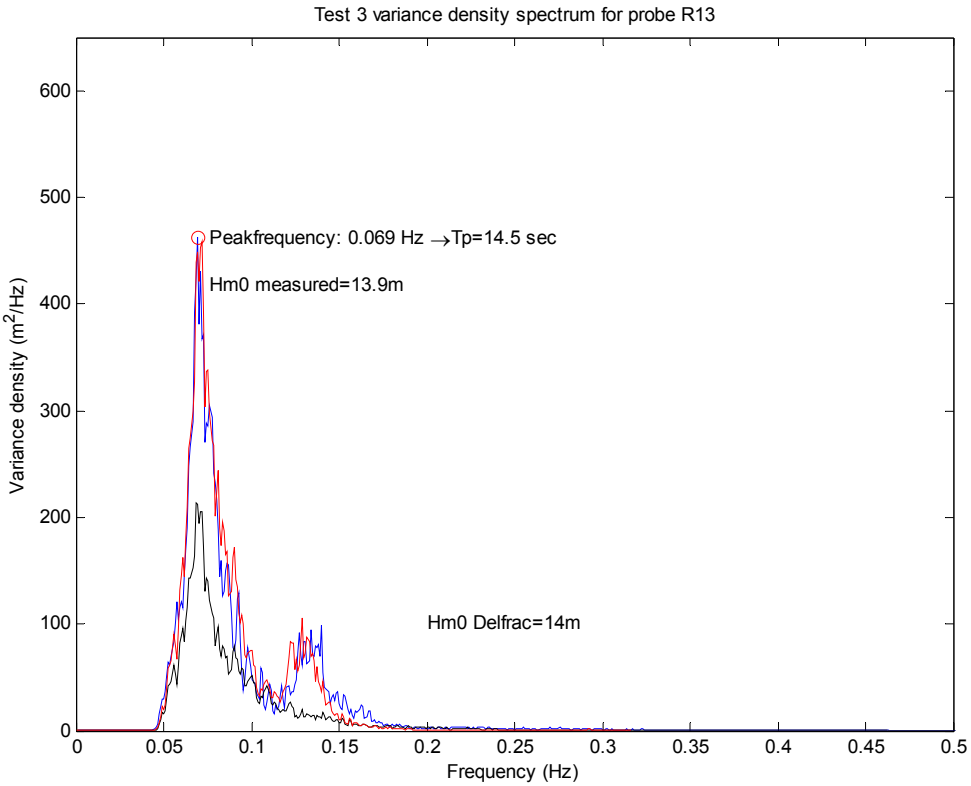

Figure 34: Spectra R13

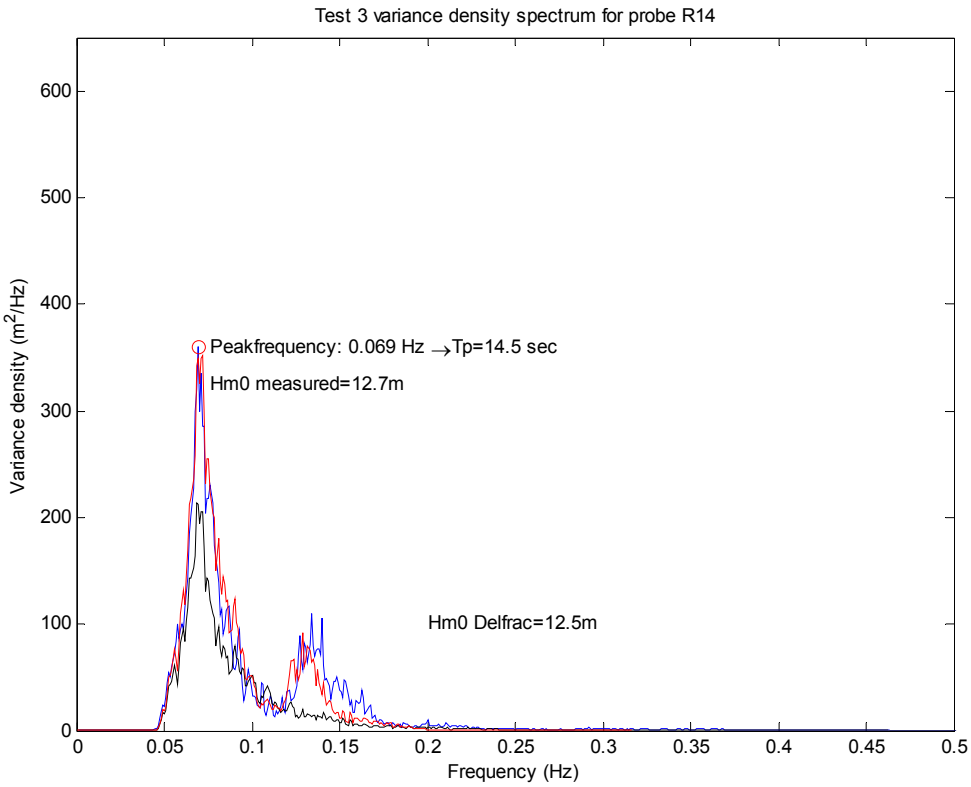

Figure 35: Spectra R14

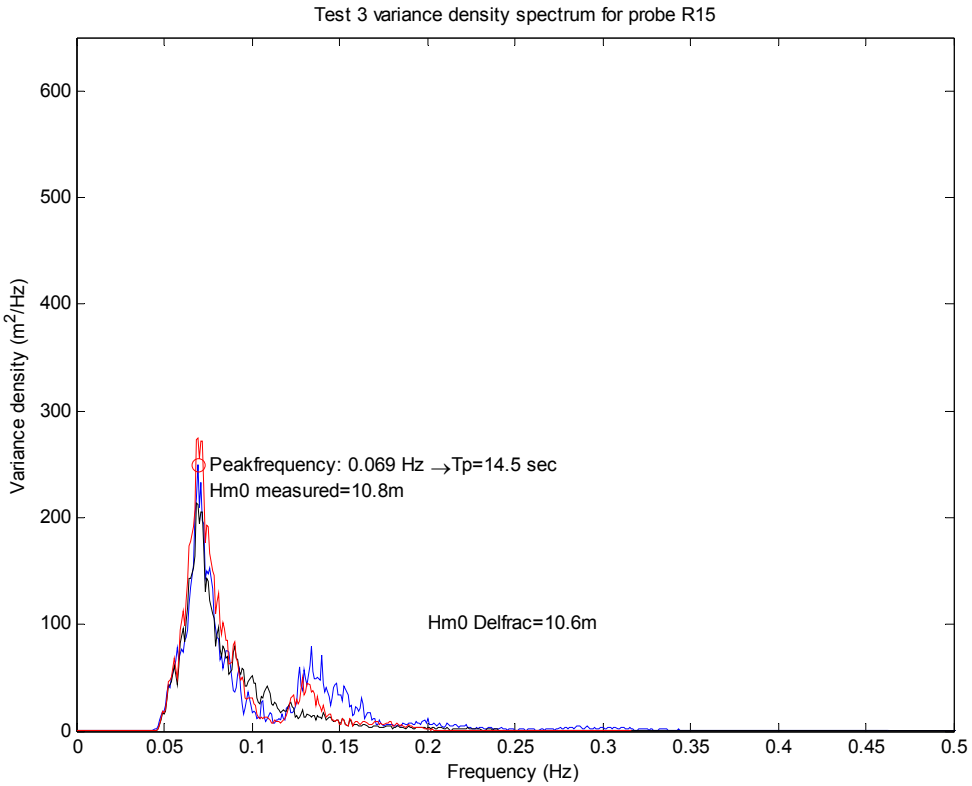

Figure 36: Spectra R15

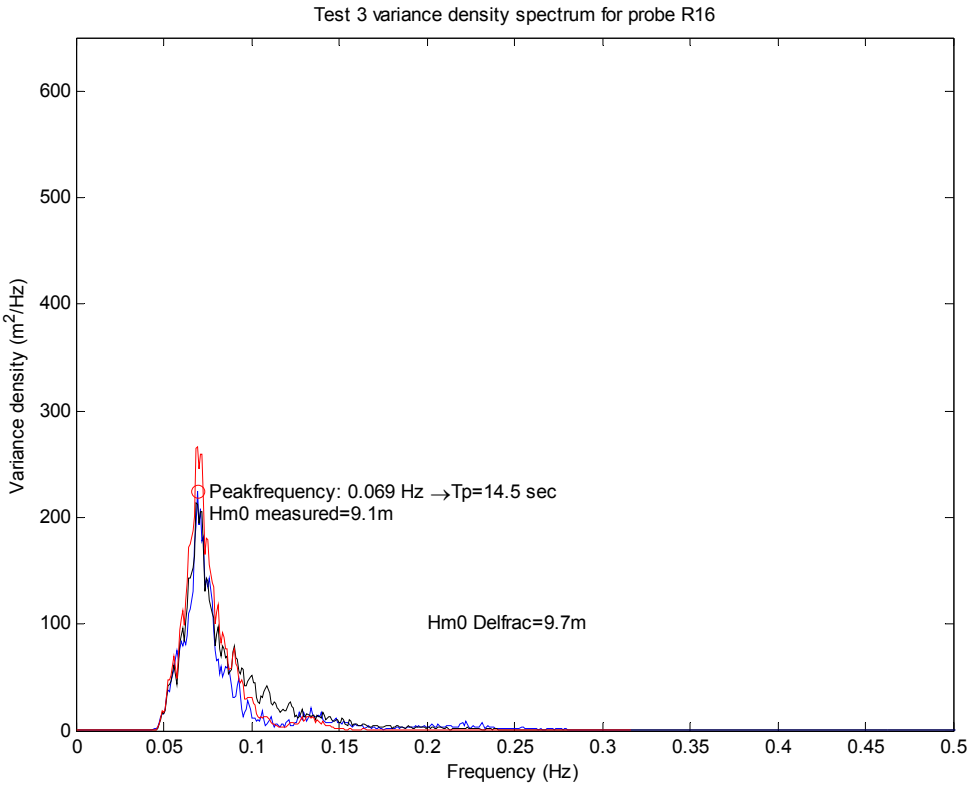

Figure 37: Spectra R16

Some observations that were made from comparison of the DELFRAC and the measured spectra are summarized in Table 8.

Table 8: Observations from the 100-year spectra

Fit to the first peak		Remarks
Good	**Poor**	
R4		2nd peak overestimated, 3rd peak and higher underestimated by DELFRAC
R7		2nd peak overestimated, 3rd peak and higher underestimated by DELFRAC
R8		2nd peak overestimated, 3rd peak and higher underestimated by DELFRAC
R9		Overall a very good fit, DELFRAC misses some energy at high frequencies
R11		Overall a very good fit, DELFRAC misses some energy at high frequencies
R12		Overall a very good fit, also at high frequencies
R13		Overall a very good fit, DELFRAC misses some energy at high frequencies
R14		Overall a very good fit, DELFRAC misses energy at high frequencies
R15		Overall a very good fit, DELFRAC misses energy at high frequencies
R16		Overall a very good fit, also at high frequencies

In Section 4.2.1, the amplification factor of the measured, first-order harmonic component was derived for regular waves along the centreline and compared to the amplification factor as predicted by DELFRAC. A similar comparison can be made for the irregular waves. We define:

$$\overline{\eta_a{}^2}(x,y) = \sum_n S_a(x,y,f_n)\Delta f = m_{0a} \qquad \{9\}$$

which is the average of the squared amplified surface elevation measurements with the structure in place, or the 0th moment of the measured amplified wave variance density spectrum. S_a is the variance density of the amplified waves at location (x,y) at frequency f_n. and Δ f is the frequency step size.

$$\overline{\eta_i^2} = \sum_n S_i(f_n)\Delta f = m_{0i} \qquad \{10\}$$

which is the average squared incident surface elevation, or the 0th moment of the incident wave variance density spectrum. S_i is the variance density of the incident waves at frequency f_n.

$$\overline{\eta_D^2}(x,y) = \sum_n \phi_n^2(x,y) S_i(f_n)\Delta f = m_{0D} \qquad \{11\}$$

which is the average squared amplified surface elevation as predicted by DELFRAC, or the 0th moment of the variance density spectrum as calculated by DELFRAC. $\phi_n(x,y)$ is the amplification factor calculated by DELFRAC.

We define an average amplification factor that allows for comparison of the DELFRAC results to the measurements.

For the measurements: $amplification\_factor = \sqrt{\frac{m_{0a}}{m_{0i}}}$ {12}

For DELFRAC: $amplification\_factor = \sqrt{\frac{m_{0D}}{m_{0i}}}$ {13}

The 0^{th} moment calculated from the measurements is known at 10 locations along the centreline. The DELFRAC predicted 0^{th} moment is known at 17 locations along the centreline. The combined result is shown in Figure 38.

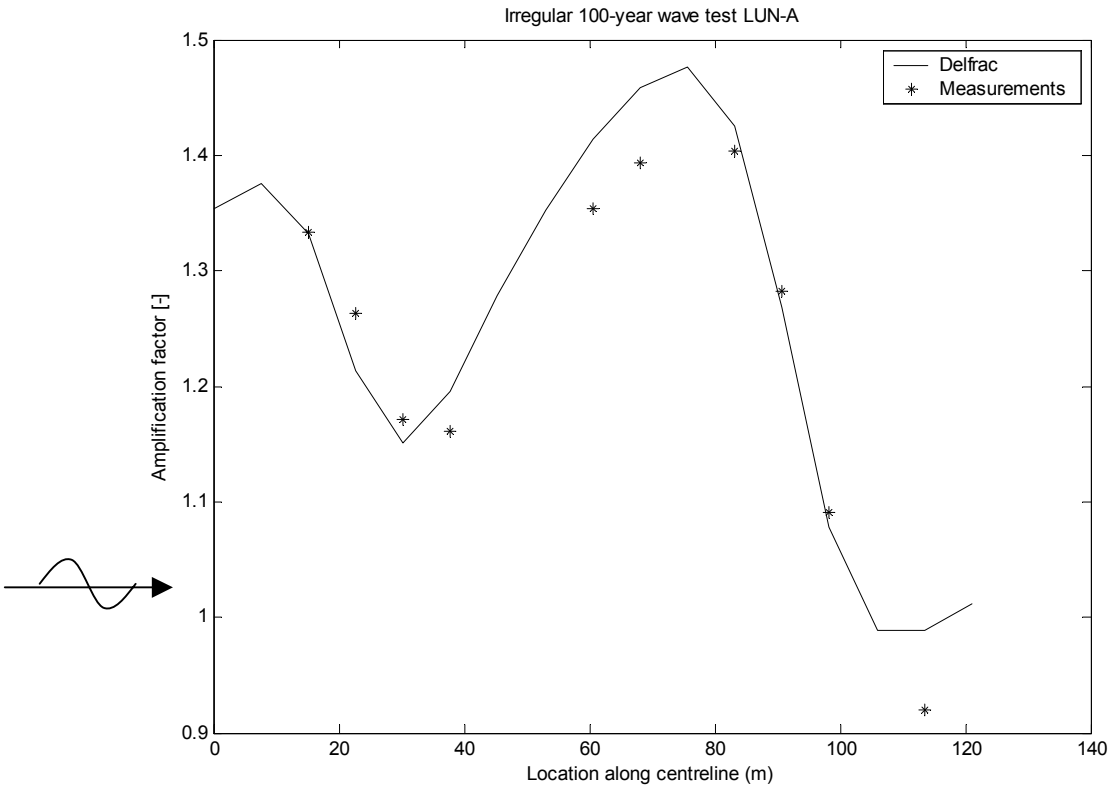

Figure 38: Amplification factor for irregular waves

Figure 38 shows DELFRAC is in close agreement with the measurements. It is noted that the profile is very similar to the profile derived by Ohl et al. [5], despite the different geometry. Ohl et al. used a model with square leg spacing (ratio lateral- to longitudinal spacing is 1:1) as shown in Figure 18, and the LUN-A model has rectangular spacing (ratio lateral- to longitudinal spacing is 1:1.5). In the work by Ohl et al. the amplification factor was consistently under predicted by the diffraction theory. They therefore filtered out the high frequency components ($f>1.5*f_{peak}$) and found a much better fit between measurements and theory.

Table 9 summarizes the observations that can be made from comparison of DELFRAC with the regular wave tests, this allows for comparison of the results from the irregular waves to the regular waves.

Table 9: Observations from the regular wave test

1st order amplitude fit			2nd order amplitude		
Good	**Poor**	Remarks	High	Med.	Low
	R4	DELFRAC too low		R4	
	R7	DELFRAC too low	R7		
R8			R8		
R9				R9	
R11		H=14 better than H=10		R11	
R12		Factor for H=14>H=10			R12
R13				R13	
R14			R14		
R15			R15		
	R16	DELFRAC too high			R16

The observations made from irregular wave tests seem to be consistent with those made from the regular wave tests. The close agreement between linear diffraction theory and the measurements for the irregular wave test at probes R12 and R16 can be explained by the relative low amount of second order energy. The slight disagreement at higher frequencies for probes R7, R8, R14 and R15 seems to be caused by a larger amount of second order energy. As mentioned before, Ohl et al. [5] accounted for this by filtering out the energy at the frequencies higher than $1.5*f_{peak}$. That exercise is not performed here.

We note that the measured spectra show bumps of increased energy near twice the incident peak frequency and that these bumps are well predicted by linear diffraction theory. The nature of these bumps is discussed in Section 4.2.3.

4.2.3. Spectra at the rear legs

The preceding work in chapter 4 focuses on the amplification of waves at locations along the centreline of the structure. This allows for global trends to be identified. The work shows that DELFRAC gives good results for the diffracted irregular wave spectra and for the regular wave diffraction to first-order. The present study sets out to develop a prediction method for the maximum surface elevation underneath the deck, therefore this section considers the spectra at the rear legs, which show the highest value for the significant wave height H_{m0} around the structure. The CHC probe name of the rear legs is R21 for the left rear leg and R25 for the right rear leg, as shown in Figure 19. For both locations, the undisturbed spectrum is plotted in black, the measured spectrum in blue and the DELFRAC predicted spectrum in red in Figure 39 and Figure 40.

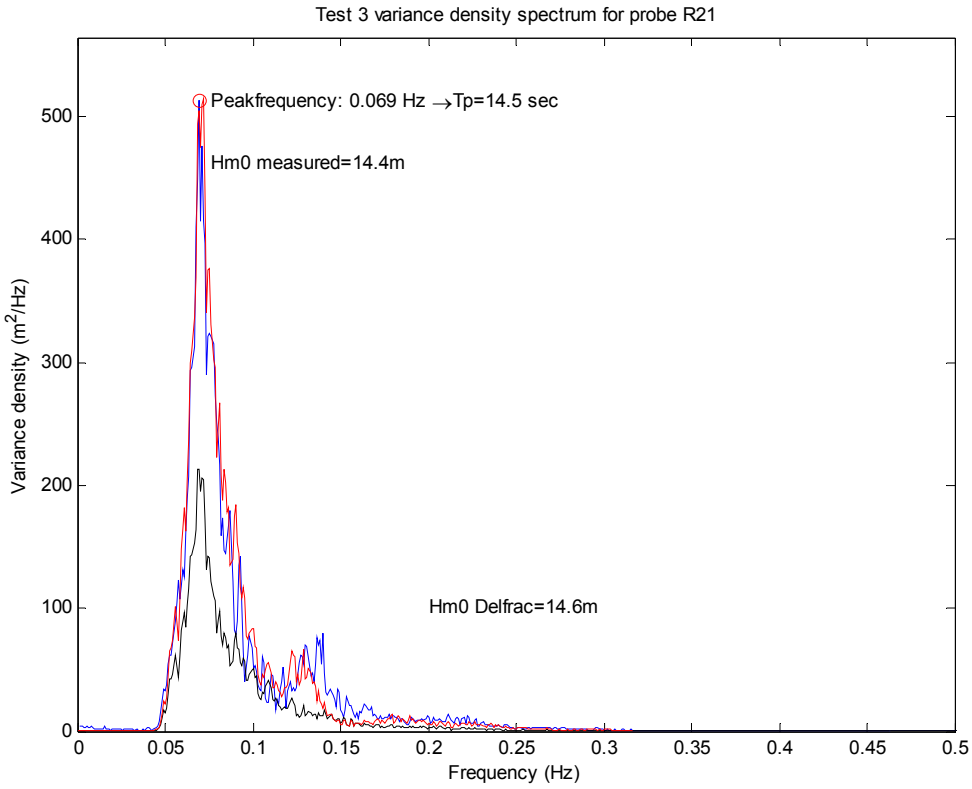

Figure 39: Spectra at left rear leg

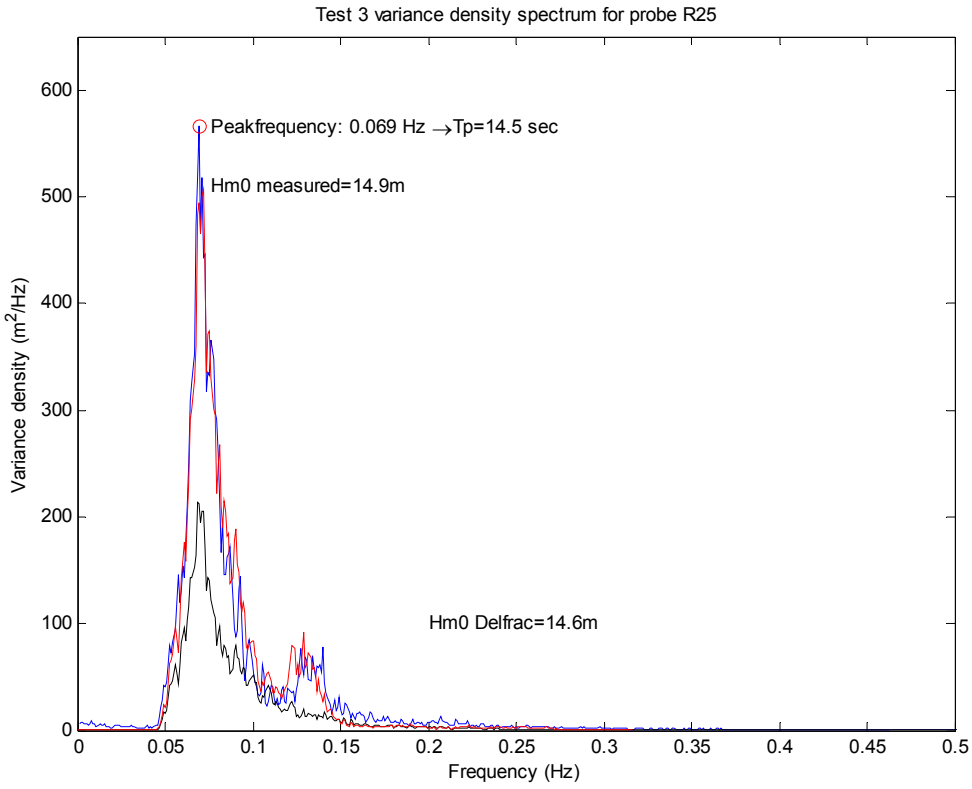

Figure 40: Spectra at right rear leg

The measured spectra clearly show an increase in energy at approximately twice the peak frequency of the undisturbed spectrum. One might assume that this is due to second order effects, except that DELFRAC, which is a linear diffraction code, also quite accurately predicts this increase. The next two paragraphs study the nature of this so-called bump at twice the incident peak frequency using the measurements only.

The slightly larger amount of energy in the measured spectrum at R25 is likely to be due to the fact that this probe is located just in front of the steel column supporting the deck, whereas the R21 probe is located more away from the steel column. As discussed in Section 3.2, these steel columns are not modelled in DELFRAC. Due to the dimensions of the steel column compared to the wavelength of the larger incident waves, the effect is likely to be limited to a small area.

4.2.3.1. Relating the energy in the bump at twice the incident peak frequency to the total incident energy

Figure 41 shows the undisturbed spectra for wave tests 1 through 3 in the upper row. The lower row shows the diffracted spectra at probe R21 for the same wave cases. The same procedure is followed for R25 in Figure 42.

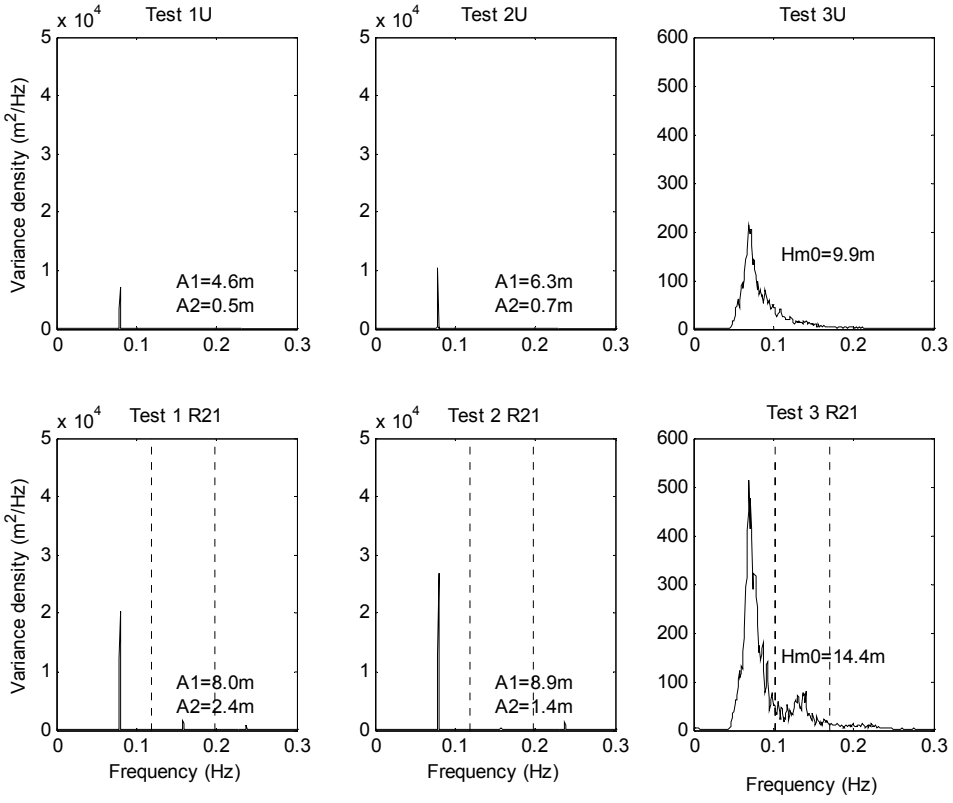

Figure 41: Matrix of incident and diffracted spectra R21

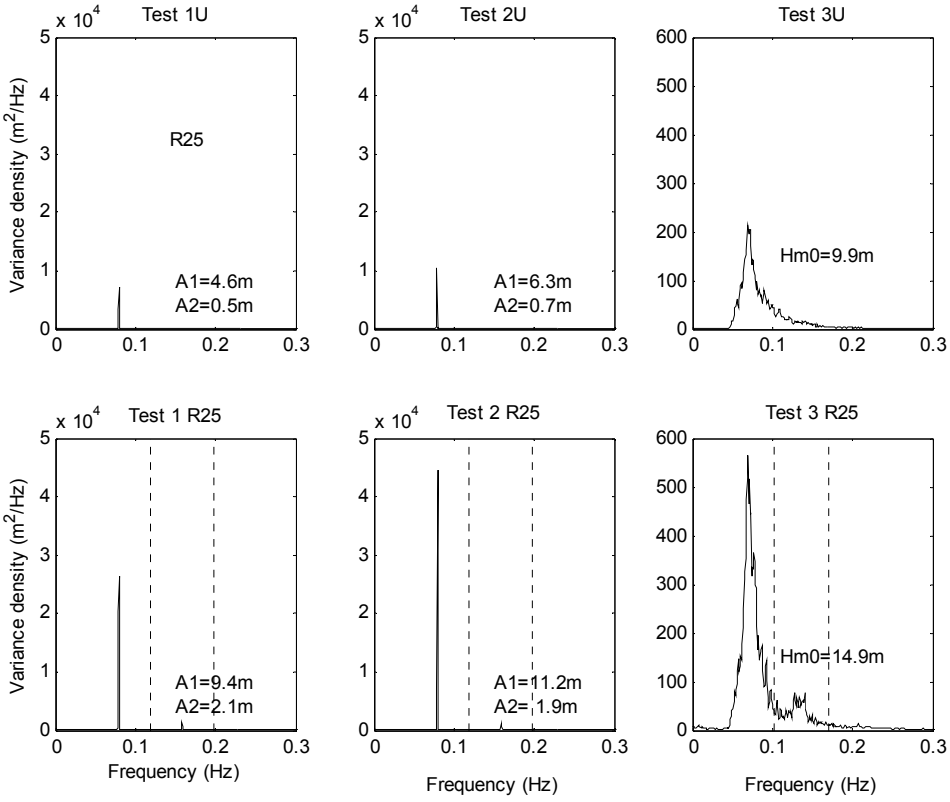

Figure 42: Matrix of incident and diffracted spectra for R25

The energy between the dashed lines in the diffracted spectra is now related to the undisturbed energy in the following way:

$\alpha_{regular} = \frac{m_{diffracted}(1.5f_1 < f < 2.5f_1)}{m_{incident}(f = f_1)}$ for the regular wave case. This implies the energy at the second harmonic of the diffracted wave is related to the energy at the first harmonic of the undisturbed wave, which is approximately all the energy in the incident wave. For the undisturbed regular wave cases, the energy at higher frequencies than the first harmonic is insignificant compared to the energy at the first harmonic, with a ratio of approximately 1:85, and therefore not included in the calculations.

$\alpha_{irregular} = \frac{m_{diffracted}(1.5f_p < f < 2.5f_p)}{m_{incident}}$ for the irregular wave case. This implies that the energy in the bump near twice the incident peak frequency is related to all the energy in the incident spectrum.

The ratios are shown in Table 10.

Table 10: Diffracted energy band over incident energy

	R21	**R25**
Test 1 α	0.27	0.21
Test 2 α	0.05	0.09
Test 3 α	0.38	0.36

Since the energy at the second harmonic of the undisturbed regular wave is so small compared to the energy at the first harmonic, it can be concluded that the energy at the second harmonic of the diffracted regular wave is largely due to non-linear effects. The value of α gives the amount of energy at a frequency band centred around twice the peak- or incident frequency over the total incident energy. The measurements show that the value of α is higher for the irregular wave case than for the regular wave cases, as presented in Table 10. This is a first indication from the measurements that at least some of the increase in energy in the 2nd bump of the diffracted irregular wave spectra at probes R21 and R25 is due to linear diffraction.

4.2.3.2. Comparing different irregular sea states

As shown in Table 5, the LUN-A structure has been tested for two multidirectional irregular wave cases, the 100-year and the 10,000-year conditions. Holthuijsen et al. [22] discussed some of the theory on the flow of energy through a JONSWAP spectrum in deep water as waves grow. The wind transfers energy to the waves mostly at the high-frequency flank of the spectral peak. The energy gain at these frequencies is rapidly removed by whitecapping, wave breaking in deep water, and quadruplet interactions, interactions between four wave components that redistribute energy over the spectrum. The quadruplet interactions only transfer energy to the lower and higher frequencies, no energy is withdrawn from or added to the spectrum as a whole. The energy transferred to the lower frequencies is almost completely used to migrate the spectral peak to a lower frequency. The energy transferred to higher frequencies is almost totally dissipated by whitecapping. This flow of energy results in a state of equilibrium of the high frequency tail of the spectrum; it does not change, the growth of spectral energy occurs on the low frequency flank of the spectral peak. Figure 43 shows that the 100-year and 10,000-year sea-sates behave accordingly.

Linear diffraction theory implies there is no transfer of energy from one frequency component to another. Therefore an increase in energy in a certain frequency band is caused by amplification of waves already present in that band; the diffracted energy is not related to energy outside the band. Thus at each location, according to linear diffraction theory, the two sea-states shown in Figure 43, even though their total incident energy is different, would have similar bumps in their diffracted spectra because their undisturbed high frequency tails are the same. Figure 44 shows the bumps to be approximately the same for the different sea-states, which is a second and strong indication that the increase in energy in the 2nd bump of the diffracted irregular wave spectra at probes R21 and R25 is due to linear diffraction.

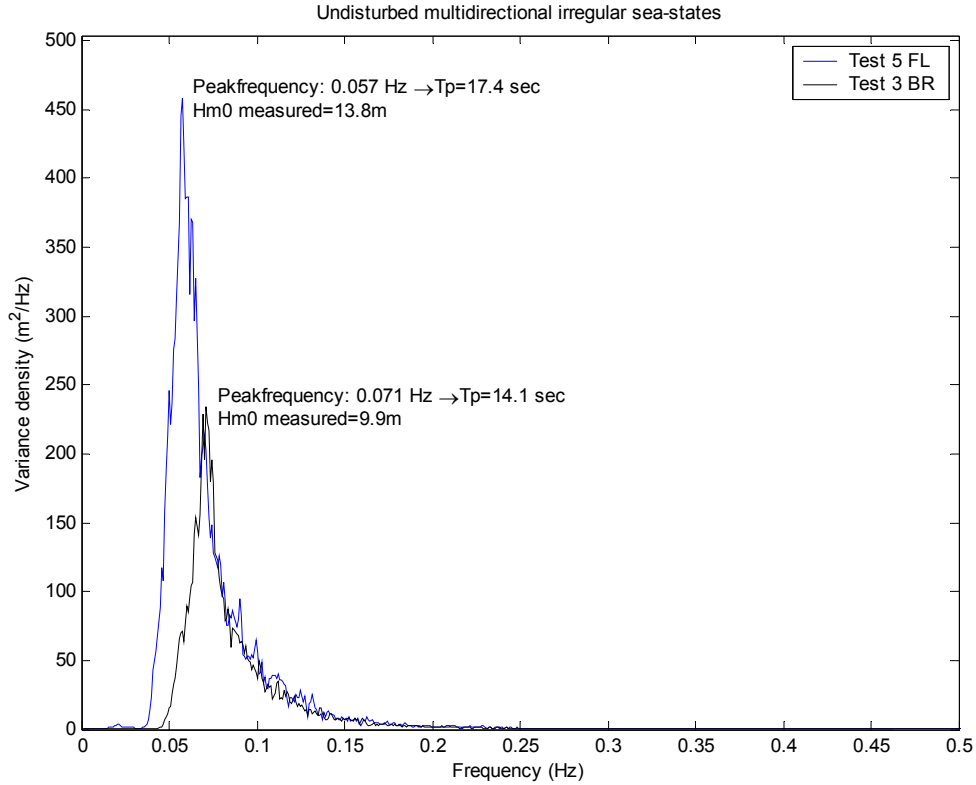

Figure 43: Two irregular undisturbed sea-states

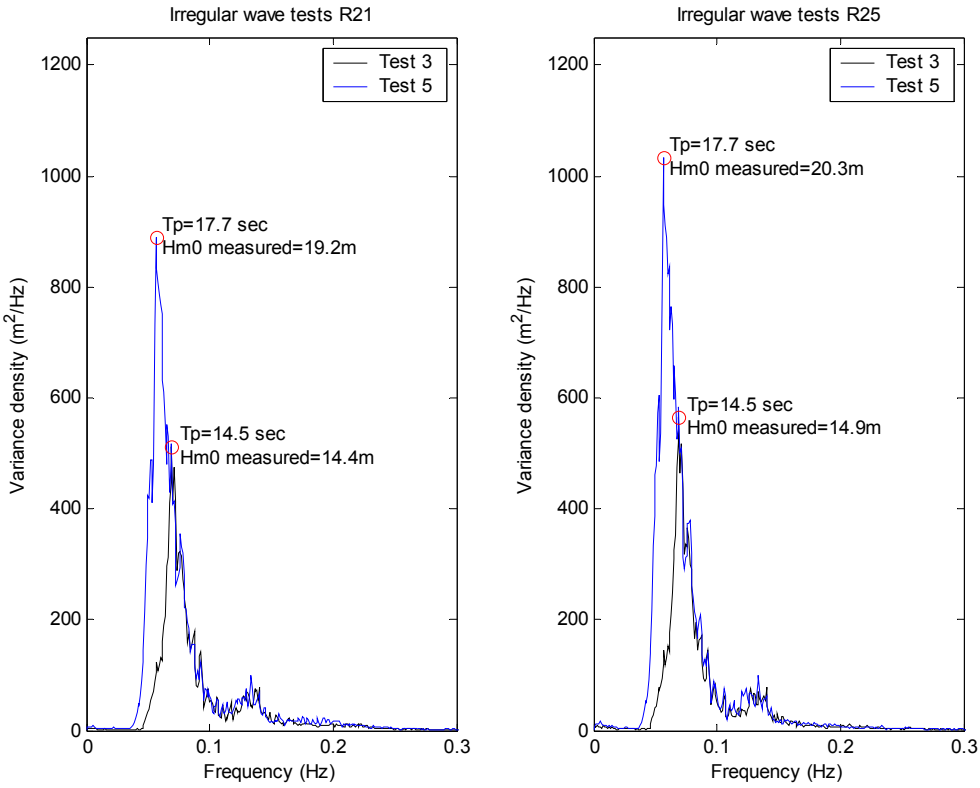

Figure 44: Diffracted spectra for two irregular sea-states at two locations

4.2.4. Contour plots

To point out principal features, contour plots of the local linear free surface amplitudes are produced at different frequencies using DELFRAC. In the following figures, the waves approach the structure from right to left and the origin of the coordinate system is located at the centre of the structure. The solid circles represent the column positions, the contours are labelled with magnitude in terms of the amplification modifying the incident wave. For example, a contour labelled 1 indicates no modification to the incident wave amplitude, whereas a value of 1.4 represents a 40% increase in amplitude.

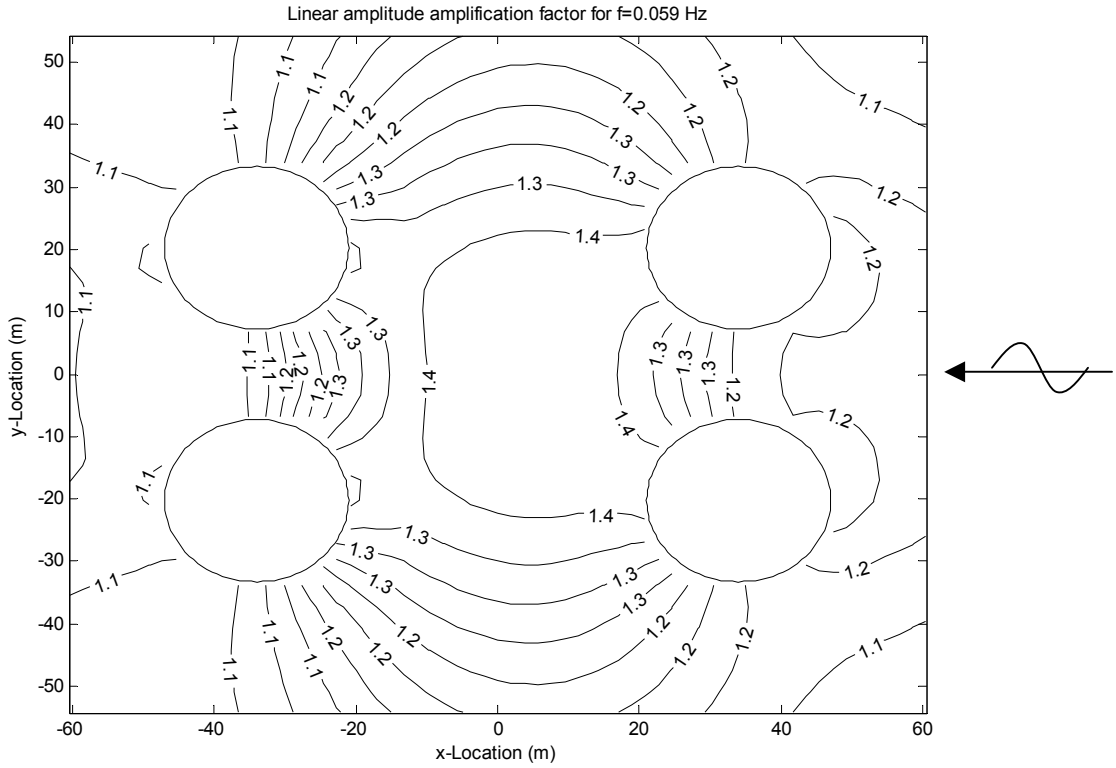

Figure 45: Contour plots at the peak frequency of a 10,000-year storm

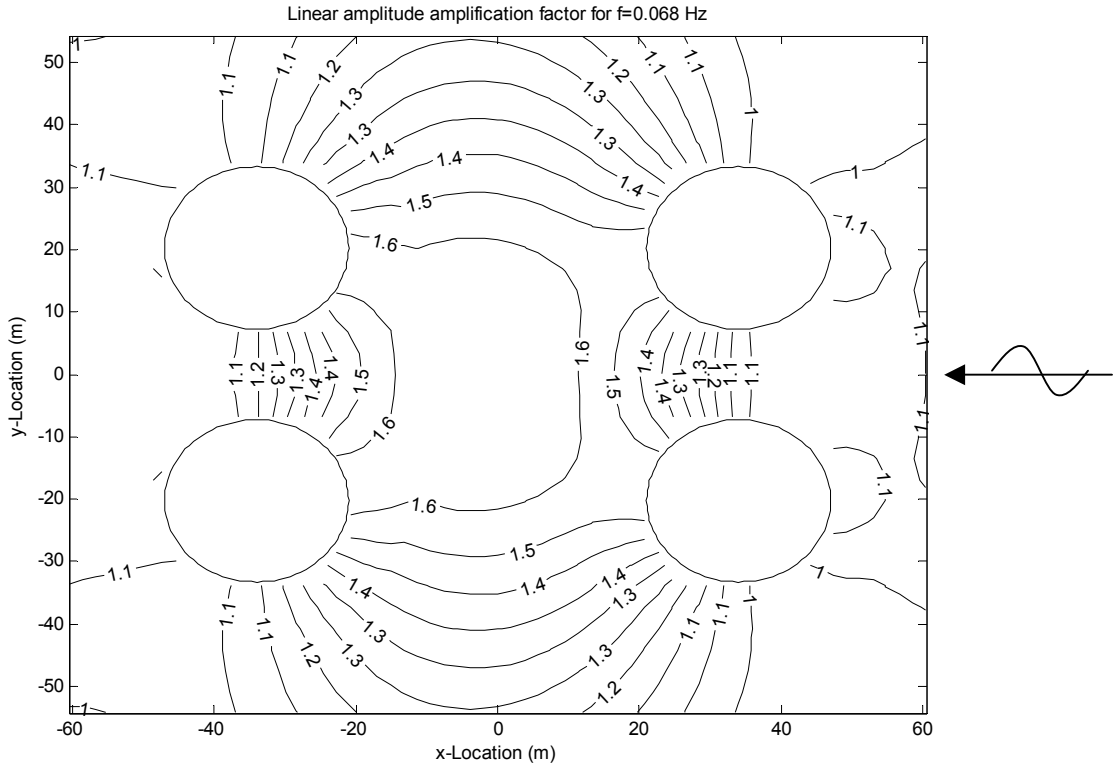

Figure 46: Contour plots at the peak frequency of a 100-year storm

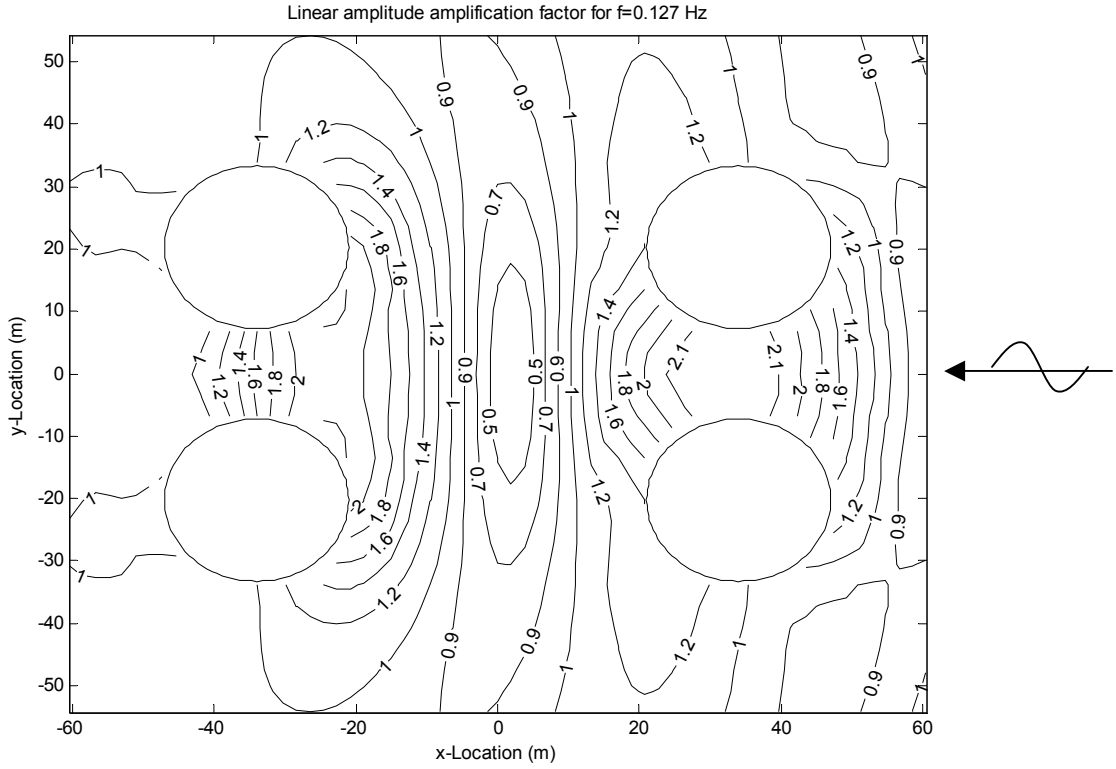

Figure 47: Contour plots at the peak frequency of the 2nd bump

Figure 45 and Figure 46 show the diffraction process is not too much different for regular incident waves with a frequency of 0.059Hz or 0.068Hz respectively. The period of these waves is 17 seconds and 14 seconds, their respective wavelength in water of 53m depth is 270m and 340m. For regular incident waves with a higher frequency of 0.127Hz, which is twice the 100-year incident peak frequency, a period of 8 seconds and a wavelength of 97m, the diffraction process is entirely different as shown in Figure 47.

- The amplification of low frequency waves reaches a maximum at the centre of the structure radiating outwards.
- The high frequency wave amplitudes are greatly reduced at the centre of the structure to approximately 50% of their incident value. Large amplification occurs in between the two up-wave columns and in front of the down-wave columns.

A three-dimensional visualisation of these processes is shown in Figure 48 for incident waves with a frequency of 0.068Hz and in Figure 49 for a frequency of 0.127Hz.

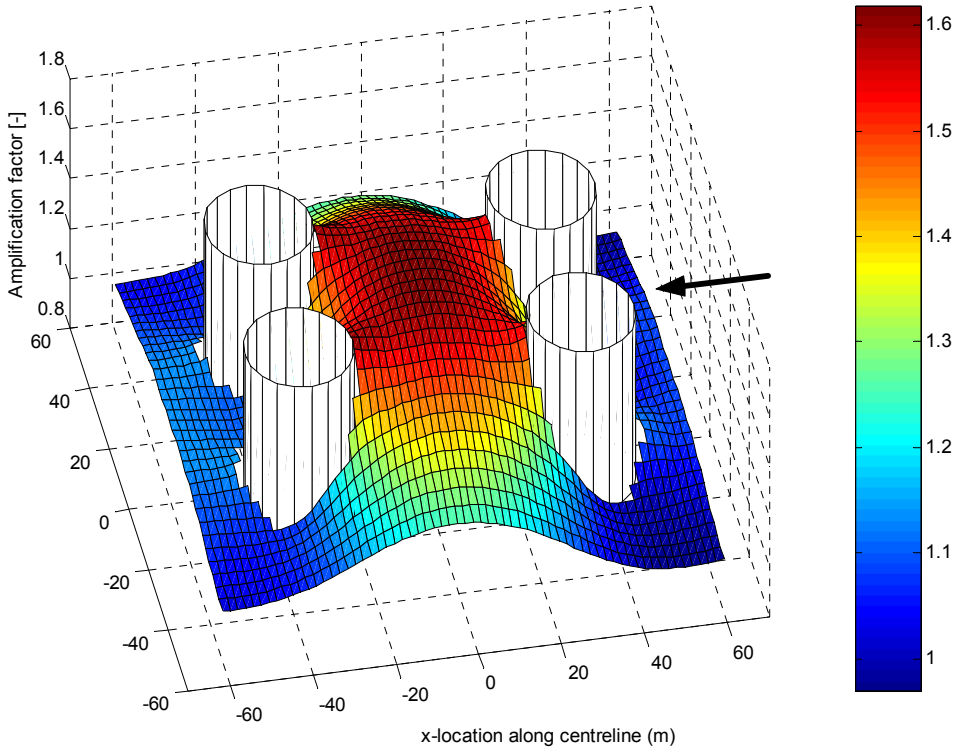

Figure 48: Amplitude amplification at f=0.068Hz

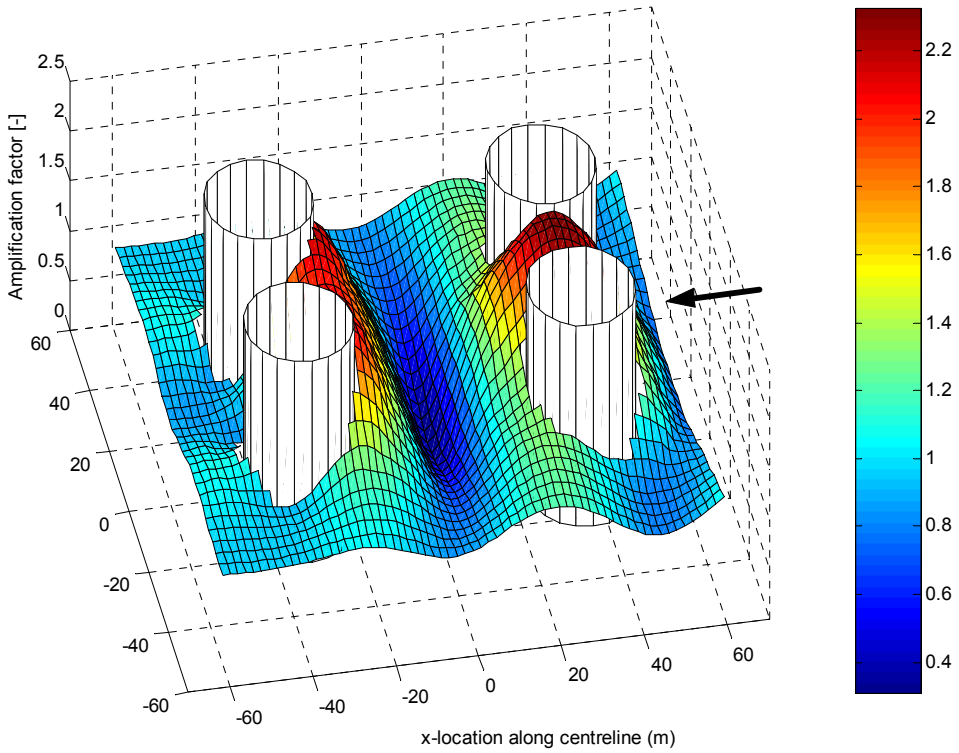

Figure 49: Amplitude amplification at f=0.127Hz

In addition to the contour plots of the amplitude amplification factor, contour plots of the phases also yield valuable information about convergence or divergence of wave energy. The following figures show contour plots of lines with equal phases. The lines are labelled with the value of their phases in degrees. A wave ray can be constructed as the normal to the iso-phase lines.

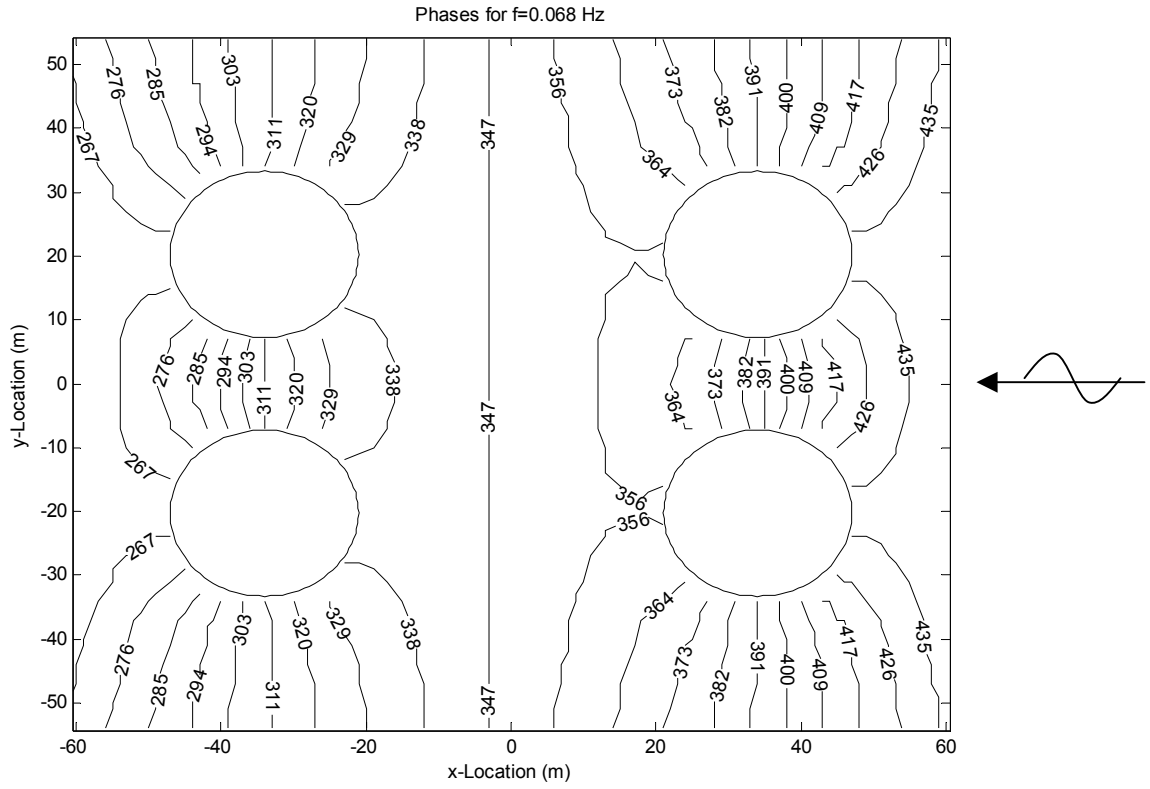

Figure 50: Iso-phase lines at the peak frequency of a 100-year storm

Figure 50 supports the idea that waves with a period equal to the peak period of the 100-year incident spectrum tend to bend around the two up-wave columns towards the centre of the structure where they are then blocked by the two rear columns. The converging wave rays represent the focussing of wave energy and therefore result in amplification of the waves. This interpretation is consistent with the results from the amplitude amplification factor analysis.

For waves with a period equal to the peak frequency of the 2nd bump the picture is again very different as shown in Figure 51. Here wave rays seem to be forced closer together in between the two up-wave columns. The convergence of the wave ray results in convergence of energy and therefore amplification of the amplitudes. The rays propagating along the outside of the columns appear to be unaffected by the structure, they proceed in their original direction. Behind the up-wave cylinders the rays diverge, which results in an decrease of wave amplitude. A similar process of first convergence followed by divergence starts once the wave rays reach the down-wave columns. Again the interpretation of the wave rays is consistent with the results from amplitude amplification factor analysis.

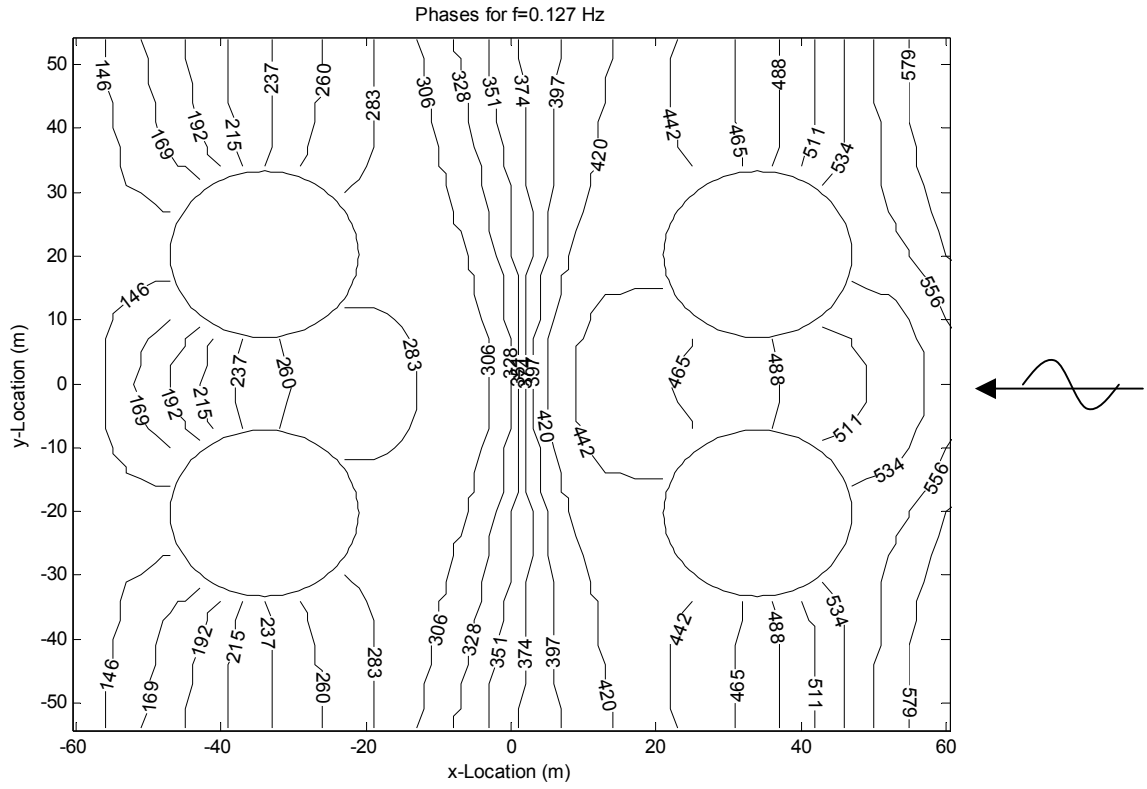

Figure 51: Iso-phase lines at the peak frequency of the 2nd bump

5. FROM SPECTRUM TO PROBABILITY DISTRIBUTION

One can treat the phases of the various spectral components as stochastically independent, random variables without preferred values. Independence implies that the components do not influence each other, which is approximately the case for relatively low waves described by linear wave theory. Also, in a stationary process the phases cannot have preferred values. This leads to the formulation of the random phase model. According to this model, the surface elevation is the sum of a large number of stochastically independent contributions. According to the Central Limit Theorem of probability theory, it therefore is a Gaussian process, which implies its values obey the Gaussian probability distribution. The distribution of the maximum wave height between successive zero up- or down-crossings is then given by the Rayleigh distribution:

$$P(H_{dc} > H) = \exp\left[-2\frac{H^2}{H_{m0}^2}\right] \qquad \{14\}$$

Where $H_{m0} = 4\sqrt{m_0}$, with m_0 is the 0^{th} moment of the variance density spectrum. Therefore the Rayleigh distribution can be directly derived from the variance density spectrum. According to CHC, the undisturbed wave heights are Rayleigh distributed. This assumption is verified in Figure 52 and is shown to be reasonable.

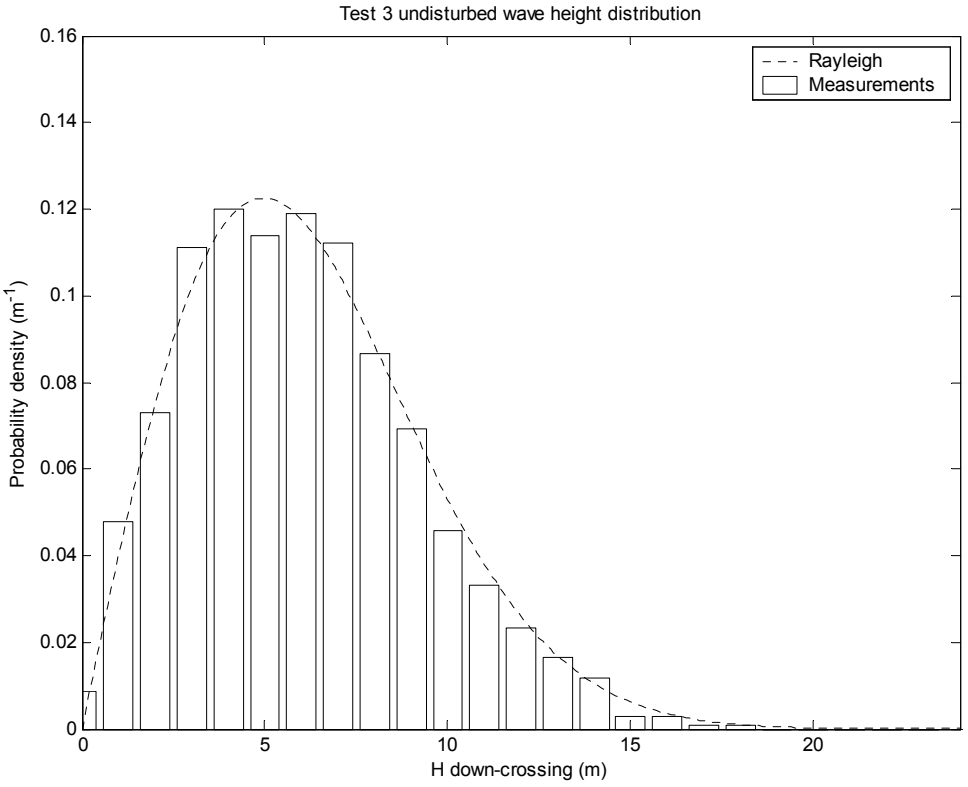

Figure 52: Undisturbed wave height distribution test 3

5.1. Rayleigh distribution

For the study of maximum green water surface elevation, the interest is not so much in the wave height but more in the crest elevation, as this determines the surface elevation above SWL. In his paper on wave crest distributions, Forristall [2] compares measurements of crest heights to the Rayleigh distribution, and a similar approach is followed here. The Rayleigh distribution for the crest height η_c is given by:

$$P(\eta_c > \eta) = \exp\left[-8\frac{\eta^2}{H_{m0}^2}\right] \quad \{15\}$$

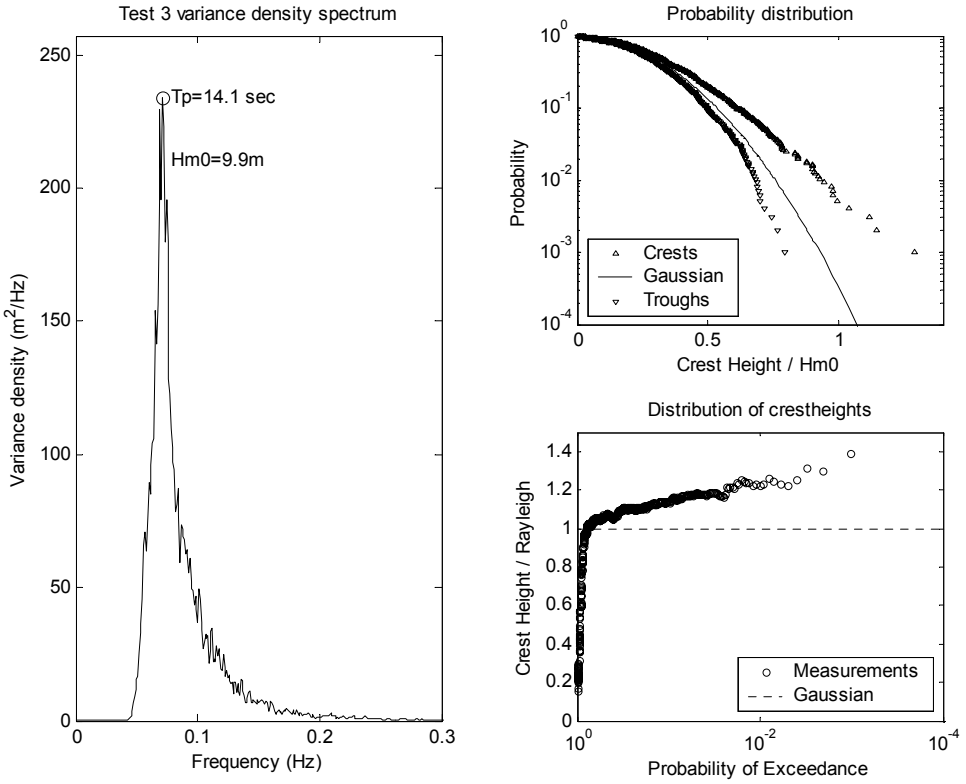

Figure 53: Undisturbed 100-year MDS and probability distributions

For the 100-year multidirectional undisturbed sea-state, Figure 53 shows the probability distribution of the crest heights and the troughs compared to a Gaussian surface in the upper right corner. The lower right corner shows the normalized crest heights against the probability of exceedance. The crest heights are normalized by the crest heights of a Gaussian surface at that probability of exceedance. For the 100-year unidirectional and 10,000-year multidirectional sea-states, the results are shown in Figure 54 and Figure 55 respectively.

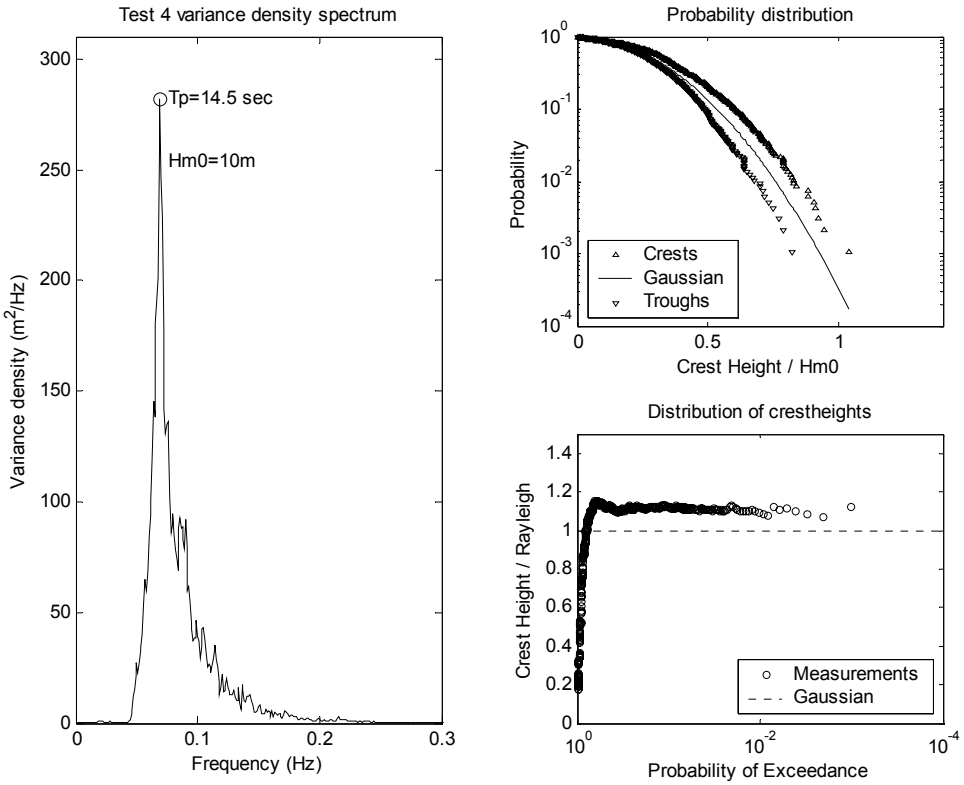

Figure 54: Undisturbed 100-year UDS and probability distributions

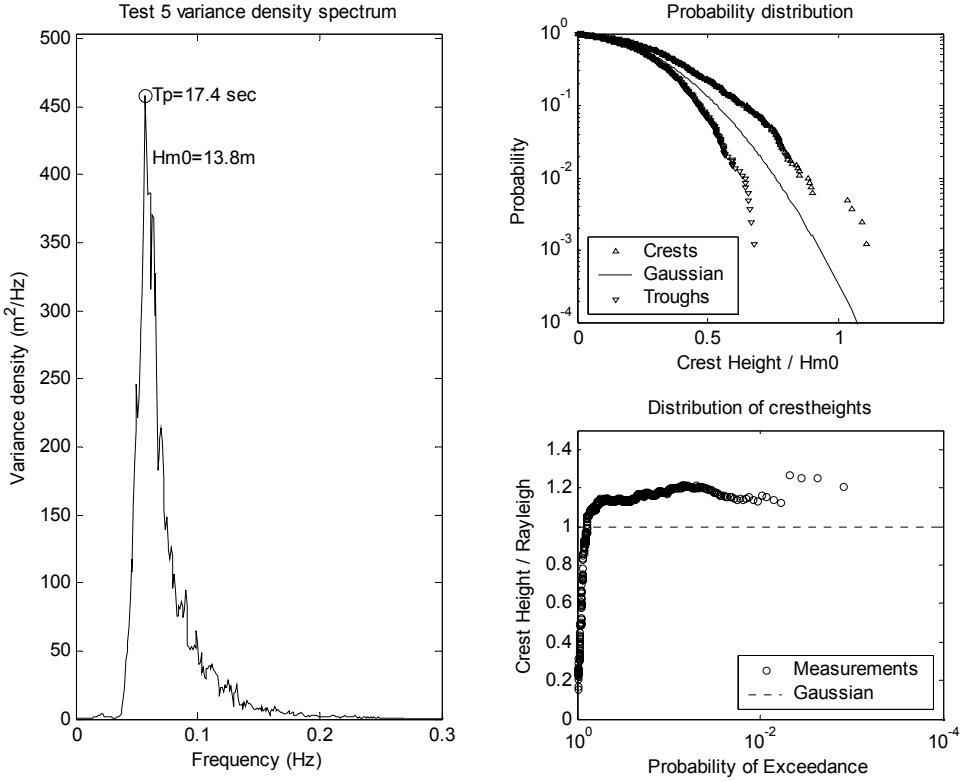

Figure 55: Undisturbed 10,000-year MDS and probability distributions

These figures show that in contrast to the wave heights, the probabilities of the crest heights are not well described by the Rayleigh distribution. The Rayleigh distribution consistently under predicts the crest height for low probabilities. An important phenomenon that could explain this mismatch is the non-linearity of the waves, which causes crest-trough asymmetry. Therefore the crests are higher than the troughs are deep.

5.2. Weibull distribution

The Rayleigh distribution has only one variable parameter that can be used to scale the distribution, this is the so-called scale parameter. It cannot be adjusted to fit a distribution with a different shape. The Weibull distribution, of which the Rayleigh distribution is a special case, does have an extra variable parameter:

$$P(\eta_c > \eta) = \exp\left[-\left(\frac{\eta}{\alpha H_{m0}}\right)^{\beta}\right] \quad \{16\}$$

In Forristall's paper [2], the first step was to fit the Weibull distribution to the measurements with sufficient accuracy. In the second step, the parameters, α and β, were related to two parameters that characterize the degree of non-linearity of the waves. That is the wave steepness:

$$S_1 = \frac{2\pi}{g}\frac{H_{m0}}{T_1^2} \quad \{17\}$$

Where $T_1 = m_0/m_1$

And the Ursell number:

$$Ur = \frac{H_{m0}}{k_1^2 d^3} \quad \{18\}$$

Where k_1 is the wave number for a frequency of $1/T_1$ and d is the water depth.

The probability distribution of the crest heights was now known once the variance density spectrum was known: The spectral moments yielded the wave steepness S_1 and Ursell number Ur, which were used to calculate the Weibull parameters α and β. These in turn gave the crest height for a certain probability of exceedance.

In the present study, the Matlab routine 'weibfit' is used to calculate the maximum likelihood estimates, which are referred to as phat(1) and phat(2), of the parameters of the Weibull distribution that best fits the crest height measurements. The results of fitting the Weibull distribution to the crest height measurements of the undisturbed waves are shown in Figure 56 through Figure 58.

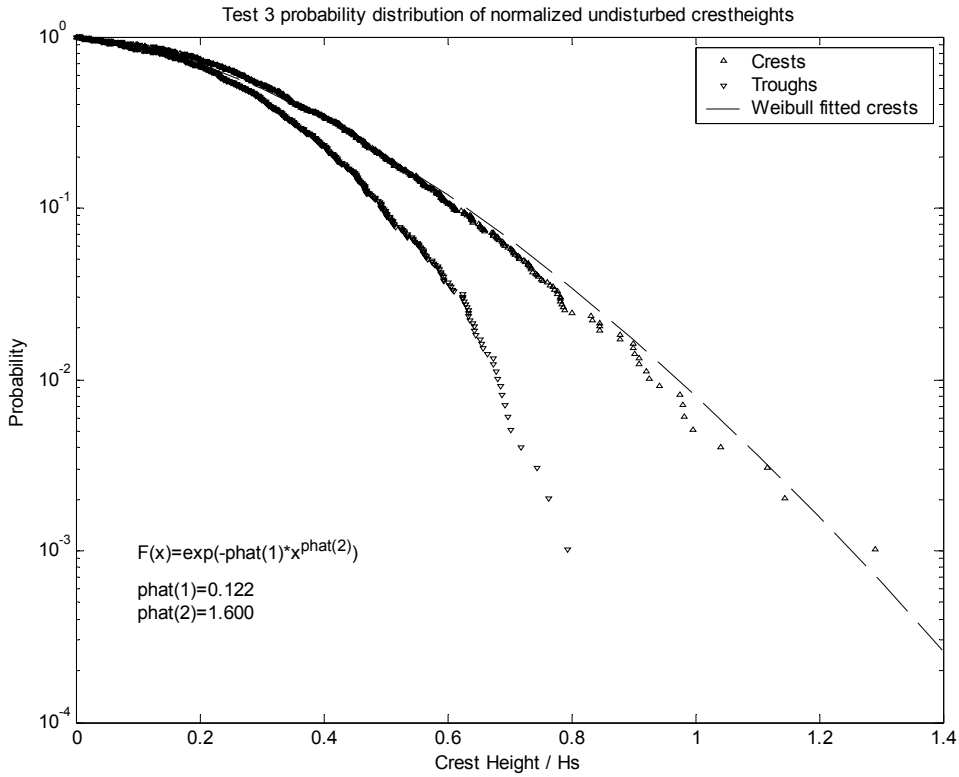

Figure 56: 100-year MDS Weibull fitted probabilities

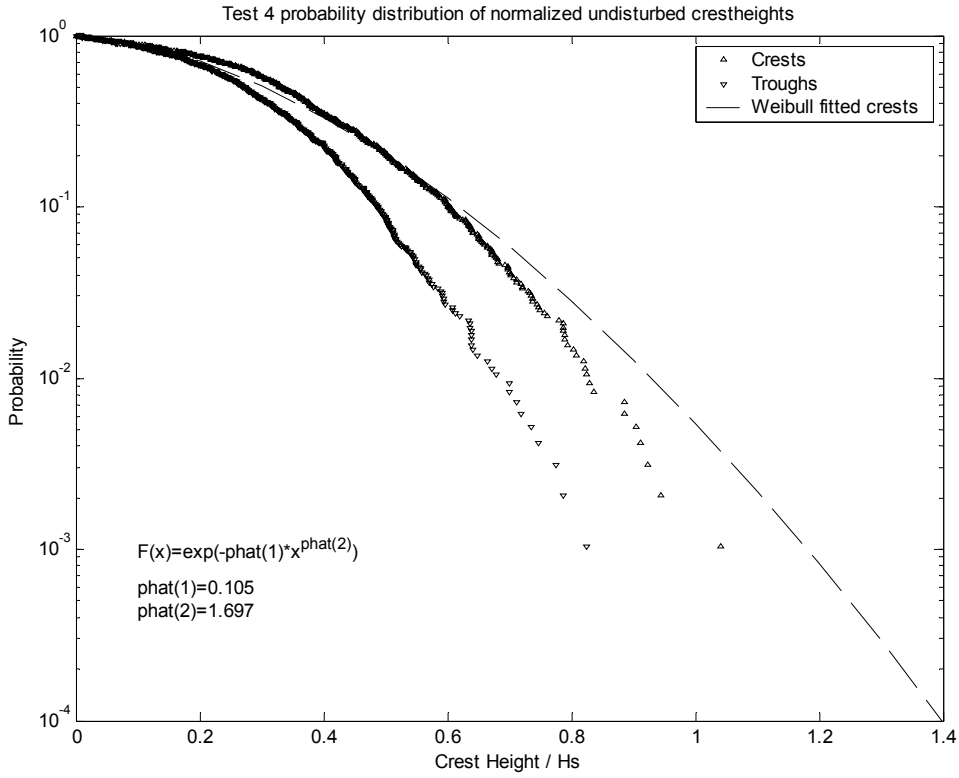

Figure 57: 100-year UDS Weibull fitted probabilities

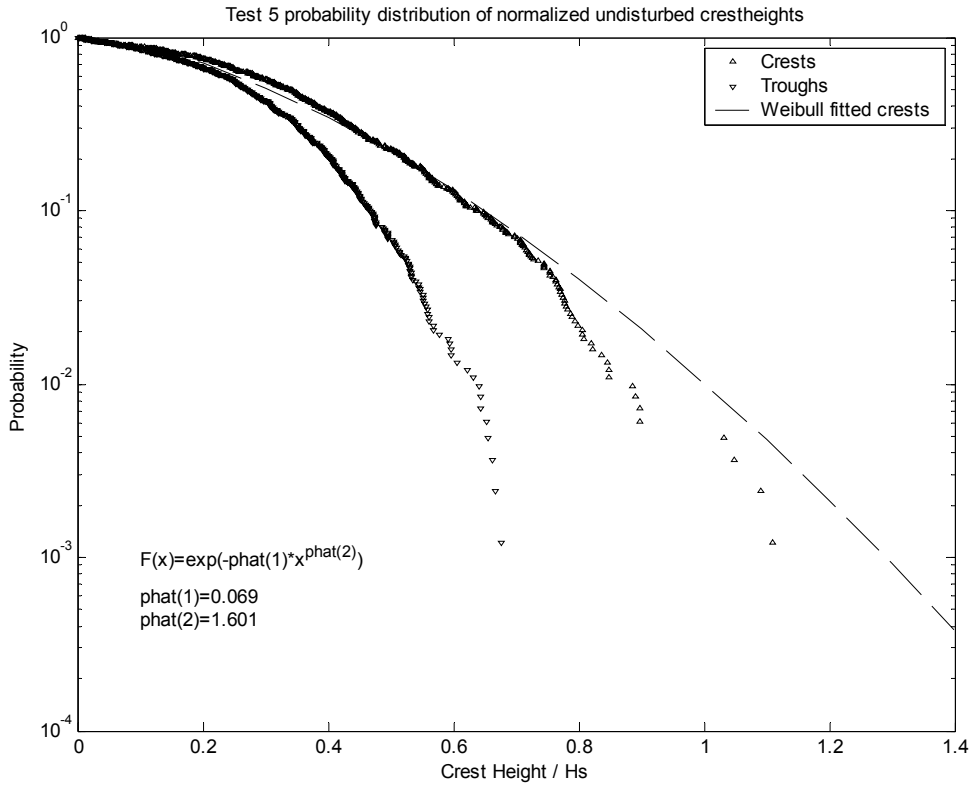

Figure 58: 10,000-year MDS Weibull fitted probabilities

For the 100-year unidirectional and 10,000-year multidirectional spectrum respectively, Figure 57 and Figure 58 indicate that the crest height is overestimated for the low probabilities. Figure 56 shows that the Weibull distribution fits the 100-year multidirectional sea-state very well. This is shown more clearly in the next three figures.

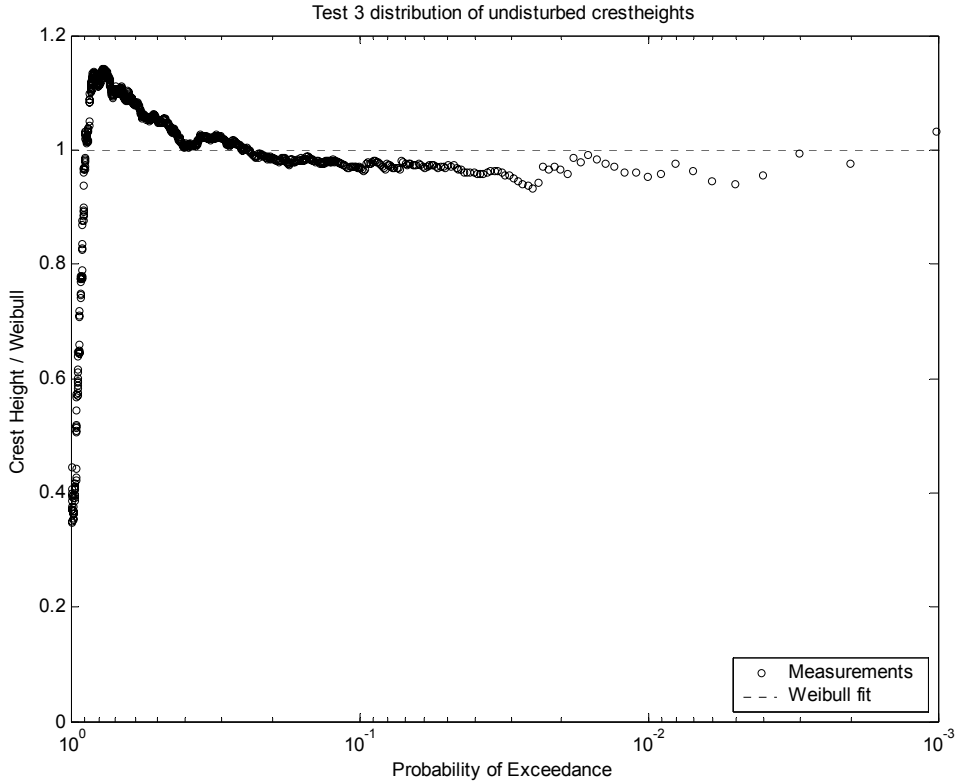

Figure 59: 100-year MDS measurements compared to Weibull

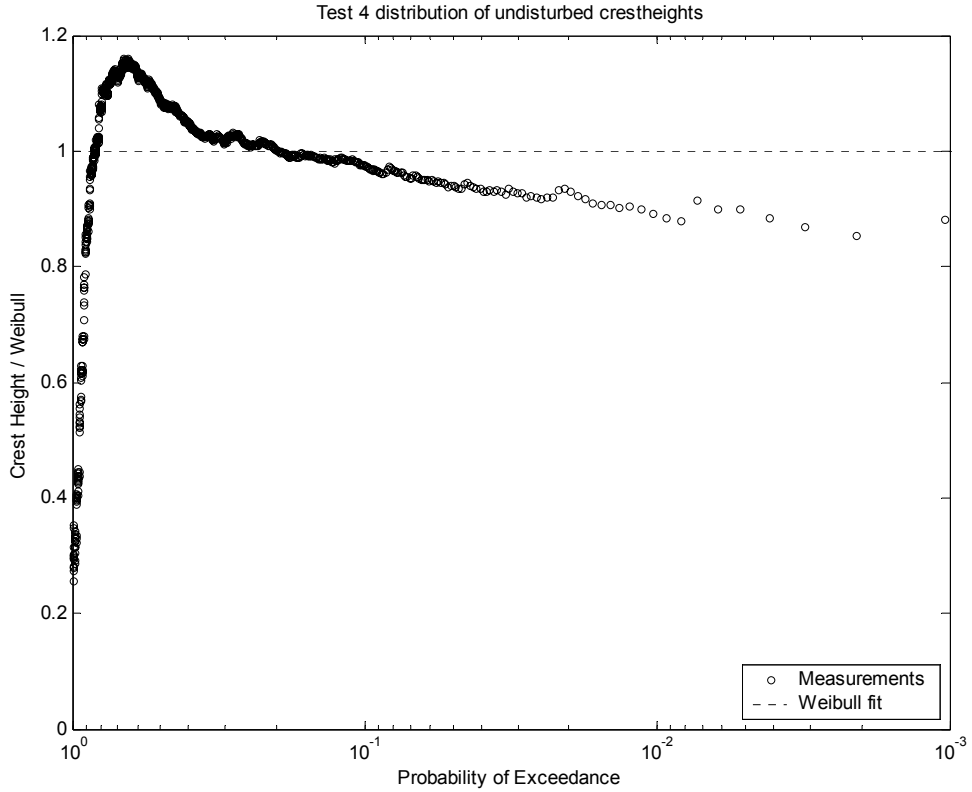

Figure 60: 100-year UDS measurements compared to Weibull

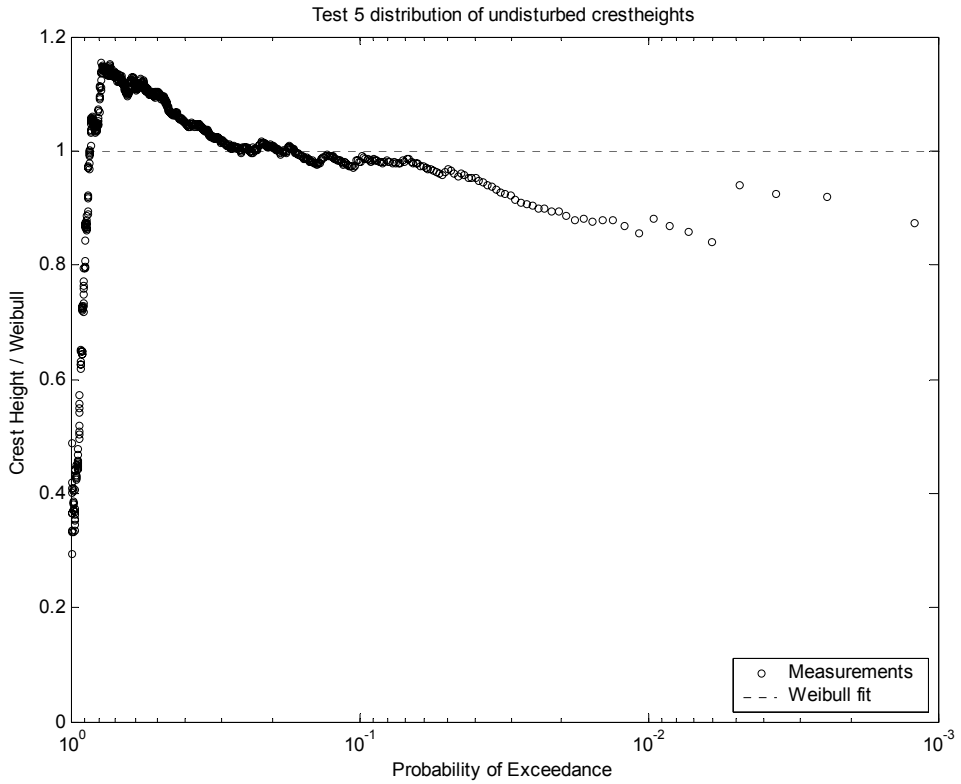

Figure 61: 10,000-year measurements compared to Weibull

In Figure 60 and Figure 61 the maximum crest heights are overestimated by the Weibull distribution by more than 10%. Another issue arises from Table 6, which shows both the 100-year and the 10,000-year sea-states have the same significant steepness. This leaves only the Ursell number, of which two values are available, to relate the Weibull parameters to. This does not result in a robust parameterisation. The second step of fitting as performed by Forristall [2], relating the Weibull parameters to the steepness and Ursell number, can therefore not be performed.

Analysis of the disturbed cases would provide a considerable amount of different values of the significant steepness. Determining the wavelength from the disturbed time series is a complicated matter however and this approach is not pursued here.

5.3. Surface elevation simulations to second order

Forristall [2] numerically implemented second order wave interaction calculations. A second-order expansion of the sea surface can capture the effects of wave steepness, water depth and directional spreading with no approximation other than the truncation of the expansion at second order. Higher-order interactions and other effects will of course influence the distribution of real wave crests. In particular, wave breaking could be important. The point of the investigation by Forristall [2] was, however, to see how well a straightforward application of second-order theory can match observations during heavy storms. In the present study, Forristall's simulation program is used to answer that same question for the measurements obtained during the Sakhalin II project model tests.

The simulation consists of a first-order approximation, which is adjusted to include two second-order effects:

1. Sharpening of the crest and flattening of the trough due to the positive second-order terms
2. Set-up or -down caused by passing wave-groups

The following figures provide insight in how well the simulation describes the model tests. They include the measurements and two plots of the second-order simulations; one including all the terms, referred to simply as simulation, and one that excludes the set-up and –down terms, referred to as simulation plus terms only. The reason for this is an important observation made by Forristall:

Multidirectional simulations including all the terms show a better fit to field measurements than to laboratory measurements.

A possible explanation for this could be that the long set-up and set-down waves, which are bound to the shorter free surface waves, are not absorbed properly by the wave absorbers in the wave basin. Once the free waves reach the end of the basin, the short waves are absorbed and the longer, bound waves are reflected into the basin to propagate as free waves and interact with the other free waves in the basin. The bound set-up or -down terms tend to lower the surface elevation under large wave groups. Due to the chaos of interacting long set-down waves, this phenomenon does not develop in the laboratory as it would in the field. The absence of the bound set-down terms results in higher crest elevation measurements than predicted by a second-order simulation including the minus terms. To account for this, the results from the simulations with only the plus terms are also plotted.

5.3.1. Undisturbed waves

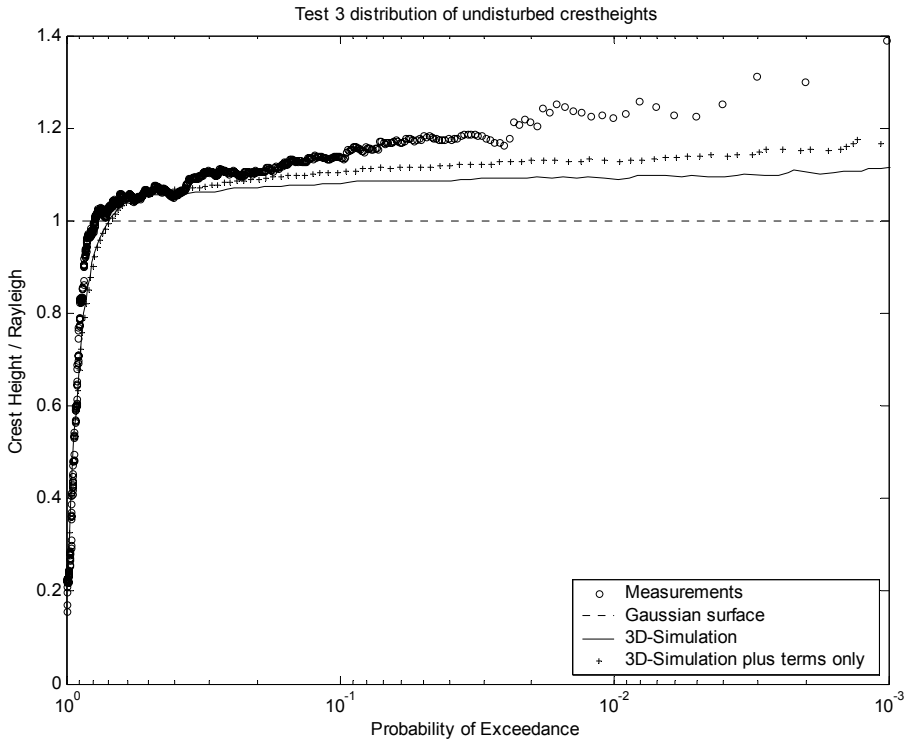

Figure 62: 100-year MDS measurements and simulation

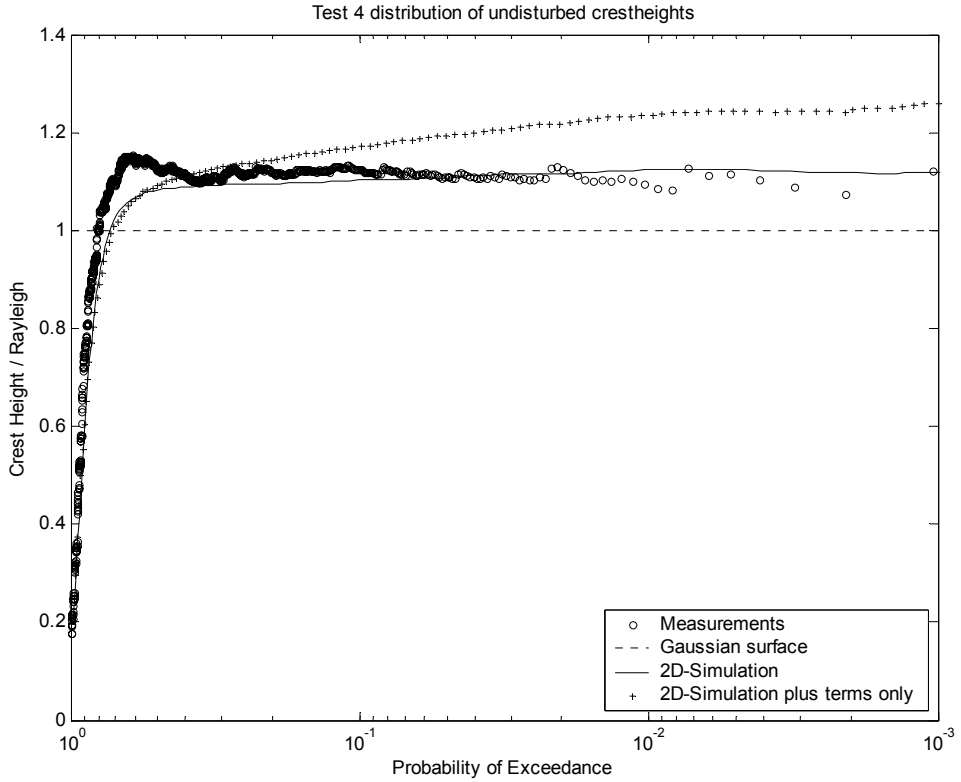

Figure 63: 100-year UDS measurements and simulation

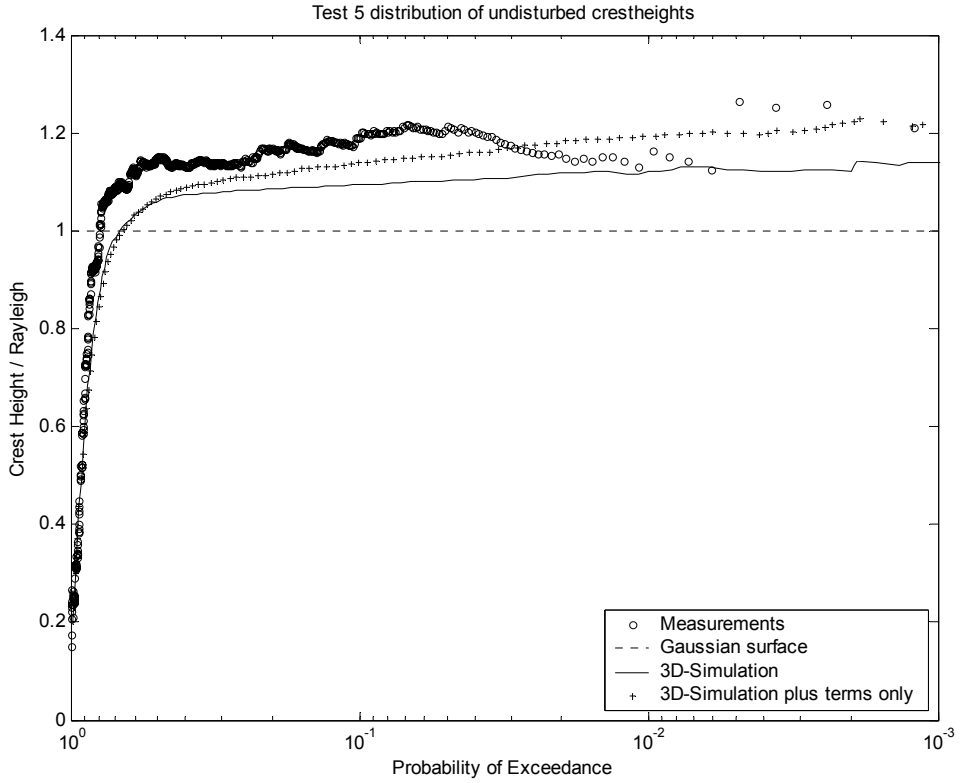

Figure 64: 10,000-year MDS measurements and simulation

Figure 63 shows that the match between simulation and the undisturbed measurements for the unidirectional test is better when the minus terms are included.

Figure 62 and Figure 64 show that for the multidirectional tests, the simulation including only the plus terms represents the best fit to the measurements. Figure 64 shows that for the measurements during the 10,000-year multidirectional sea-state the increase in normalized crest heights stops for low probabilities. A possible explanation for this phenomenon is that crest heights might be limited due to wave breaking.

5.3.2. Waves at the rear legs

The analysis is now continued for the surface elevation with the structure in place. As mentioned, the highest significant wave heights are measured at the two rear legs, probe R21 and R25, their variance density spectra are shown in Figure 39 and Figure 40 respectively. The fit between the undisturbed measurements and the second-order simulation including the minus terms, is very close for the 100-year unidirectional spectrum, test 4, as shown in Figure 63. The focus is therefore first on comparing the disturbed measurements and simulations at probe R21 and R25 for the unidirectional wave case. The occurrence of set-up and –down terms, as discussed in Section 5.3, is illustrated for these locations in Figure 65. The time-series are filtered to remove all energy above 0.04Hz, which is approximately the start of the low frequency flank of the spectrum. This analysis results in the set-up and –down and is shown as the red line. The set-up reaches values up to 2 meters or more. In addition, the mean water level is raised above the still water level due to waves interacting with the structure. The value of the mean water level at each probe location is stated in the legend. For the undisturbed tests these values are typically in the order of several centimetres.

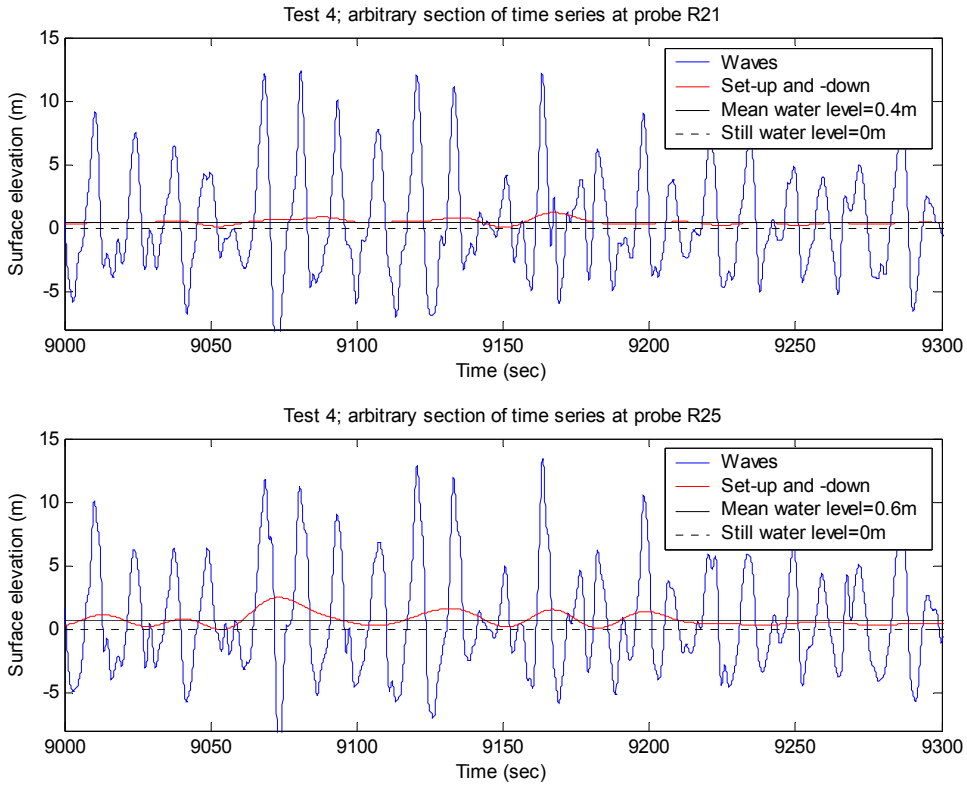

Figure 65: Set-up under passing wave for 100-year UDS

An additional low frequency set-up is observed during the wave group, opposite to what is expected from second-order theory. Nevertheless, we have shown that for the undisturbed unidirectional case the fit is best when the minus terms are included. To allow for comparison between the simulations and measurements the following adjustments are made:

- The minus-terms of the second-order simulations are not included as there is reason to assume that the laboratory measurements do not show these terms according to the theory.
- The increase in mean water level is deducted from the measurements as the simulations do not include this phenomenon.

This results in the following figures:

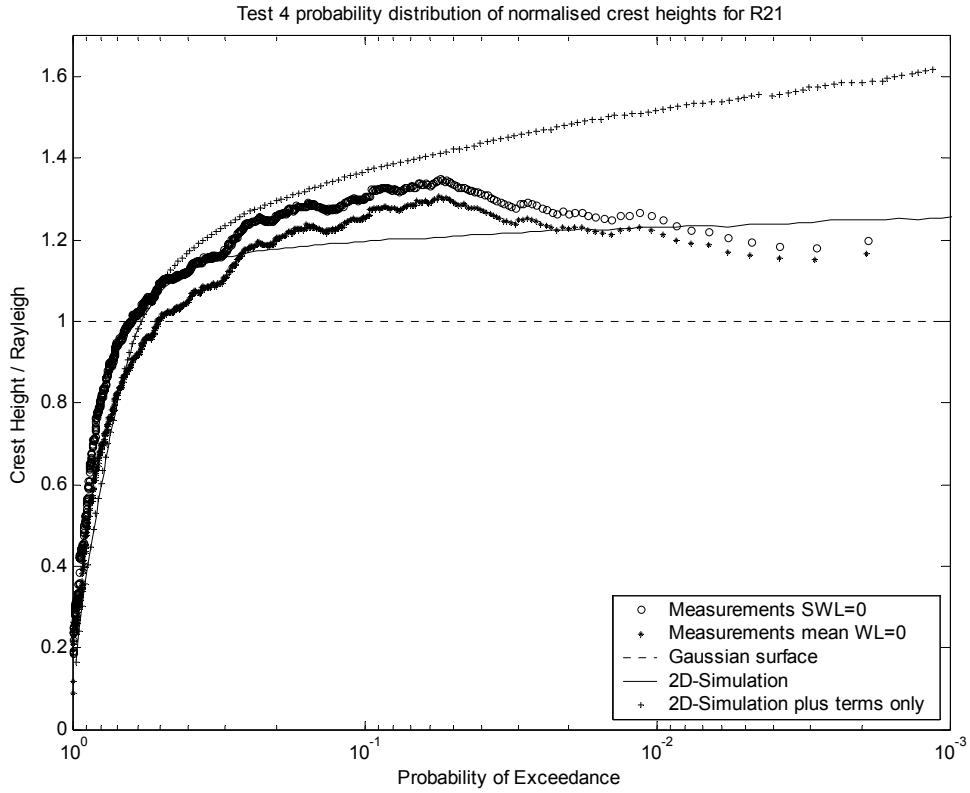

Figure 66: Measurements and simulations at R21 for 100-year UDS

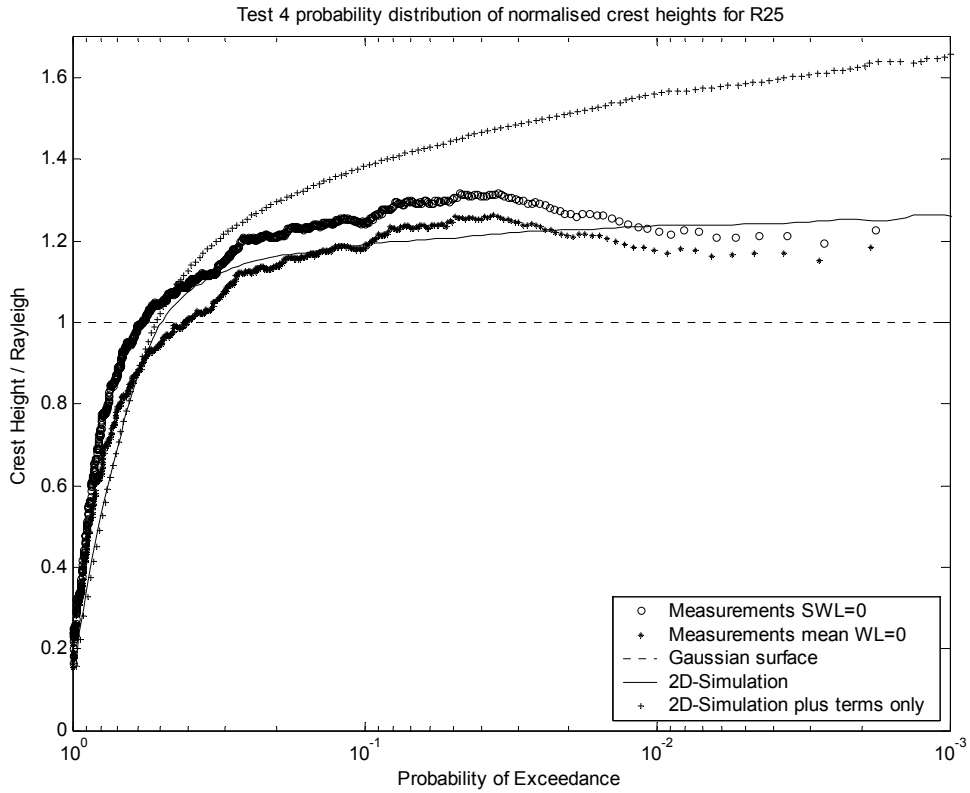

Figure 67: Measurements and simulations at R25 for 100-year UDS

Figure 66 and Figure 67 show the fit between the 100-year unidirectional measurements at the rear legs and the simulation to be close when the minus terms are included. This is consistent with the undisturbed tests.

For the multidirectional sea-state we first consider the 100-year case. Figure 68 shows the low frequency set-up during the wave group for the multidirectional 100-year sea-state. It reaches a maximum value of 3.2m at probe R21. Again this is opposite to what is expected from second-order theory.

The 10,000-year multidirectional sea-state time series including the set-up is shown in Figure 69.

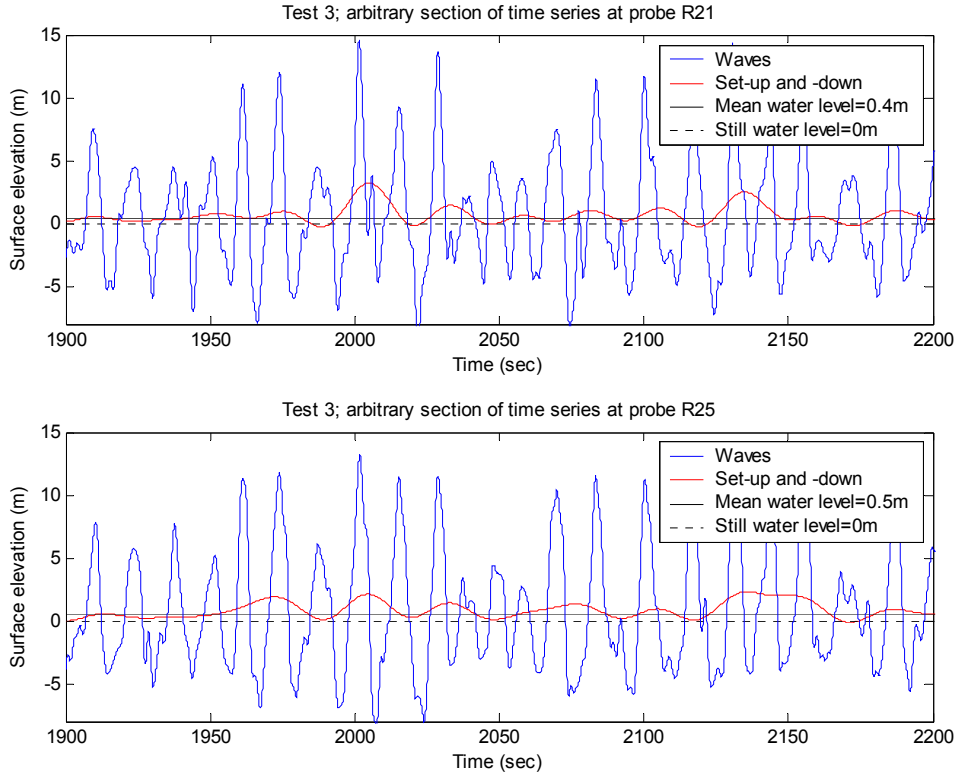

Figure 68: Set-up under passing wave for 100-year MDS

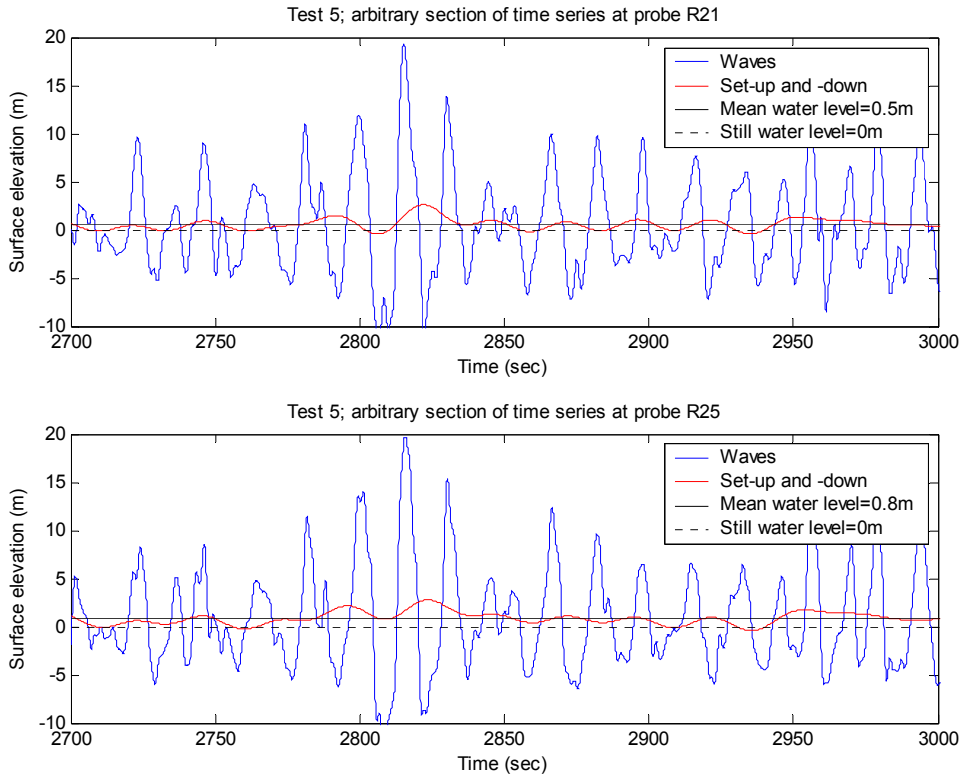

Figure 69: Set-up under passing wave for 10,000-year MDS

Figure 70 and Figure 71 show the fit between the simulation and the measurements at the rear legs during the 100-year multidirectional sea-state is close when the minus terms are omitted. This is consistent with the undisturbed tests.

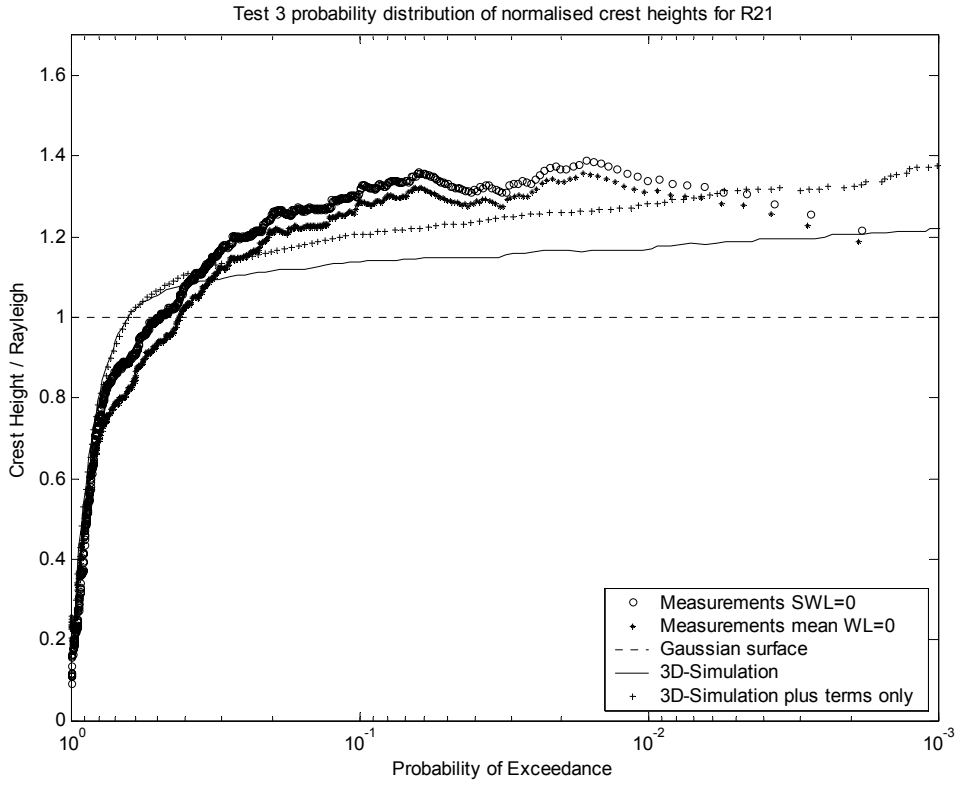

Figure 70: Measurements and simulations at R21 for 100-year MDS

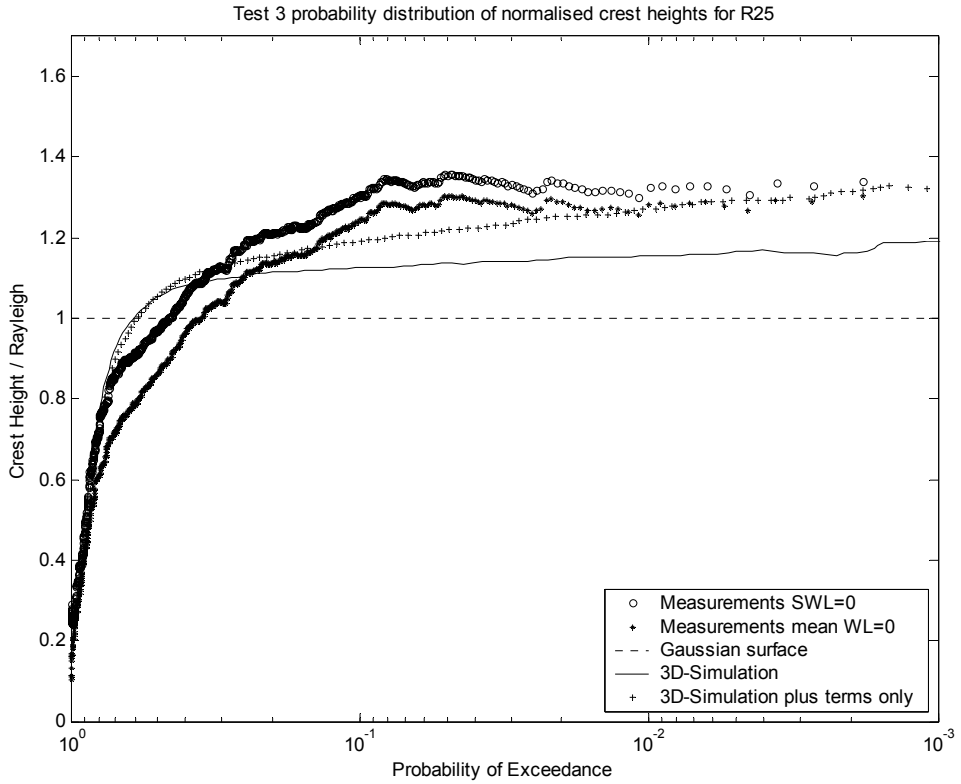

Figure 71: Measurements and simulations at R25 for 100-year MDS

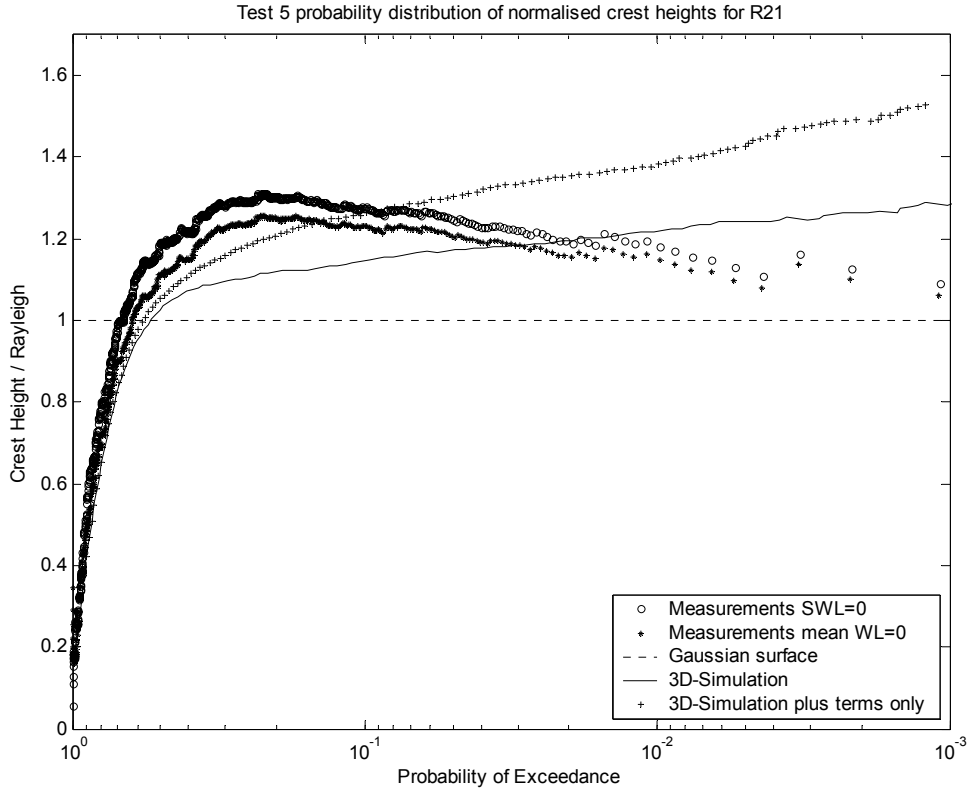

Figure 72: Measurements and simulations at R21 for 10,000-year MDS

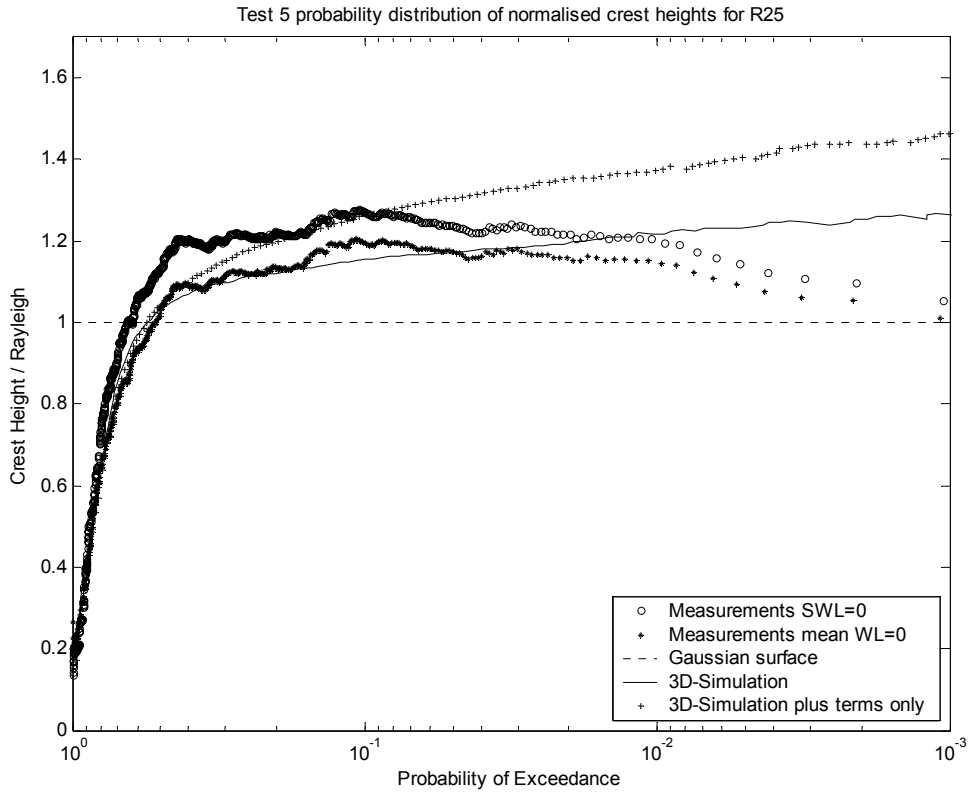

Figure 73: Measurements and simulations at R25 for 10,000-year MDS

Figure 72 and Figure 73 show the results for the 10,000-year multidirectional test. At relatively high probabilities, the trend of an increase in the normalised measured crest height with decreasing probability is bent downward to a decreasing normalised crest height. For the lower sea-states, a similar process starts at significantly lower probabilities. The measurements of the 10,000-year waves at the rear legs of the structure are not well described by the simulations. It is likely that the drop in normalised crest height measurements is due to breaking of the largest waves. This phenomenon is studied in Section 5.4.

5.4. Depth induced breaking

The breaking of waves has an important limiting influence on the crest height distribution. Neither the linear diffraction model DELFRAC, nor the second-order simulations take wave breaking into account. Video shots of the Sakhalin II project model tests showed waves were breaking along the centreline of the structure during at least some parts of the model tests. This supports the idea that wave breaking is a key reason the prediction recipe overestimates the crest heights at certain locations around the structure during certain model tests. Identifying the breaking phenomenon and quantifying the extent of breaking relative to certain parameters can greatly increase the applicability of the recipe developed within this study, therefore a first step is made to gain insight in the phenomenon as it occurs during different tests. First an overview of literature on the subject is presented.

In a paper on extreme waves and wave loading in shallow water Klopman and Stive [25] suggested two improvements as an alternative to what was at that time (1989) the more or

less standard derivation procedure for design wave heights in relatively shallow water. The improvements were based on observations of shallow water effects on both the decay of the total wave energy density and on the extreme waves in the wave height distribution. This first effect, the decay of total wave energy density due to depth limited breaking as a random wave field shoals towards shallower water, was accounted for by a dissipation model for random breaking waves as described by Battjes and Stive [26], and will not be addressed further in the present study. The second effect concerned the implications of shallow water effects on the wave height distribution of a random wave field as it propagates towards shallower depths. At the time there was a lack of reliable model formulations with respect to the distribution of extreme wave- and crest heights on shallow water. The extreme values were identified in the paper as being of great importance in the design of offshore structures. Klopman and Stive [25] stated that in relatively deep water it appeared that the wave heights of individual waves follow a Rayleigh distribution. Deviations due to non-linearity and finite bandwidth were relatively small compared to those deviations that might occur for extreme waves in the tail of the wave height distribution on relatively shallow water. These deviations in relatively shallow water were ascribed to the height or steepness limiting effects of a finite water depth. The Miche criterion for the maximum wave heights gives a smooth transition between the wave steepness limit in deep water and the maximum solitary wave height in shallow water. The practical upper boundary for the shallow water limit which is usually adopted is the theoretical maximum for a steady solitary wave on a horizontal bottom $H/d = 0.833$. The validity of this choice is amongst other things determined by the degree in which individual waves in a natural wave field in shallow water behave as steady solitary waves. In the limit for $d \to 0$ this is a realistic assumption, but it appeared from laboratory experiments that in the transition zone from nearly breaking to saturated breaking there was no proof of a more general validity of the limiting situation. The Miche criterion was adapted by Battjes and Janssen [27] to create a shallow water limit, which is different from 0.88:

$$\frac{H_{\max}}{d} = \frac{0.88}{kd}\tanh\left(\gamma\frac{kd}{0.88}\right) \qquad \{19\}$$

Comparison of laboratory measurements to equation {19} showed a relatively large data scatter and that even qualitatively the criterion did not seem to be a good approximation. It was concluded that apparently the relative water depth is not the dominant parameter in the physical process. Further analysis of the measurements showed that the dominant parameter was the ratio of total local energy density to depth, in the paper presented as: H_s/d. The extreme wave heights normalised by the water depth were plotted against this newly developed parameter and the data scatter was shown to be greatly reduced.

Klopman [28] proposed another parameterisation of the Weibull parameters in terms of wave height H_{rms} as supposed to the parameterisation developed by Klopman and Stive [25]. The new parameterisation gave a more conservative approximation.

An even more accurate predictive model for wave height distributions on shallow foreshores was developed by Battjes and Groenendijk [29]. A model distribution was proposed consisting of a Weibull distribution with exponent equal to 2 for the lower heights, and a Weibull distribution with a higher exponent for the higher wave heights.

There appears to be no literature on the subject of depth induced breaking at offshore structures in shallow water. Therefore we have compared the Sakhalin II project measurements to the literature on undisturbed wave breaking as presented above.

In the present study, the LUN-A structure has been tested for only two irregular sea-states at a constant undisturbed depth. Application of the improved Klopman methods as discussed above, which relate the steepness to the energy density normalised by the water depth, is therefore not considered to be a meaningful exercise. We are aware that the breaking criterion as defined in equation {19} has been developed for steady solitary waves on a gradually sloping shore and that even for that case it has been proven not to be a good approximation. Nevertheless, the criterion is used here for both the undisturbed and the disturbed model tests since it does at least allow for straightforward comparison of the various scatter plots. In these plots, the wave height normalised by the water depth is plotted against the wave number k, which is also normalised by the water depth. Firstly the undisturbed tests are shown in Figure 74. For the undisturbed tests, the calculation of the wave number k is straightforward and can be performed once the wave period and water depth are known. All the wave heights are well below the breaking criterion.

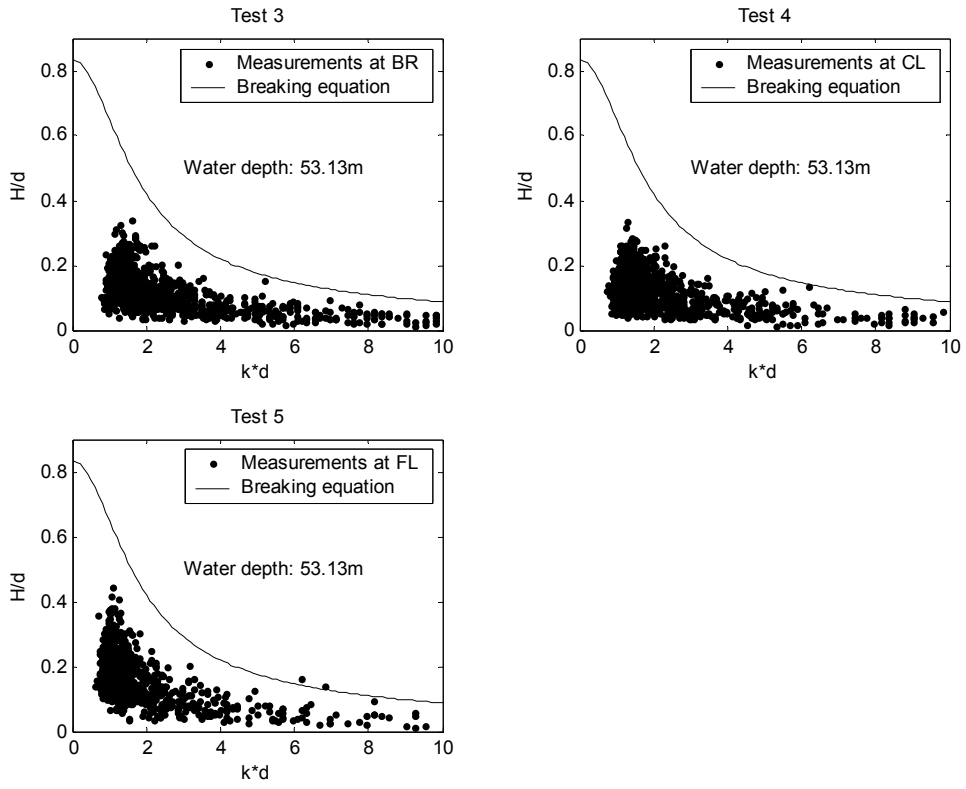

Figure 74: Undisturbed irregular wave tests

For the disturbed time series, the calculation of the wave number is by no means straightforward. The wave period can be obtained directly from the measurements, and can be used to calculate the deep water wavelength. Typically the undisturbed shallow water wavelength is in the order of several hundreds of meters. For a wave with a period equal to the peak period of the 100-year incident spectrum, the undisturbed shallow water wavelength is approximately 270m. As discussed in Section 4.1 the wave profile requires time to adjust to the sudden change in water depth; its wavelength does not change instantaneously as soon as the wave reaches the structure. In addition the legs influence the celerity of the waves. Cross-correlation analysis between measurements made at an up-wave and a down-wave probe along the centreline can provide the celerity of the crest and thereby the wavelength. The complicated modification of the waves by diffraction would

however make this exercise of questionable validity in determining the wavelength of the waves over the structure. Because of the ambiguity in the wavelength, we tried three different options for specifying it. Figure 75 shows the wave heights compared to the breaking curve at the centre of the structure, at probe R11. Firstly the plot is made as if the water depth is still the undisturbed water depth of 53m. Secondly the disturbed water depth of 38m is used to normalise and to calculate the wave number as if the waves were at this water depth travelling over a gradual slope. Thirdly the wave number is calculated as if the water depth was still the undisturbed water depth of 53m but the water depth used to normalise is the disturbed water depth of 38m.

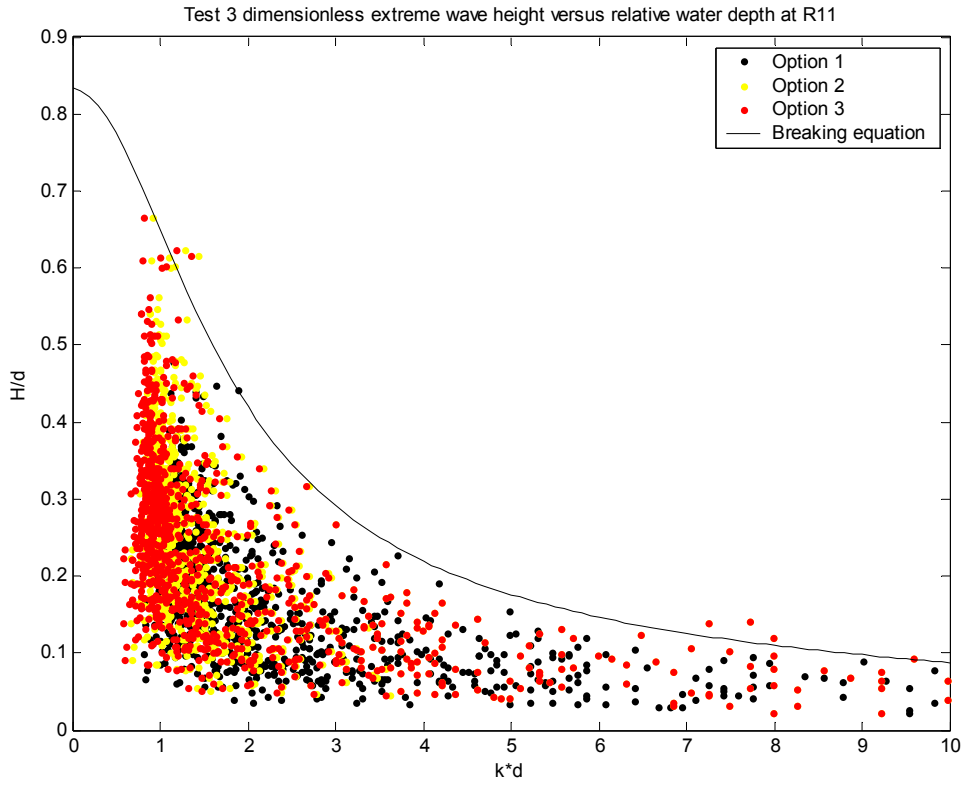

Figure 75: Water depth options 100-year sea-state at R11

Figure 75 shows that the influence of the water depth used for normalisation is very large. Option 1 uses 53m and is significantly different than options 2 and 3, which use 38m. The water depth used to calculate the wave number is of less influence as can be concluded from the relatively small difference between option 2 and 3. It appears that for waves with similar periods, and therefore deep water wavelengths, the reduction in wavelength is not much different for the two water depths. Figure 75 is consistent with linear theory that states the difference is larger for low wave numbers, or long periods. The same procedure is followed for the 10,000-year sea-state at probe R11 in Figure 76.

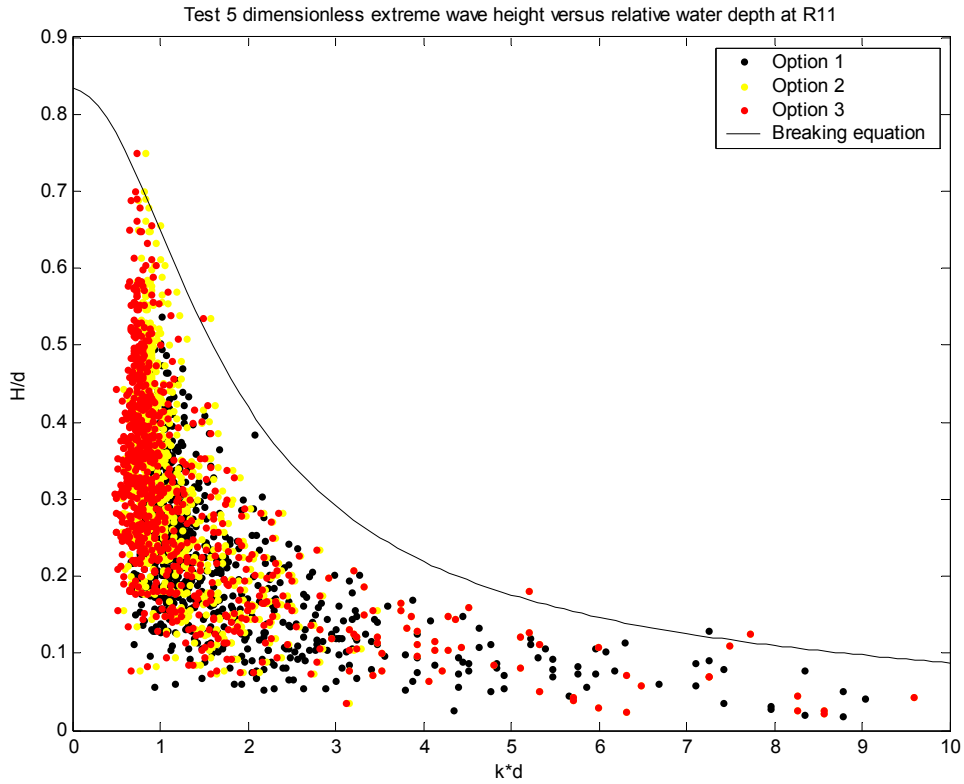

Figure 76: Water depth options 10,000-year sea-state at R11

Figure 76 shows that also for the 10,000-year sea-state there are approximately no cases of wave steepness exceeding the breaking equation. The same procedure is followed for both sea-states at the rear legs at probe R21 and R25.

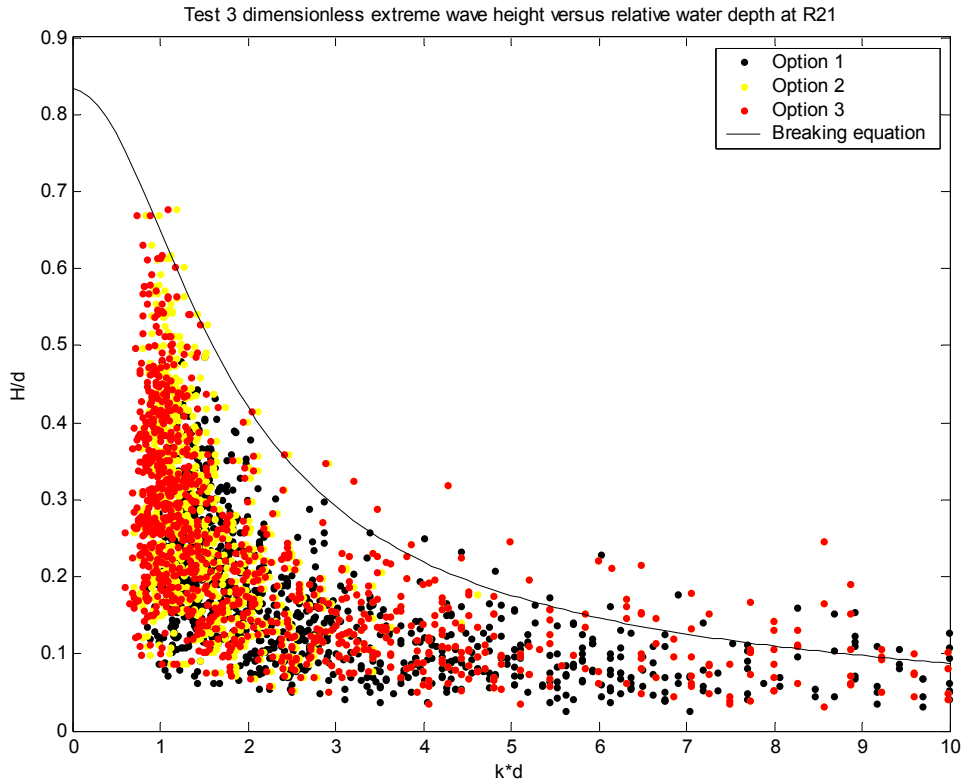

Figure 77: Water depth options 100-year sea-state at R21

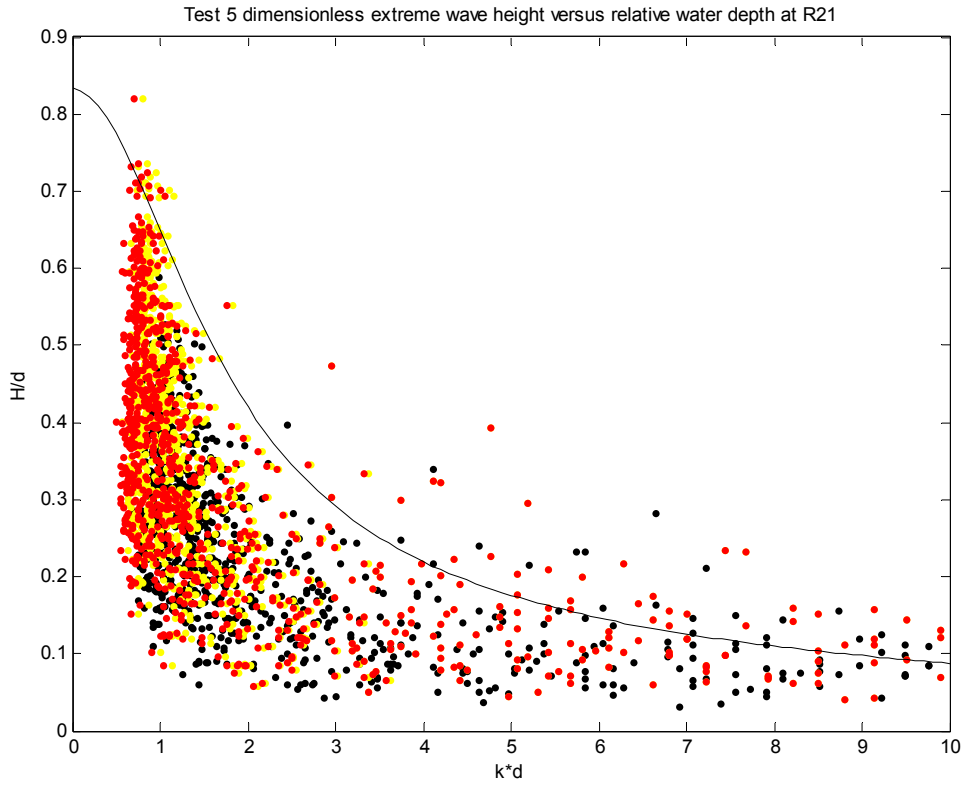

Figure 78: Water depth options 10,000-year sea-state at R21

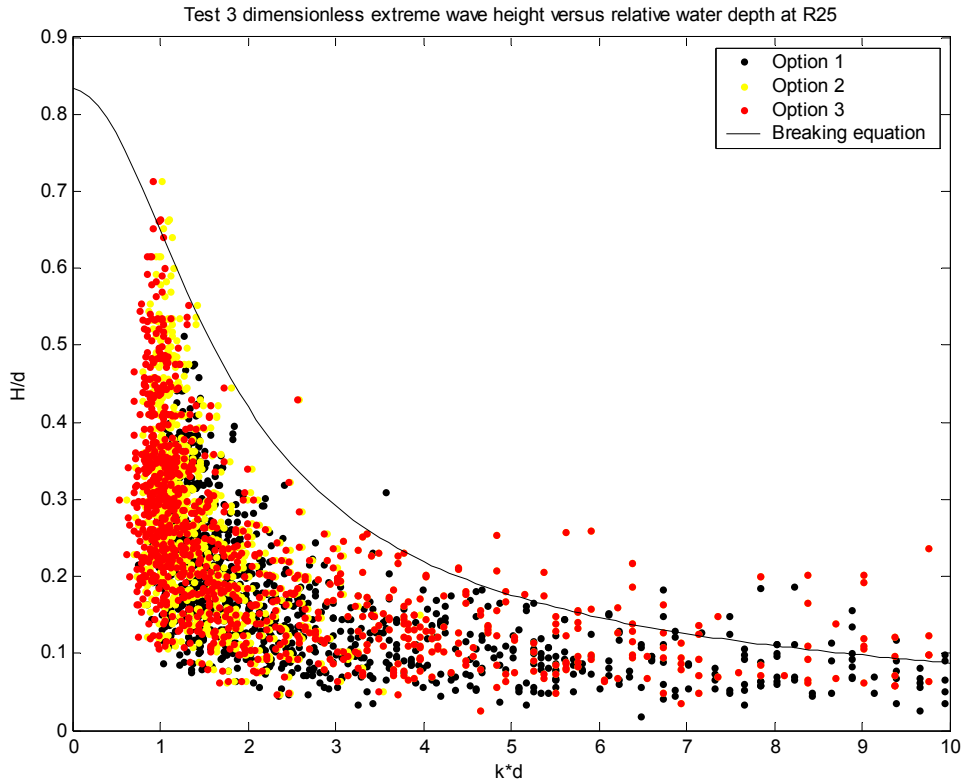

Figure 79: Water depth options 100-year sea-state at R25

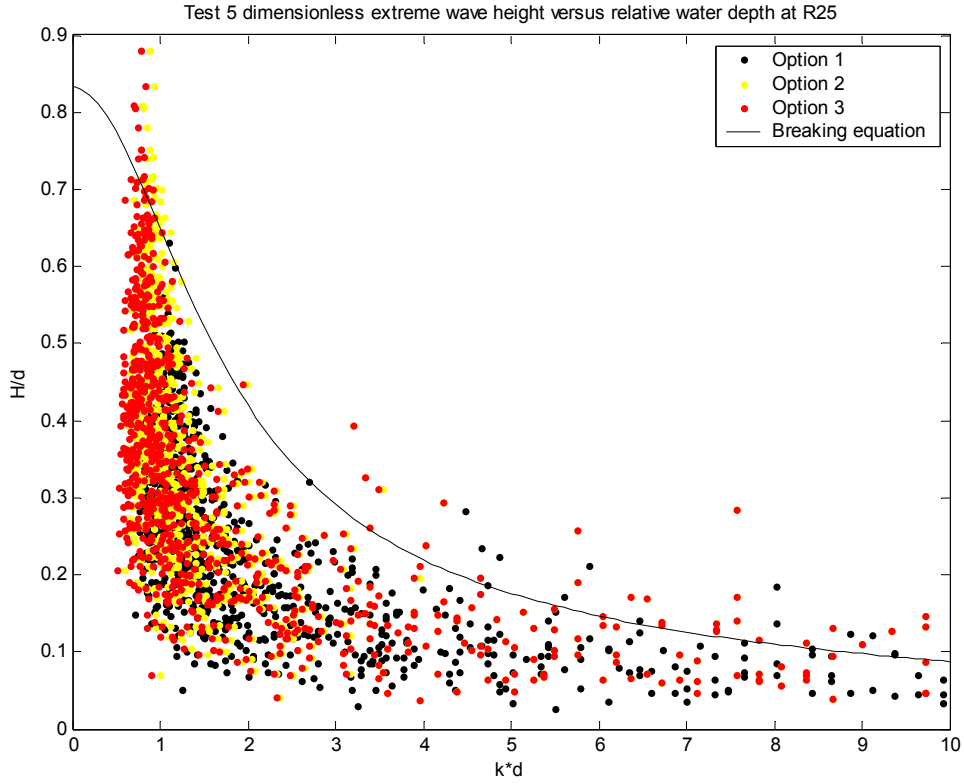

Figure 80: Water depth options 10,000-year sea-state at R25

The results at the rear legs indicate the waves are not obeying the breaking criterion as defined in equation {19}. We therefore study the applicability of the model developed by Battjes and Groenendijk [29] for wave height distributions on shallow foreshores. As mentioned previously, it consists of a Weibull distribution with exponent equal to 2 for the lower heights, and a higher exponent for the higher wave heights. The wave height at which the exponent is changed is called the transitional wave height. The model has a step-wise approach:

1. Calculate the transitional wave height: $H_{tr} = (0.35 + 5.8\tan(\alpha))d$, where α is the slope of the foreshore and d is the local water depth.
2. Calculate the root-mean-square wave height: $H_{rms} = (2.69 + 3.24\sqrt{m_0}/d)\sqrt{m_0}$
3. Calculate the dimensionless transitional wave height by dividing the result from step 1 by that from step 2
4. A table provided by Battjes and Groenendijk [29] gives the dimensionless wave height at certain probabilities.
5. The actual wave height at a certain probability can be obtained by multiplying the result from step 4 by that from step 2

This exercise is performed for probes R11, R21 and R25. The 0^{th} moment is obtained from the measurements, and to be able to get meaningful results we take α equal to zero. The calculations are performed for each multidirectional irregular wave test at a water depth of 38m and 53m. The variation of water depth is again because of the ambiguity in the wavelength.

This analysis yields a total of four wave height measurements per probe location that can be used to determine the applicability of the model.

Table 11: Depth limited wave heights at probe R11

R11	Water depth 53m		Water depth 38m	
	Test 3	**Test5**	**Test 3**	**Test5**
$H_{0.1\%}$ predicted	17.6m	24.6m	18.2m	26.5m
$H_{0.1\%}$ measured	25.4m	28.6m	25.4m	28.6m
$H_{1\%}$ predicted	15.7m	22.0m	16.3m	23.7m
$H_{1\%}$ measured	20.7m	24.7m	20.7m	24.7m

Table 12: Depth limited wave heights at probe R21

R21	Water depth 53m		Water depth 38m	
	Test 3	**Test5**	**Test 3**	**Test5**
$H_{0.1\%}$ predicted	19.0m	26.2m	19.8m	29.0m
$H_{0.1\%}$ measured	25.8m	31.3m	25.8m	31.3m
$H_{1\%}$ predicted	17.0m	23.4m	17.7m	25.9m
$H_{1\%}$ measured	22.6m	26.7m	22.6m	26.7m

Table 13: Depth limited wave heights at probe R25

R25	Water depth 53m		Water depth 38m	
	Test 3	**Test5**	**Test 3**	**Test5**
$H_{0.1\%}$ predicted	19.8m	28.0m	20.6m	30.7m
$H_{0.1\%}$ measured	27.2m	33.5m	27.2m	33.5m
$H_{1\%}$ predicted	17.7m	25.0m	18.4m	27.6m
$H_{1\%}$ measured	22.6m	27.2m	22.6m	27.2m

Table 11, Table 12, and Table 13 show the model developed by Battjes en Groenendijk [29] cannot be used in its present form to predict the amplified wave height at the structure. The method gives better results if the actual water depth above the caisson is used, which is 38m. The accuracy of the model is acceptable for one of the four wave heights only. The 1:100 wave height during test 5, which is the 10.000-year multi-directional sea-state, is predicted reasonably accurately at all the probe locations analysed. All the other wave heights are significantly under predicted. No explanation for the difference in agreement is available.

6. THE PREDICTION RECIPE

The prediction recipe, as developed using the LUN-A model during the 100-year multidirectional sea-state, works as follows:

1. Load the geometry of the CGS in DELFRAC. Calculate the diffracted spectra at various location underneath the deck of the structure. Choose the location with the highest value for the significant wave height $H_{m0.}$
2. Run the second-order simulation program using the spectrum predicted by DELFRAC at the location with the highest significant wave height as input.

This recipe is demonstrated for the LUN-A structure at probe R25 during the 100-year multidirectional sea-state. Figure 81 shows the first step in the prediction recipe: Predicting the diffracted spectrum at the location with the highest value for the significant wave height.

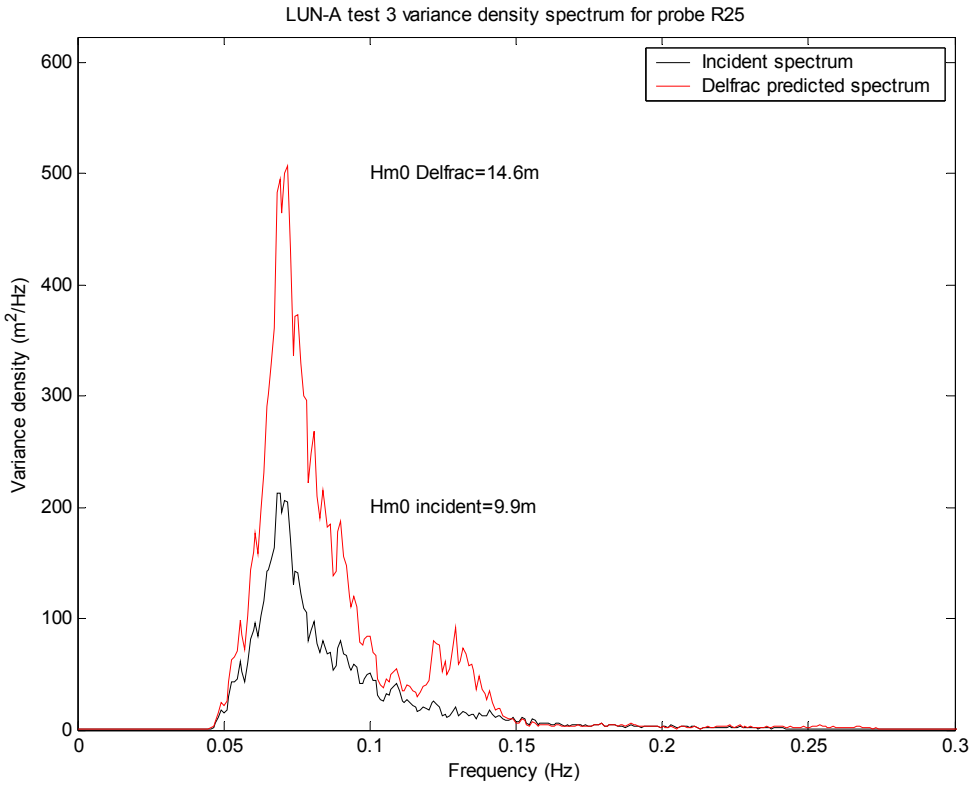

Figure 81: Step 1: Predict diffracted spectrum using DELFRAC

The next step is to translate this diffracted spectrum into an extreme crest height. As discussed in Section 5.3, the second-order simulation including all the terms shows a better fit to field data than to laboratory data for a multidirectional spectrum. For multi-directional laboratory data the fit between simulation and measurements is better when the minus terms are omitted from the second-order simulation.

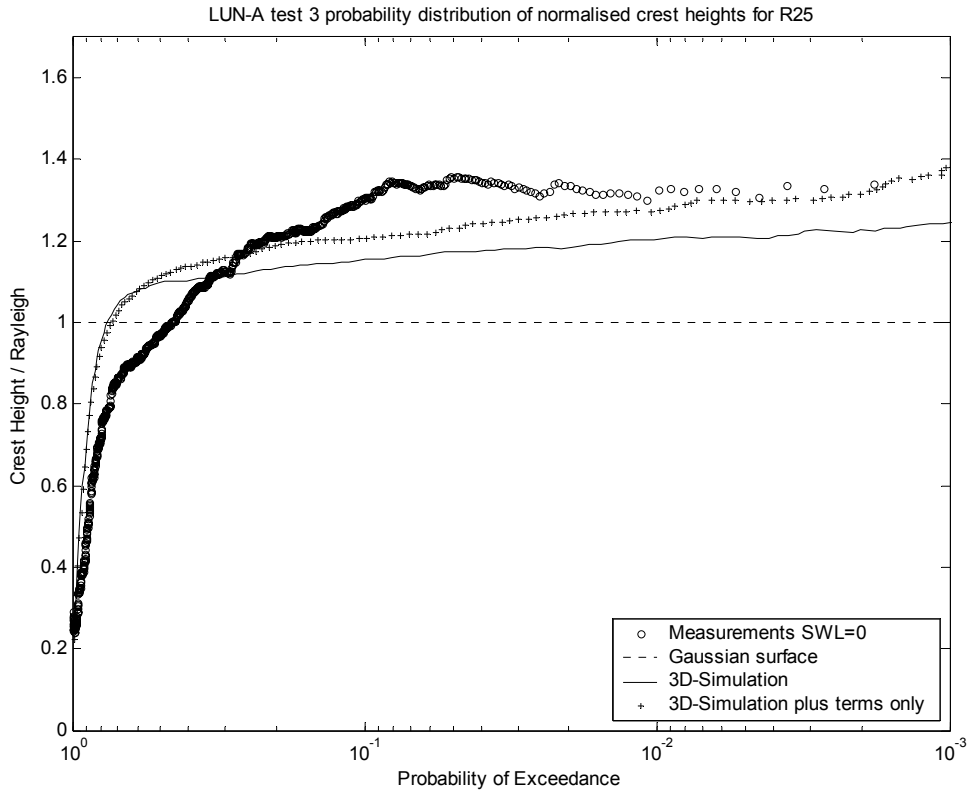

Figure 82: Step 2: Predict the 1:1000 crest height from the spectrum

Figure 82 shows the second step in the prediction recipe: Predicting the 1:1000 crest height from the diffracted spectrum at the location with the highest significant wave height. The figure shows the agreement between the measured normalised crest height and the prediction recipe is close for low probabilities.

We conclude the prediction recipe is accurate in predicting the extreme crest height underneath the deck during a one-in-a-hundred-year storm at the LUN-A structure. To assess the general applicability we now validate the recipe using the measurements obtained for the PA-B model.

6.1. Validation of the recipe using the PA-B model

To validate the applicability of DELFRAC in determining the diffracted spectra at an arbitrary CGS, we perform a similar exercise as in Section 4.2.2 but now for the PA-B structure. The amplification factors, as defined in equation {12} and equation {13}, are plotted along the centreline. Figure 83 shows the fit between DELFRAC and the measurements is much better for the LUN-A than for the PA-B structure. Although DELFRAC consistently over predicts the amplification factor for the PA-B structure, the global trend along the centreline is reproduced quite well.

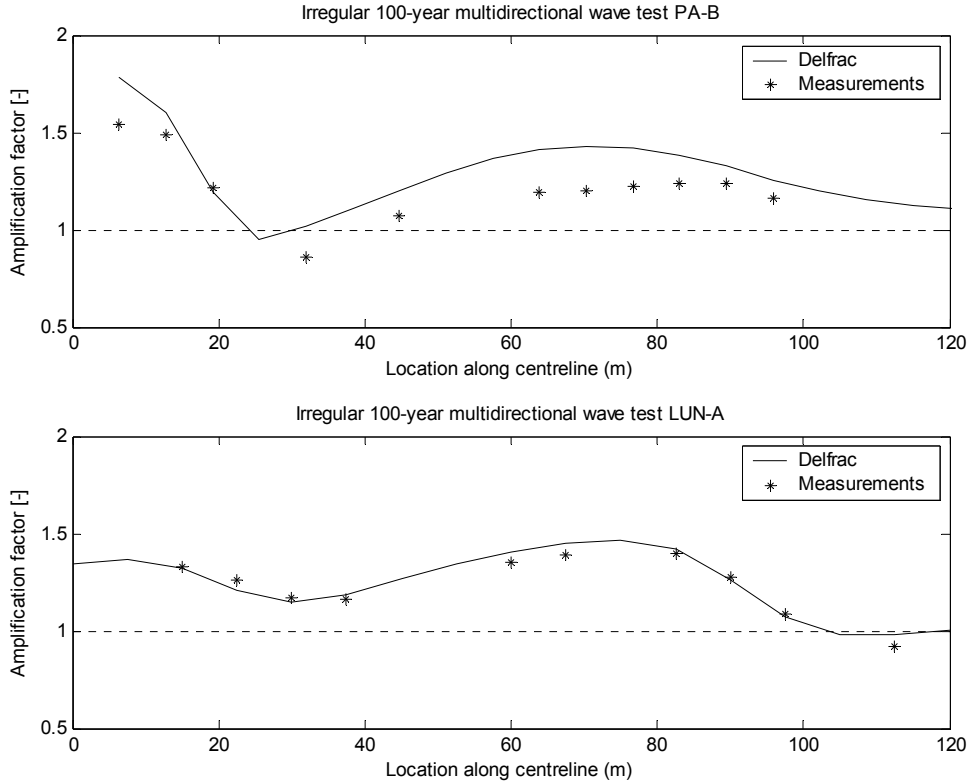

Figure 83: DELFRAC fit to measurements for PA-B and LUN-A

For the PA-B structure, the maximum value of the measured significant wave height occurs in front of the right up-wave column, at probe location R1. The difference in geometry between the two structures, as discussed in Section 1.3.2 and Section 1.3.3, results in a different diffraction process and therefore a different location for the maximum value of the significant wave height. Comparison of Figure 4 and Figure 5 shows the spacing between the up-wave columns of the PA-B structure is significantly smaller than for the LUN-A structure. This close spacing is likely to cause the location of the maximum significant wave height at the PA-B structure to be in front of the up-wave columns. The measured variance density spectrum at the right up-wave column is compared to the DELFRAC predicted spectrum in Figure 84. DELFRAC significantly overestimates the energy in the spectrum.

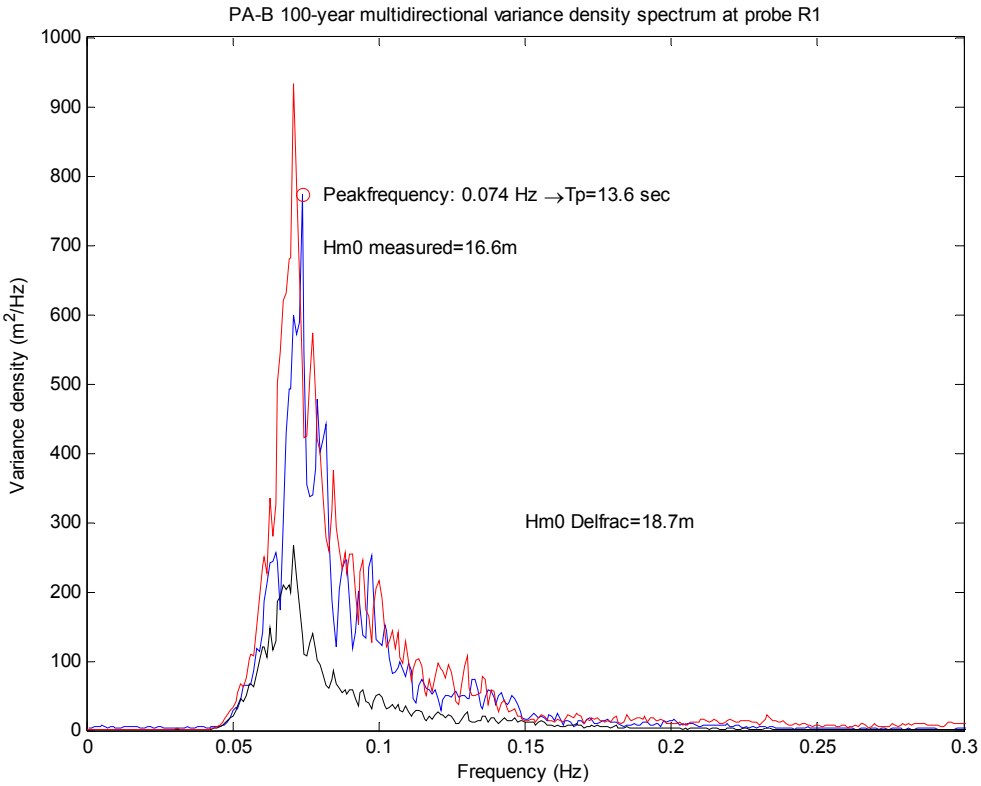

Figure 84: Predict diffracted spectrum at PA-B using DELFRAC

Figure 84 shows for the location with the highest significant wave height that while the shape of the energy density spectrum is accurately reproduced, the total amount of energy is significantly overestimated by DELFRAC. Running the second-order simulation with the DELFRAC spectrum instead of the measured spectrum will therefore result in a significant overestimation of the highest crest height. We therefore run the simulation with the measured spectrum. The results from this simulation are shown in Figure 85. Even when the measured spectrum is used as an input for the second-order simulation, it significantly overestimates the highest crest height.

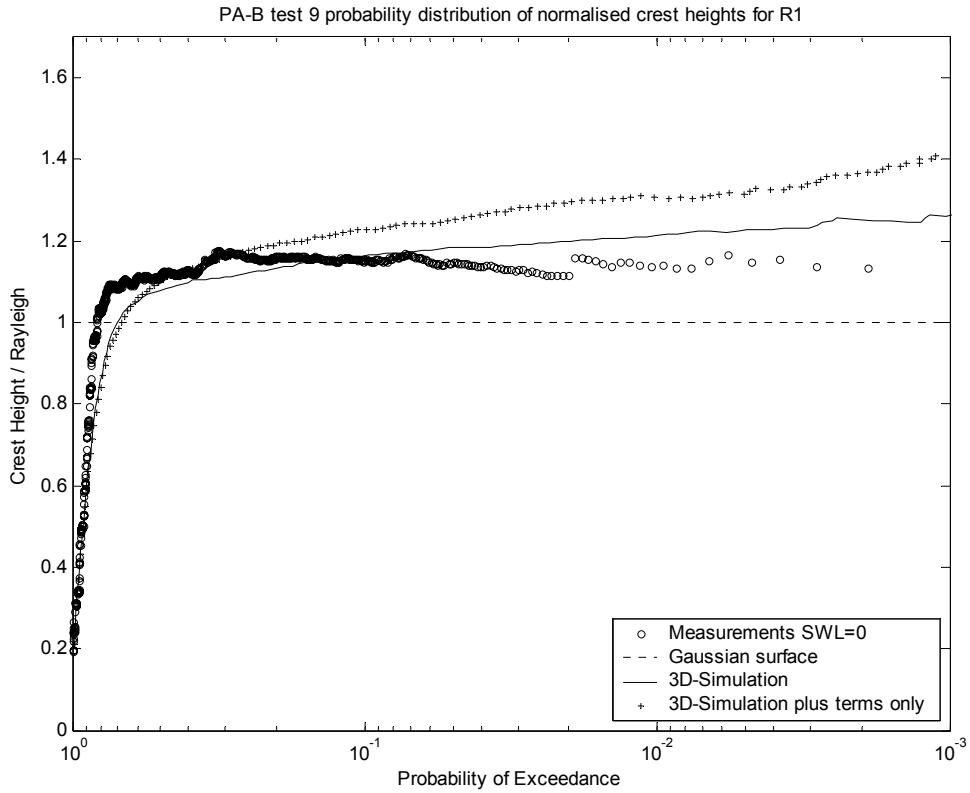

Figure 85: Predict the 1:1000 crest height at PA-B from the spectrum

The prediction recipe is not accurate in predicting the extreme crest height underneath the deck during a one-in-a-hundred-year storm at the PA-B structure.

7. CONCLUSIONS AND RECOMMENDATIONS

The main conclusions can be summarized as follows:

1. DELFRAC gives a close fit to the measurements made during the Malampaya model test [4] of regular waves focussing over the underwater box-shaped storage caisson.
2. DELFRAC accurately predicts the first-order free surface response for the two regular wave cases interacting with the complete LUN-A structure during the Sakhalin II project model test [6].
3. DELFRAC effectively simulates the shape of the measured diffracted multidirectional irregular wave spectra for both the Sakhalin II project structures.
4. For the 100-year sea-state at the LUN-A structure, DELFRAC gives an excellent prediction of the diffracted spectrum at various locations around the structure, including the peak at twice the incident peak frequency.
5. The results found for the LUN-A structure in the present study are consistent with results found in similar studies by Ohl et al. [3] and [5], on less complex structures.
6. For the PA-B model the 100-year DELFRAC predictions are too high compared to the measurements obtained during the Sakhalin II project model test [6] .
7. A complete second-order expansion of the sea surface accurately predicts the extreme crest height for the model test of the undisturbed unidirectional 100-year irregular sea-state at the proposed location for the LUN-A structure.
8. Measurements made during undisturbed multidirectional irregular model tests give higher values for the crest height than is expected from second-order theory.
9. A complete second-order expansion of the sea surface accurately predicts the extreme crest height, measured at the significant location underneath the deck of the LUN-A structure during the model test of the unidirectional 100-year irregular sea-state.
10. A second-order expansion of the sea surface excluding the set-down terms accurately predicts the extreme crest height, measured at the significant location underneath the deck of the LUN-A structure during the model test of the multidirectional 100-year irregular sea-state.
11. Depth induced breaking is an important phenomenon limiting the crest heights.

The accuracy of linear diffraction theory in predicting the diffracted spectra at a complex structure like LUN-A during a multi-directional irregular sea-state is very promising. The second-order expansion has shown that for the 100-year irregular sea-state it is accurate in predicting the extreme crest height at the LUN-A structure using the DELFRAC calculated spectrum as input. Therefore for this specific structure during this specific sea-state the prediction recipe developed within the present study can provide the same information with respect to the extreme crest height, with the same accuracy as physical model tests. During the 10,000-year sea-state at the LUN-A structure, and the 100- and 10,000-year sea-state at the PA-B structure, wave breaking is observed to a great extent. In addition to the analysis performed in the present study, videos showing this breaking process are available. They were made by CHC during the Sakhalin II project model tests. Both of the numerical codes in the prediction recipe do not take the effect of wave breaking into account. As soon as this becomes an important phenomenon, linear diffraction theory is no longer accurate in predicting the total energy in the diffracted spectrum. In addition the extreme

crest height distribution is no longer accurately described by the second-order simulation. This significantly limits the applicability of the recipe in its present form to situations where breaking is not an important phenomenon. We therefore suggest the following additional work to be carried out:

1. During the time of this research data has been obtained by CHC on multidirectional irregular wave tests on a slightly adjusted PA-B structure for significantly lower sea-states than the 100-year condition that was available for the present study. The extent of wave breaking in these tests is expected to be much lower. Therefore, we suggest this data be used to validate the applicability of the recipe on a different structure under similar conditions.
2. DELFRAC gives good results for the multi-directional 100-year sea-state without taking this directional spread into account. We therefore suggest a thorough comparison between the diffraction process during the unidirectional and the multi-directional sea-states.
3. A study on depth induced breaking at offshore structures in shallow water can fill the present gap with respect to knowledge concerning this phenomenon. This study could provide results that will greatly enhance the applicability of the prediction recipe. The development of a breaking criterion allows one to determine up front whether or not breaking will be an important phenomenon at a certain structure during a certain sea-state and therefore whether or not the prediction recipe can be used. Another application of the breaking criterion could be that the recipe is used to determine the extreme crest height, regardless of the expected extent of wave breaking. The criterion can than be used to cut off, if necessary, the crest height distribution and suggest an alternate crest height. This requires a far more advanced breaking criterion.
4. Compare the results from higher-order diffraction codes to those obtained using DELFRAC and to the measurements. This would give a clear indication whether the use of higher-order codes significantly contributes to the accuracy of the determination of the extreme crest height at a CGS.

REFERENCES

[1] Emery & Thomson, Data analysis methods in physical oceanography, 2nd and revised edition

[2] Forristall, G.Z., Wave crest distributions: Observations and second-order theory. Journal of Physical Oceanography, vol 30, pp 1931-1943

[3] Ohl C.O.G., Eatock Taylor R., Taylor P.H. and Borthwick A.G.L., Water wave diffraction by a cylinder array. Part 1. Regular waves. Journal of Fluid Mechanics (2001), vol. 442, pp. 1-32

[4] C. Swan & Associates Ltd., Wave-Structure Interaction at the proposed Malampaya CGS. Final Report July 1998

[5] Ohl C.O.G., Taylor P.H., Eatock Taylor R. and Borthwick A.G.L., Water wave diffraction by a cylinder array. Part 2. Irregular waves. Journal of Fluid Mechanics (2001), vol. 442, pp. 33-66

[6] Cornet A., Morin V., Durand N., Model tests to select deck elevations for the PA-B and LUN-A platforms. Canadian Hydraulics Centre controlled technical report HYD-CTR-008, August 2002

[7] Dmitrieva I., DELFRAC 3-D potential theory including wave diffraction and drift forces acting on the structures. TU-Delft Report No. 1017, December 1994

[8] Belibassakis K.A., Athanassoulis G.A., Extension of second-order Stokes theory to variable bathymetry. Journal of Fluid Mechanics. (2002), vol. 464, pp.35-80

[9] Mei C.C., Black J.J., Scattering of surface waves by rectangular obstacles in waters of finite depth. Journal of Fluid Mechanics (1969), vol. 38, part3, pp. 499-511

[10] Mei C.C., The applied dynamics of ocean surface waves

[11] Dingemans M.W., Water wave propagation over uneven bottoms. Part 1-Linear wave propagation. Advanced series on ocean engineering – Volume 13

[12] Swan C., Taylor P.H., van Langen H., Observations of wave-structure interaction for a multi-legged concrete platform. Applied Ocean Research 19 (1997) 309-327

[13] Niedzwecki J.M., Huston J.R., Wave interaction with tension leg platforms. Ocean Engineering (1992), Vol. 19, No 1, pp. 21-39

[14] Sweetman B., Winterstein S.R., Cornell C.A., Air gap analysis of floating structures: first- and second-order transfer functions from system identification. Applied Ocean Research 24 (2002) 107-118

[15] Linton C.M., Evans D.V., The interaction of waves with arrays of vertical circular cylinders. Journal of Fluid Mechanics (1990), vol. 215, pp. 549-569

[16] Niedzwecki J.M., Duggal A.S., Wave run-up and forces on cylinders in regular and random waves. Journal of Waterway, Port, Coastal and Ocean Engineering, Vol. 118, No. 6, Novemner/December, 1992

[17] Kriebel D.L., Non-linear run-up of random waves on a large cylinder, 1993 OMAE - Volume I, Offshore Technology ASME 1993

[18] Kriebel D.L., Non-linear wave run-up on large circular cylinders.1992b Proceedings Civil Engineering in the Oceans, ASCE, pp. 173-187

[19] Kriebel D.L., Non-linear wave interaction with a vertical circular cylinder. Part II: Wave run-up, Ocean Engineering, Vol. 19, No. 1, pp. 75-99, 1992

[20] Martin A.J., Easson W.J., Bruce T., Run-up on columns in steep-deep water regular waves, Journal of waterway, port, coastal and ocean engineering, January/February 2001

[21] WAMIT; a 2nd order diffraction program, www.wamit.com

[22] Holthuijsen L.H., Battjes J.A., Wind waves. Draft version of TU-Delft lecture notes, October 2001

[23] Tucker M.J., Pitt E.G., Waves in ocean engineering. Elsevier ocean engineering book series volume 5, 2001

[24] Battjes, J.A., Korte golven. TU-Delft lecture notes, September 2000

[25] Klopman G., Stive M.J.F., Extreme waves and wave loading in shallow water. Proceedings E&P forum workshop: Wave and current kinematics and loading. Paris 25-26 October 1989

[26] Battjes J.A., Stive M.J.F., Calibration and verification of a dissipation model for random breaking waves, Journal of Geophysical Research 90 (C5), pp. 9159-9167 (1985)

[27] Battjes J.A., Janssen J.P.F.M., Energy loss and set-up due to breaking of random waves. Proceedings 16th International Conference on Coastal Engineering, Hamburg, pp. 569-587 (1978)

[28] Klopman G., Extreme wave heights in shallow water, Report H2486, WL|Delft Hydraulics (1996)

[29] Battjes J.A., Groenendijk H.W., Wave height distributions on shallow foreshores. Coastal engineering 40 (2000) 161-182

APPENDIX 1. DATA ANALYSIS METHODS

A1.1. Using Matlab

The data from the tests performed by CHC is available in binary format on CD-ROM's. This data is first converted into ASCII format using a conversion program provided by CHC. The data is then imported into Matlab as a matrix where the columns represent the different probes and the rows represent the surface elevation at different points in time.

A1.2. Time series analysis

The basic purpose of time series analysis is to define the variability of a data series in terms of dominant periodic functions.

A1.2.1. High frequency noise

In the test results there is a clear high frequency distortion of the data that is of no interest to the research. This high frequency noise has been removed from the data.

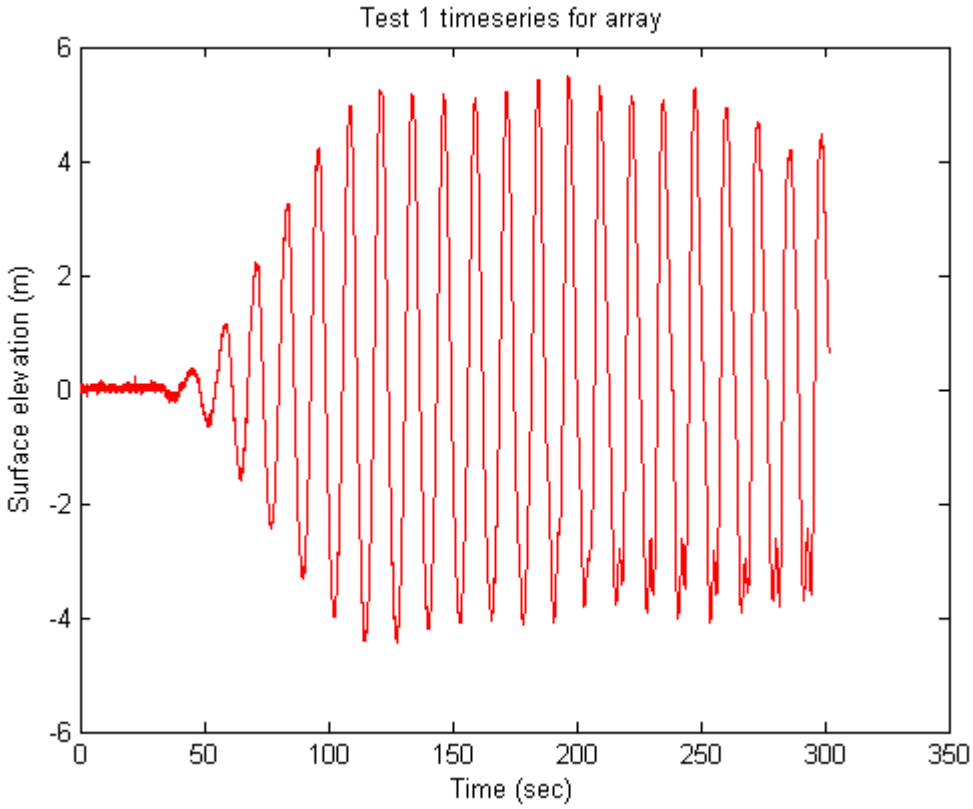

Figure 86: Untreated time series

There are two main methods to remove these high frequency oscillations; digital filters and removal of the high frequencies of a Fast Fourier Transformed (FFT-ed) time series followed by an Inverse FFT (IFFT).

A1.2.1.1. Digital filters

A digital filter filters out specific frequencies from the data. In our case we need to develop a low-pass filter, which lets the low frequencies pass but filters out the high frequency noise. The text in this paragraph is established after studying Data Analysis Methods in Physical Oceanography by Emery and Thomson [1]. A good low-pass filter should have five essential qualities:

1. A Sharp cut-off that effectively removes high frequency components
2. A comparatively flat pass-band that leaves the low frequencies unchanged
3. A clean transient response, which means that rapid changes in the signal do not result in so-called ringing within the filtered record
4. Zero phase-shift
5. Acceptable computation time

The definition of a digital filter is an algebraic process by which a sequential input $\{x_n\}$ is systematically converted into a sequential output $\{y_n\}$. In the case of a linear filter, the time domain transformation is accomplished through convolution or so-called blending of the input with the weighting function of the filter.

- A recursive filter calculates the output from the input and past values of the output using a feedback loop, which is the second sum in equation{20}

$$y_n = \sum_{k=-M}^{M} h_k x_{n-k} + \sum_{j=-L}^{L} g_j y_{n-j}, n = 0,.1,..., N-1 \quad \{20\}$$

in which M and L are integers and h_k and g_i are non-zero weighting functions.

- The equation for a non-recursive filter is similar to equation {20} with g_j=0, that is without the feedback loop.
- A physically unrealisable filter uses data from the past, k ranges from –M to zero, and the future, k from zero to M. This is widely used in the filtering of pre-recorded data for which all digital values are available beforehand, which is the case here.
- Physically realisable filters have a range of k from zero to M.

For a non-recursive (no feedback loop) linear filter the output $\{y_n\}$ is obtained through the convolution:

$$y_n = \sum_{k=-M}^{M} h_k x_{n-k} = \sum_{k=-M}^{M} h_{n-k} x_k, n = 0,1,..., N-1 \quad \{21\}$$

in which h_k are the time invariant weights. For a symmetric filter of this kind h_k=h_{-k} and the time domain convolution becomes:

$$y_n = \sum_{k=0}^{M} h_k \left(x_{n-k} + x_{n+k}\right), n = 0,1,..., N-1 \quad \{22\}$$

1. The set of weights in equation {22}, $\{h_k\}$ is called the Impulse Response Function

The Fourier Transform of $y(t_n)$ in equation {21} is:

$$Y(\omega) = \sum_{n=-M}^{M} y_n e^{-i\omega_n \Delta t} = \sum_{k=-M}^{M} h_k e^{-i\omega_k \Delta t} \sum_{n=-M}^{M} x_{n-k} e^{-i\omega_{(n-k)} \Delta t} = H(\omega) X(\omega) \quad \{23\}$$

This yields that convolution in the time-domain corresponds to multiplication in the frequency domain.

2. The function $H(\omega) = Y(\omega)/X(\omega)$ from equation {23} is the so-called Frequency Response Function:

$$H(\omega) = \sum_{k=-M}^{M} h_k e^{-i\omega_k \Delta t}, \omega \equiv \omega_n = 2\pi n/N\Delta t, n = 0,1,...,N/2 \quad \{24\}$$

For a symmetric filter,

$$H(\omega) = h_0 + 2\sum_{k=1}^{M} h_k \cos(\omega k \Delta t) \quad \{25\}$$

Once H(ω) is specified, $\{h_k\}$ can be found through IFFT:

$$h_k = \sum_{n=-N/2}^{N/2} H(\omega) e^{i\omega_n k \Delta t} \quad \{26\}$$

In general H(ω) is a complex function that can be written in the form:

$$H(\omega) = |H(\omega)| e^{i\phi(\omega)} \quad \{27\}$$

Where $|H(\omega)|$ is the **gain** of the filter and $\phi(\omega)$ is the **phase lag**. The power of the transfer function is given by

$$P(\omega) = H(\omega)H(-\omega) = H(\omega)H^*(\omega) = |H(\omega)|^2 \quad \{28\}$$

An ideal filter has a gain of 1 for all frequencies in the pass band, and 0 for all frequencies in the stop band. In addition a phase lag of 0 for all ω ensures there is no alteration in the phase of the frequency components.

3. Achieving $\phi(\omega)$=0: For recursive filters this is done by first passing the input forward, then, after inversion of the weights, backward through the same set of weights. For non-recursive filters using symmetric filters this results in zero phase-lag.

For an ideal low-pass filter $|H(\omega)| = 1$ for $|\omega| \le \omega_c$ and 0 for $\omega_c \le \omega$, with $\omega_c = 2\pi f_c$ is the cut-off frequency, the transition from the pass- to the stop band. For an ideal filter this transition is step like, in practice the transition has a finite width and ω_c is defined as the frequency at which the mean filter amplitude in the pass band is decreased by a factor $\sqrt{2}$.

4. The cut-off frequency ω_c is the frequency at which the power of the filter is down by a factor 2, or by 3 decibels.

The transition from pass- to stop band results in so-called overshoot ripples, which distort the filtered signal.

The succession of these overshoot ripples, or 'ringing' is often referred to as the Gibbs' phenomenon. A technique called windowing is applied to attenuate the overshoot ripples by truncation in the time domain. This technique will be explained further on in this appendix, for now we suffice in mentioning that it is required to obtain an accurate digital filter.

There are many possible digital filters, of all of these, Butterworth filters of the form $|H(\omega)|^2 = \frac{1}{1+(\omega/\omega_c)^{2q}}$ have a number of desirable features:

5. It's monotonically flat within the pass- and stop band; no overshoot ripples.
6. It has a high tangency at both the origin, ω=0 and at the Nyquist frequency ω_c.
7. The attenuation rate can be increased by increasing the filter order q, too steep a transition will lead to ringing however.
8. Due to its squared response, the Butterworth filter produces zero phase-shift and its amplitude is attenuated by a factor of 2 at the cut-off frequency for all q.
9. In contrast to non-recursive filters there is no loss of output data at the ends of the records; N input values lead to N output values. Ringing distorts the data at the end of the filtered output however, this results in the need to ignore the output near the end analogous to non-recursive filters.

In the present study, the digital filter studied is a Butterworth filter, which can be classified as a physically realisable recursive infinite impulse response filter. The approach of designing a Butterworth filter is as follows:

1. Specify the sampling frequency $\omega_s = 2\pi f_s = 2\pi/\Delta t$

The frequency range is then defined by $0 < \frac{\omega}{\omega_s} < 0.5$ where the upper limit is $\frac{\omega_N}{\omega_s}$.

2. Specify the desired cut-off frequency at half power point of the filter
3. Specify the filter order q. This can be either done on basis of experience, q is often between 8 and 10, or q can be calculated based on the required attenuation at a given frequency.

In Matlab the designed filter has a cut-off frequency of 1Hz and the filter is shown to filter out the high frequency noise with zero phase-shift and without changing the rest of the signal significantly in Figure 87.

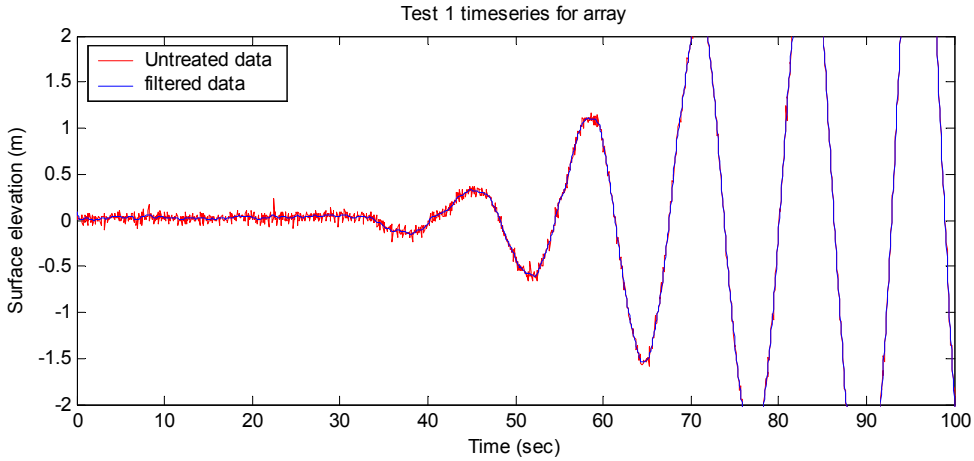

Figure 87: Digitally filtered time series

A1.2.1.2. Removal of high frequencies using the Fourier Transform

The removal of the high frequency noise using the Fourier Transform is much simpler and much more straightforward then the digital filters discussed in A1.2.1.1. The procedure is to first FFT the data, then set all frequency components higher than the cut-off frequency to zero. Scaling the first component of the FFT by dividing it by the number of points in the FFT gives the mean value of the signal or the so-called set-up. After setting this first component and all frequencies higher than 1Hz to zero the IFFT is taken, which results in the time series without the high frequency noise.

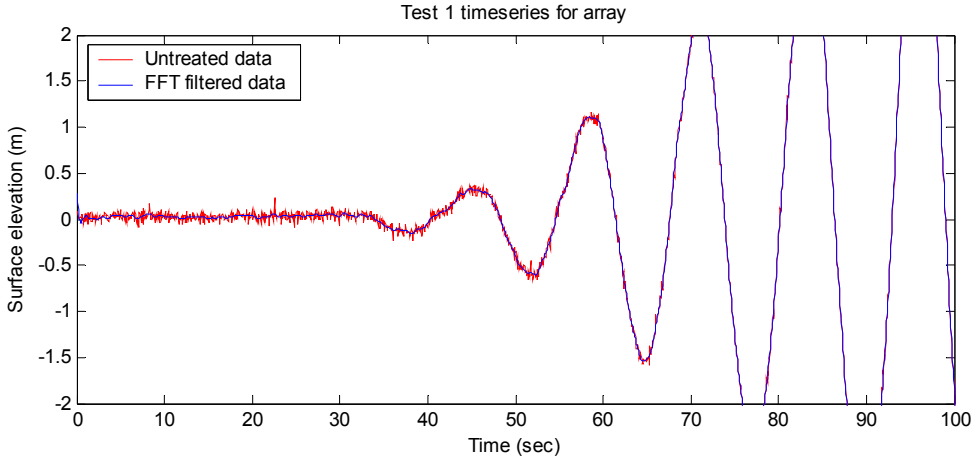

Figure 88: FFT filtered time series

As is clear from Figure 88, the FFT filtered time series represents the original signal very accurately with the high frequency noise removed. At the very start of the time series the FFT filtered series goes up, this is due to the fact that the original time series also starts with an above zero surface elevation. It is concluded that FFT high frequency filtering is a good method for the applications within this research project. Figure 89 shows the filtered time series represents the original signal accurately for the entire duration of the signal.

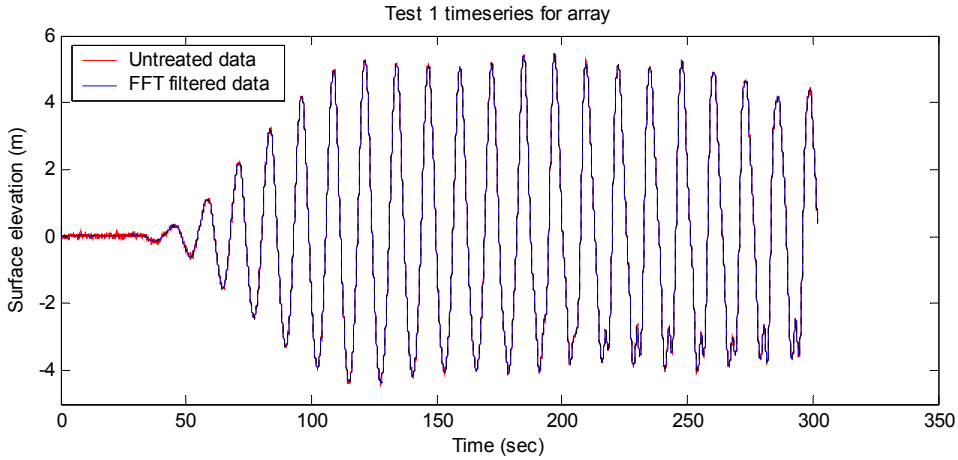

Figure 89: The complete FFT filtered time series

A1.2.2. Fourier analysis

Fourier analysis is one of the most commonly used techniques to identify the periodic components in near-stationary time series. It can in theory be applied to both regular and irregular sea-states, for the irregular waves one is however more interested in the spectrum of the time series and not so much in the individual waves. For regular waves this obviously is not the case and Fourier analysis gives valuable information on both the amplitude and phase-lag of the Fourier components. This section therefore addresses regular waves only. As is shown in Figure 86, the time series of the regular wave is not periodic throughout the series, it is stated by CHC that the first five cycles after t=120 seconds are the best representation of periodic waves; these need to be taken from the time series.

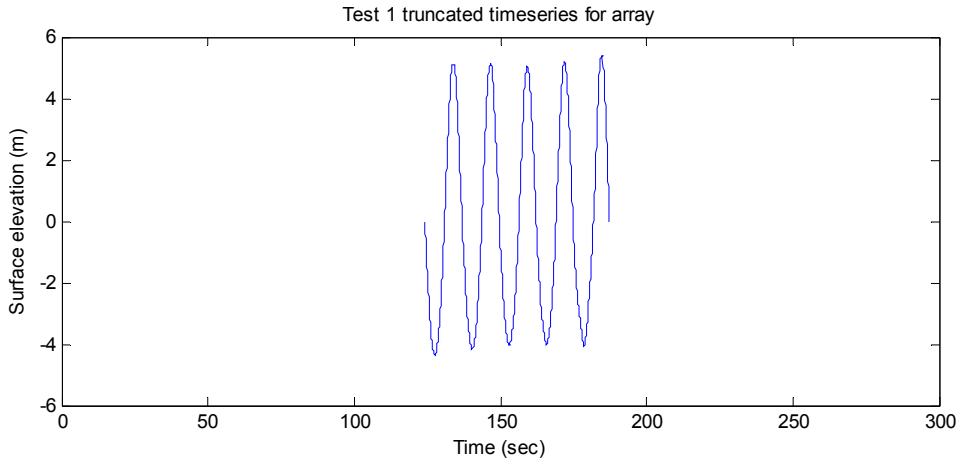

Figure 90: Truncated filtered time series

This series has a time range of approximately 63 seconds, consisting of 943 data points. The time series needs to be transformed to the frequency domain to assess distribution of energy over the frequencies. If a Fast Fourier Transform (FFT) is performed on the isolated five cycles the following variance density spectrum can be obtained:

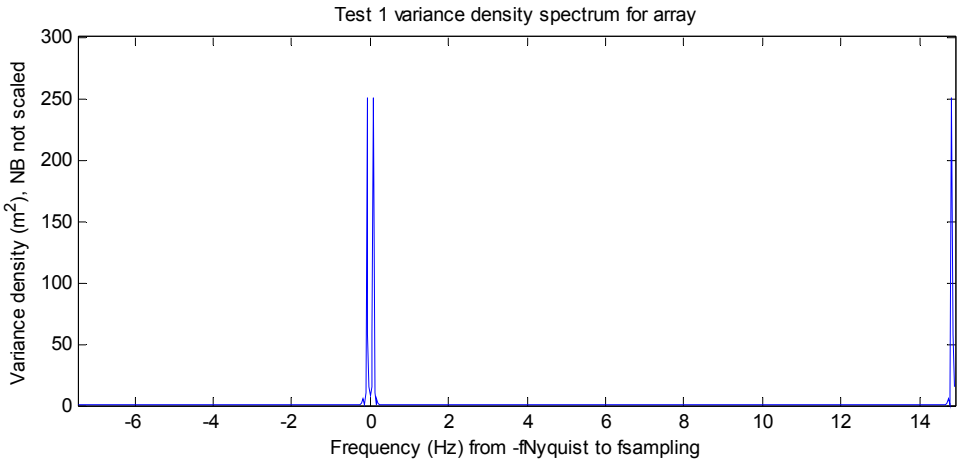

Figure 91: Frequency domain analysis

The negative frequencies have no physical meaning and are purely mathematical. The spectrum is mirrored at, or symmetrical around, the Nyquist frequency, which is half the sampling frequency. $f_N = \frac{1}{2\Delta t} \approx 7.5\text{Hz}$. Here Δt is the sampling interval. This implies that

all the energy that is physically present in frequencies higher than the Nyquist frequency is added to the spectrum on the left side of the Nyquist frequency and that the entire spectrum from f=0 to the Nyquist frequency is mirrored around the Nyquist frequency. The energy in the spectrum is negligible for frequencies higher than 1Hz; therefore there is no significant distortion of the data caused by this mirroring process. The part of the spectrum at frequencies that are higher than the Nyquist frequency has no physical meaning; the shown variance above the Nyquist frequency is also a purely mathematical feature. The duration T of the time series determines the step size $\Delta f=1/T$ in the Fourier Transform. Figure 92 shows the distribution over the frequencies for a duration of 512 points (the next power of 2 is 1024, which is larger than 943) or 34.35 seconds, yielding a step size Δf of 0.0291Hz. Due to the fact that we are looking at regular waves, it is clear that the distribution over the frequencies is not represented correctly for this step size.

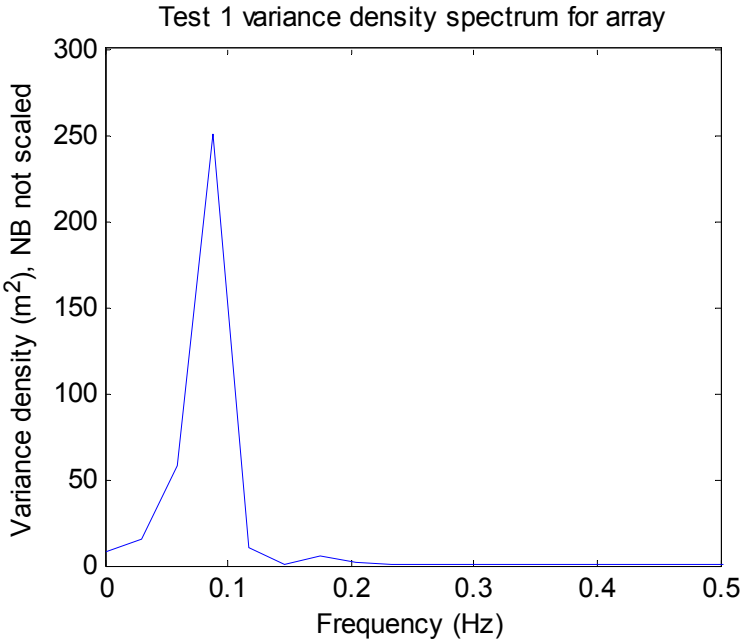

Figure 92: Spectral resolution

In order to have a sufficient small step size, which determines the so-called resolution of the transform, the length of the time series with the five regular wave cycles needs to be expanded. This can be done by adding zeros to the time series and later scaling the output back to the length with the actual signal. Another way is to copy the five cycles a number of times and truncate it at a power of 2.

A1.2.2.1. Zero padding

The number of points in the record is expanded to 2^{13} or 8192; this means the record is padded with zeros to a total length of almost 550 seconds.

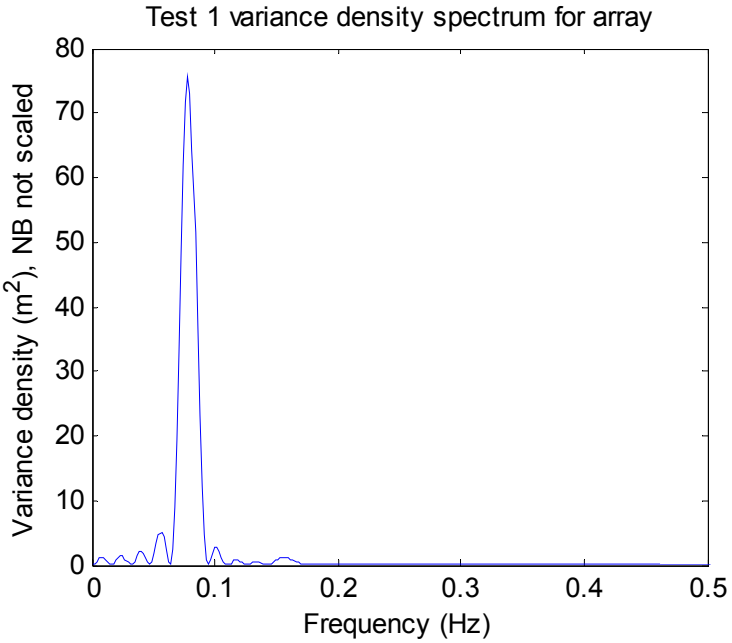

Figure 93: Ringing caused by zero padding

The reduced variance is caused by the long section of zero's and should be rescaled to resemble the variance in the actual record and not the variance in the zero padded record. The scaling factor is 8192/951, this equals the total #points in the zero padded record/#points in the initial wave record. The resulting spectrum is much higher and much narrower than the spectrum obtained by performing a 512-point FFT. A negative consequence of the increased number of points in the FFT is the creation of the so-called side-lobes that appear on both sides of the main peak. These lobes have no physical meaning but are caused by so-called spectral leakage at the end of the time series, a mathematical problem in discrete Fourier Transforms. This means that some of the variance (or energy) of certain frequencies leaks from one frequency to another, distorting the actual variance density spectrum. So increasing the number of points in the FFT by adding zero's at the end of the time series increases the resolution, but doing so it introduces the negative process of spectral leakage. Therefore there is an optimum in the amount of numbers used in an FFT. For irregular wave time series a method called windowing is used where the time series is divided in segments of a certain amount of numbers. The amount of numbers per segment is set to result in a high resolution and low leakage or distortion. In regular waves this technique is not necessary, it is enough to just simply copy the time series a number of times so that it results in longer time series with an appropriate number of points. This is allowed since the waves are assumed to be regular.

A1.2.2.2. Copying the time series

The five cycles shown in Figure 90 are copied to make a time series of 8192 points. A 8192-point FFT of this time series gives the spectrum as in Figure 94

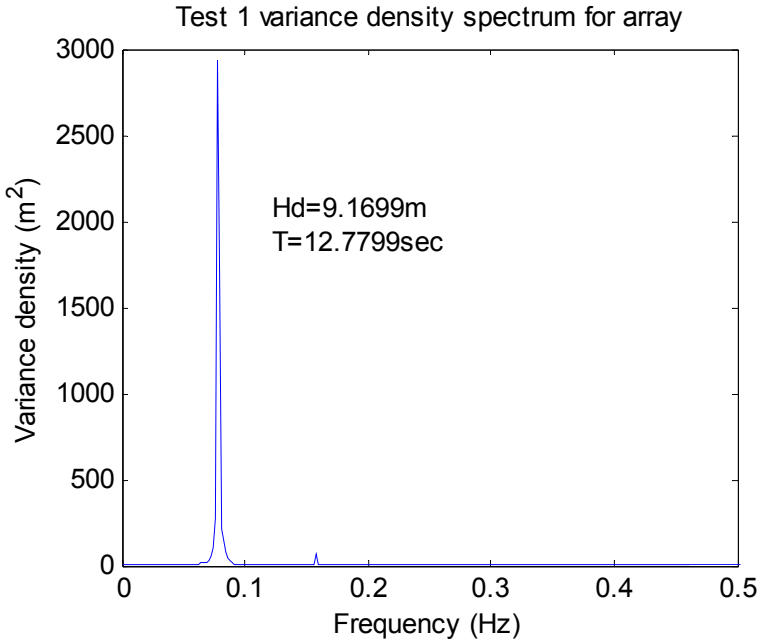

Figure 94: 2^{13}-point spectrum of copied cycles

The target parameters for this wave test are a wave height of 10 meters and a period of 12.7 seconds. Since the deviation of these target parameter is quite large, the method applied is tested on a perfect sine wave with an amplitude of 5 meters over 8192 points. The resulting spectrum is shown in Figure 95.

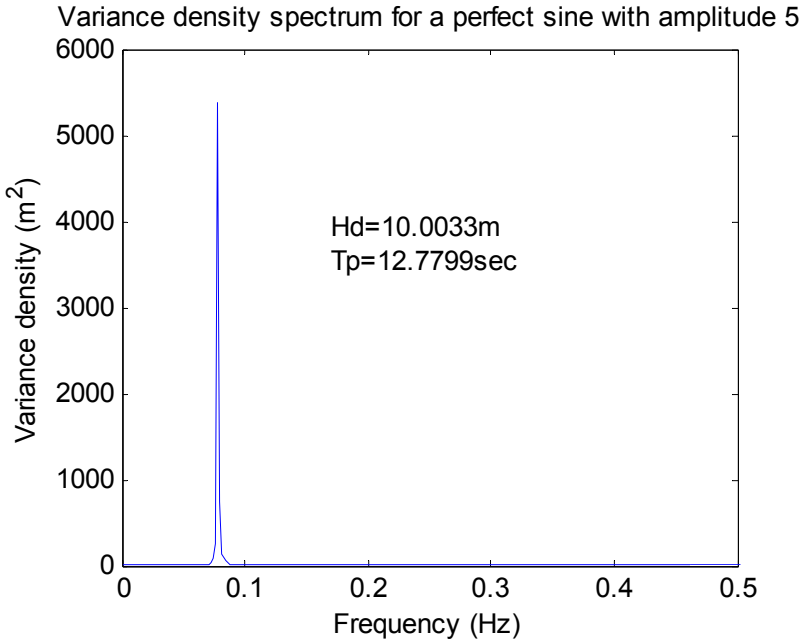

Figure 95: 2^{13}-point spectrum for perfect sine

The small error in the wave height is caused by round off errors in Matlab, the error is 0.03%, which is well within acceptable limits. Apparently the method applied works fine, it's the actual wave test that does not match the target parameters exactly.

A1.2.2.3. Harmonic components

An FFT of the time series is taken to produce a frequency domain analysis, it shows at which frequency the energy is concentrated. The first component of the FFT represents the set-up or set-down caused by the signal, which can also be calculated as the mean of the time series of the signal. Spectral peaks at the incident frequency and integer multiples of the incident frequency are the so-called harmonics. These spectral peaks are separated from the rest of the signal by removing all spectral components other than those at or near the spectral peak with a bandwidth of 0.25 times the incident frequency above and below the spectral peak. Components at these frequencies are the first, second, third etcetera harmonics respectively. An IFFT of the changed spectrum results in time series of the separate components showing there amplitude and phase-lag. It can be explored how many harmonic components are required to represent the original signal with sufficient accuracy.

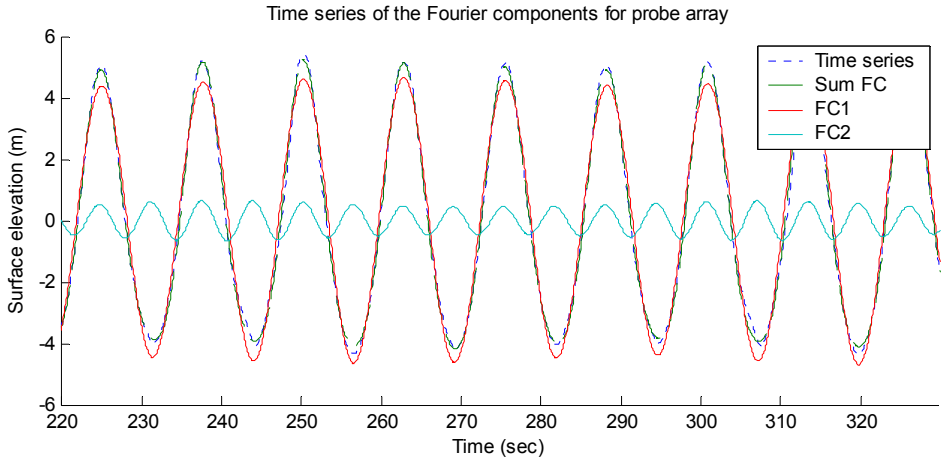

Figure 96: Time series separated in its Fourier components

For the undisturbed regular wave test with parameters H_d=10m and T_p=12.7seconds, Figure 96 shows that only two components are required to give a very accurate representation of the original time series. The figure shows an arbitrary section of the approximately 550-second time series of the copied 5 cycle section. Figure 98 shows the location of the probes during the model tests on the LUN-A structure, here we will only show the variance density spectrum and the Fourier component time series for the centre probe, R11.

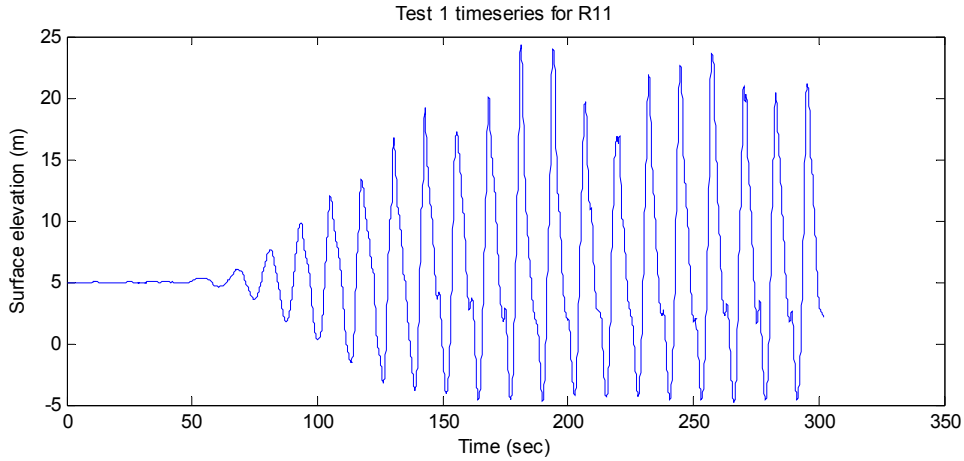

Figure 97: Regular wave time series at probe R11

As is clear from Figure 97, not all probes are calibrated to have the still water level at 0m. This is accounted for when further analysing the results.

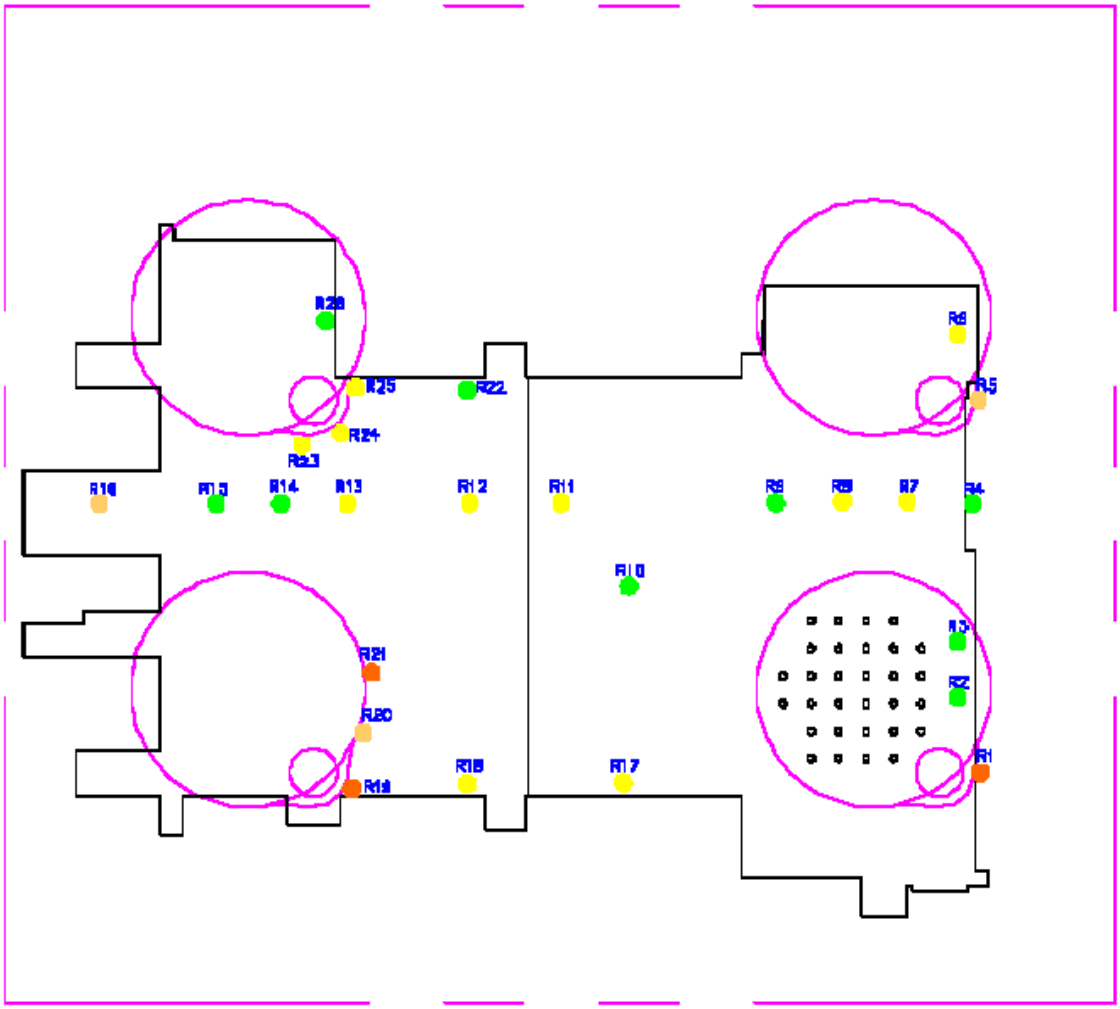

Figure 98: Probe locations for the LUN-A model tests

The variance density spectrum is calculated in the same way as for Figure 94. That is the same five "periodic" cycles are isolated from the series and copied to make a 8192-point time series. From this series the variance density spectrum is calculated as shown inFigure 99

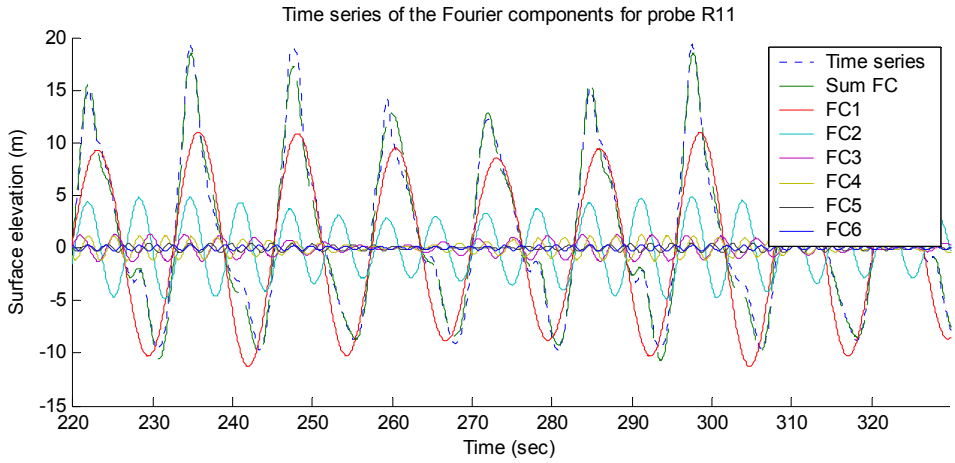

Figure 99: Fourier components R11

Figure 100 shows the variance density spectra for a 8192-point FFT with both a linear and a log variance scale. The log-scale shows a very grassy spectrum. This problem can be solved using a technique called windowing, which will be discussed later in A1.2.3. In this section it is explored how well the original time series is represented by the sum of a number of harmonic components. When applying the windowing technique, the phase information is lost and therefore this comparison can not be made. Figure 100 also shows that the main variance is located at the first and second harmonics. Therefore the sum of only the first two Fourier components is compared to the actual signal in Figure 101.

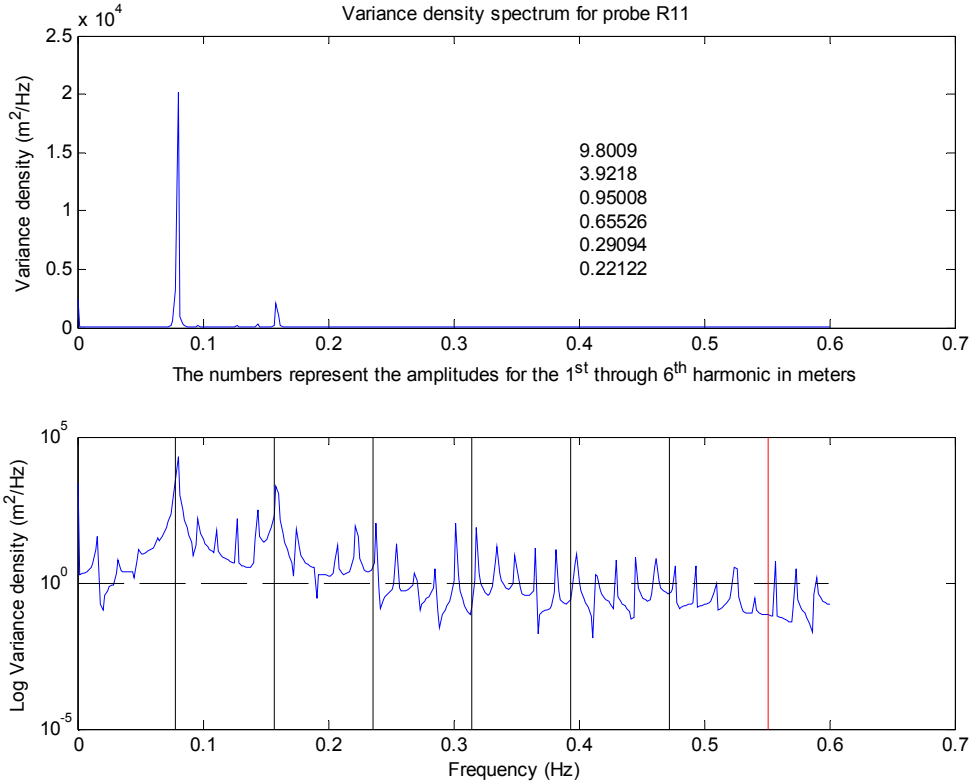

Figure 100: Variance density spectra R11

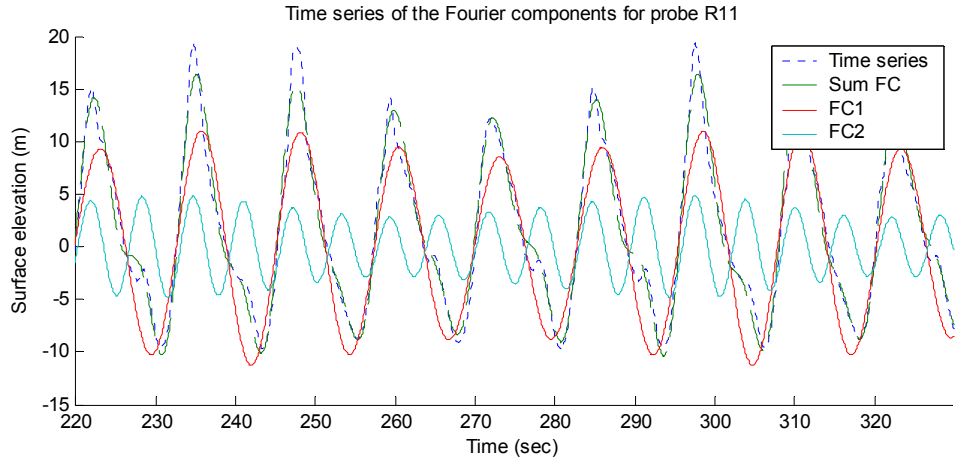

Figure 101: Replicated signal using only the first two harmonics

For the lowest three waves the signal is well represented using only the first two harmonics, for the peak values the higher order components are needed to give a good representation of the original signal.

A1.2.3. Spectral analysis

The window applied is the Hanning window.

As mentioned in A1.2.2.3, spectral analysis is applied mainly to irregular waves since the phase information is of less interest than when looking at a limited number of cycles of regular waves. The variance density spectra for all the tests at every probe location can be calculated and graphed. In this section only a number of probes will be analysed.

Test 3 is the 100-year Multi directional sea-state without any currents with the waves approaching the structure head-on. The target parameters for this sea-state are a peak period T_p of 14.3sec and a significant wave height H_{m0} of 9.9m. Figure 102 is the 3-hour filtered time series that will be used as input for the spectral analysis.

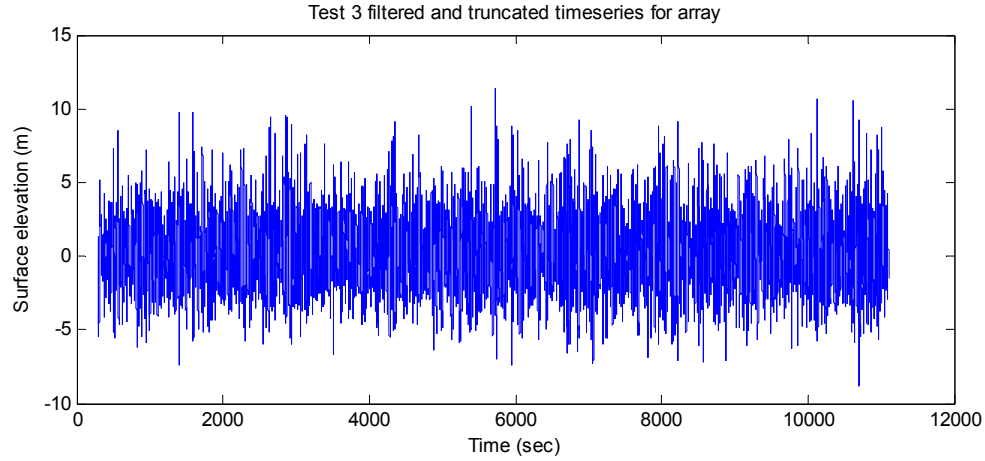

Figure 102: Time series for the undisturbed wave

When the spectrum is calculated using only the FFT and without any windowing applied, the resulting spectrum becomes very grassy as is clear from Figure 103.

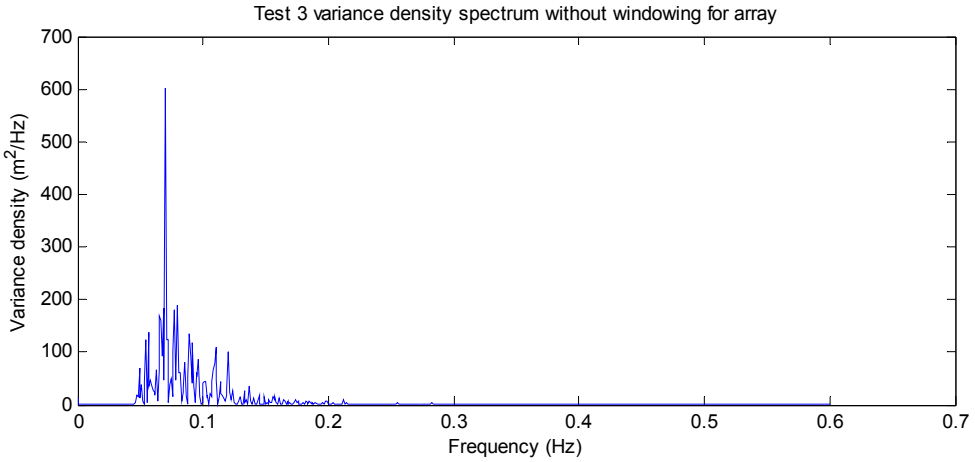

Figure 103: Grassy spectrum

When applying the windowing technique, the spectrum is much smoother. The smoothness depends on the number of windows. The spectral resolution depends on m, the amount of points in each window. Spectral density plots for various numbers of

windows with various numbers of points per window are shown in Figure 104, Figure 105, and Figure 106.

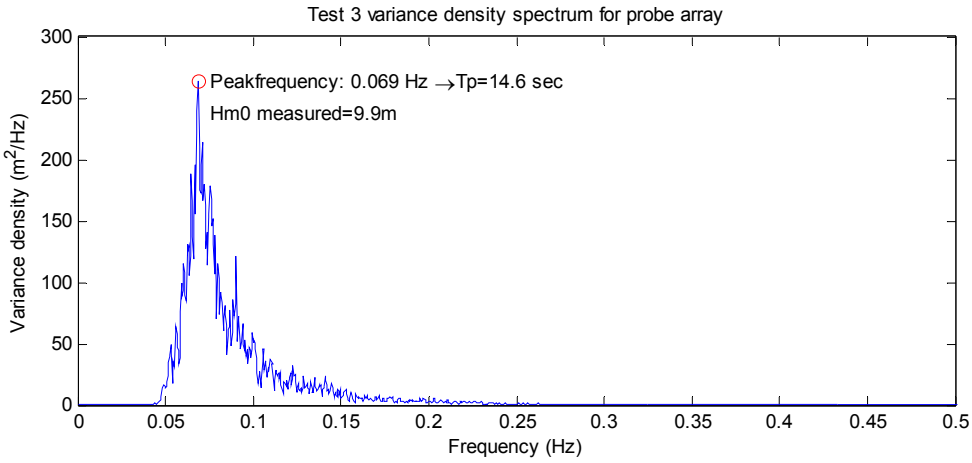

Figure 104: Spectrum for 2^{15} points per window

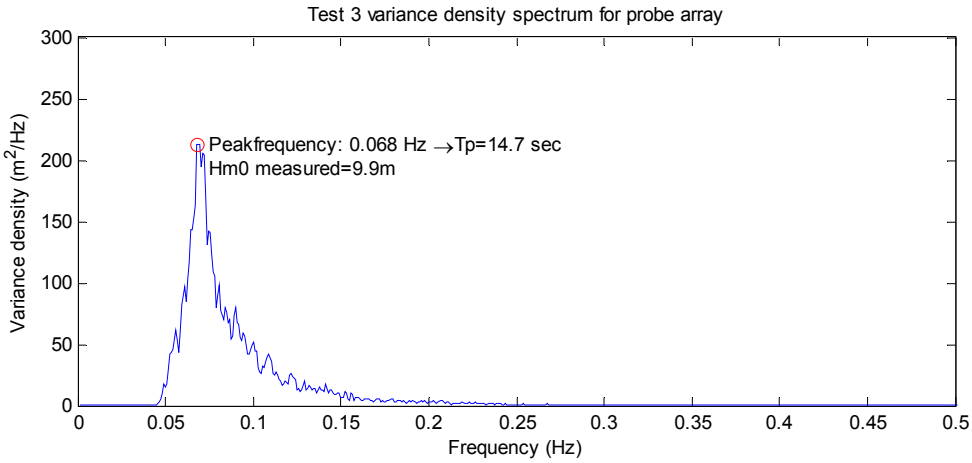

Figure 105: Spectrum for 2^{14} points per window

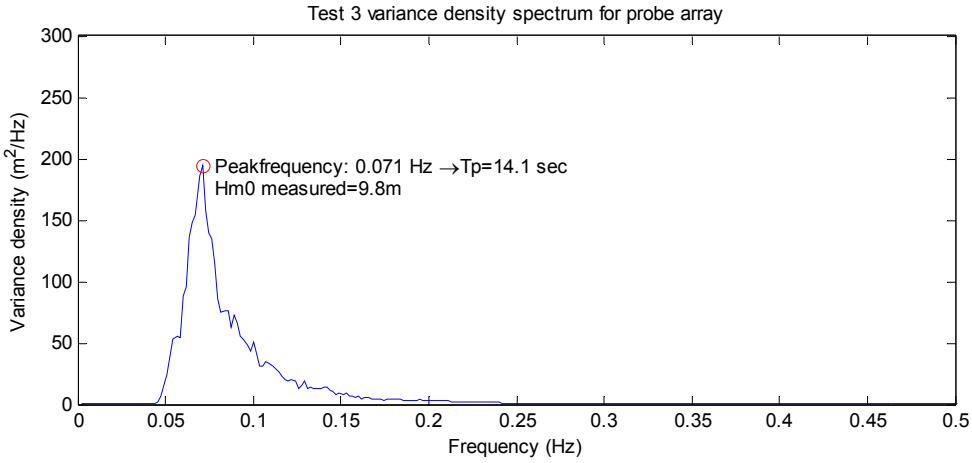

Figure 106: Spectrum for 2^{13} points per window

These figures clearly demonstrate that for a time series with a constant number of data points, increasing the number of windows (reducing the number of points per window) leads to a smoother spectrum at the cost of spectral resolution.